



HAL
open science

Electronic properties of quasicrystals

Nicolas Macé

► **To cite this version:**

Nicolas Macé. Electronic properties of quasicrystals. Disordered Systems and Neural Networks [cond-mat.dis-nn]. Université Paris-Saclay, 2017. English. NNT : 2017SACLS313 . tel-01681120v1

HAL Id: tel-01681120

<https://theses.hal.science/tel-01681120v1>

Submitted on 11 Jan 2018 (v1), last revised 15 Jan 2018 (v2)

HAL is a multi-disciplinary open access archive for the deposit and dissemination of scientific research documents, whether they are published or not. The documents may come from teaching and research institutions in France or abroad, or from public or private research centers.

L'archive ouverte pluridisciplinaire **HAL**, est destinée au dépôt et à la diffusion de documents scientifiques de niveau recherche, publiés ou non, émanant des établissements d'enseignement et de recherche français ou étrangers, des laboratoires publics ou privés.

NNT : 2017SACLS313

THÈSE DE DOCTORAT
DE L'UNIVERSITÉ PARIS-SACLAY
PRÉPARÉE UNIVERSITÉ PARIS-SUD

École doctorale n°564
Physique en Île-de-France
Spécialité de doctorat : Physique

par

M. NICOLAS MACÉ

Propriétés électroniques des quasicristaux

Thèse présentée et soutenue à Orsay, le 28 septembre 2017.

Composition du jury :

M.	CLÉMENT SIRE	Directeur de recherche Université Paul Sabatier	(Président du jury)
M.	ERIC AKKERMANS	Professeur Technion	(Rapporteur)
M.	UWE GRIMM	Professeur The Open University	(Rapporteur)
M.	JEAN-MARC LUCK	Directeur de recherche CEA Saclay	(Examinateur)
Mme.	ANURADHA JAGANNATHAN	Professeur Université Paris-Saclay	(Directrice de thèse)
M.	PAVEL KALUGIN	Maître de conférences Université Paris-Saclay	(Membre invité)
M.	FRÉDÉRIC PIÉCHON	Chargé de recherche Université Paris-Saclay	(Membre invité)

Titre : Propriétés électroniques des quasicristaux

Mots clefs : pavages, quasicristaux, propriétés électroniques, analyse multifractale

Résumé : Nous considérons le problème d'un électron sur des pavages quasipériodiques en une et deux dimensions. Nous introduisons tout d'abord les pavages quasipériodiques d'un point de vue géométrique, et défendons en particulier l'idée que ces pavages sont les pavages apériodiques les plus proches de la périodicité.

Nous concentrons plus particulièrement sur l'un de pavages quasipériodiques les plus simples, la chaîne de Fibonacci, nous montrons à l'aide d'un groupe de renormalisation que la multifractalité des états électroniques découle directement de l'invariance d'échelle de la chaîne.

Élargissant ensuite notre champ d'étude à un ensemble de chaînes quasipériodiques, nous nous intéressons au théorème de label des gaps, qui décrit comment la géométrie d'une chaîne donnée contraint les valeurs que peut prendre la densité d'états intégrée dans les gaps du spectre électro-

nique. Plus précisément, nous nous intéressons à la façon dont l'énoncé de ce théorème est modifié lorsque l'on considère une séquence d'approximants périodiques approchant une chaîne quasipériodique.

Enfin, nous montrons comment des champs de hauteurs géométriques peuvent être utilisés pour construire des états électroniques exacts sur des pavages en une et deux dimensions. Ces états sont robustes aux perturbations du hamiltonien, sous réserve que ces dernières respectent les symétries du pavage sous-jacent. Nous relierons les dimensions fractales de ces états à la distribution de probabilités des hauteurs, que nous calculons de façon exacte. Dans le cas des chaînes quasipériodiques, nous montrons que la conductivité suit une loi d'échelle de la taille de l'échantillon, dont l'exposant est relié à cette même distribution de probabilités.

Title : Electronic properties of quasicrystals

Keywords : tilings, quasicrystals, electronic properties, multifractal analysis

Abstract : We consider the problem of a single electron on one and two-dimensional quasiperiodic tilings. We first introduce quasiperiodic tilings from a geometrical point of view, and point out that among aperiodic tilings, they are the closest to being periodic.

Focusing on one of the simplest one-dimensional quasiperiodic tilings, the Fibonacci chain, we show, with the help of a renormalization group analysis, that the multifractality of the electronic states is a direct consequence of the scale invariance of the chain.

Considering now a broader class of quasiperiodic chains, we study the gap labeling theorem, which relates the geometry of a given chain to the set of values the integrated density of states can take in

the gaps of the electronic spectrum. More precisely, we study how this theorem is modified when considering a sequence of approximant chains approaching a quasiperiodic one.

Finally, we show how geometrical height fields can be used to construct exact eigenstates on one and two-dimensional quasiperiodic tilings. These states are robust to perturbations of the Hamiltonian, provided that they respect the symmetries of the underlying tiling. These states are critical, and we relate their fractal dimensions to the probability distribution of the height field, which we compute exactly. In the case of quasiperiodic chains, we show that the conductivity follows a scaling law, with an exponent given by the same probability distribution.

Résumé

Les quasicristaux sont des solides aperiodiques présentant un ordre à longue distance, qui se manifeste par une figure de diffraction purement constituée de pics de Bragg. Dans de tels matériaux, ordonnés mais non périodiques, quelle est la structure du spectre et des fonctions d'onde des électrons de conduction ? C'est l'objet de cette thèse de proposer des réponses à cette question générale.

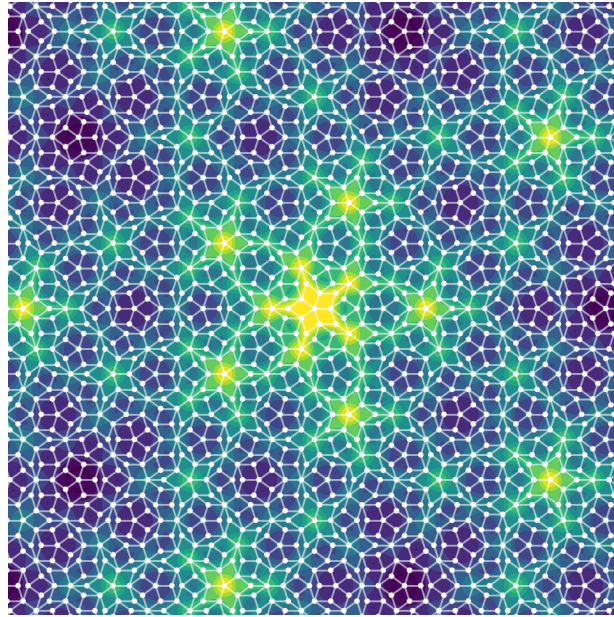


Figure 1. – Un état propre fractal d'un modèle de la forme (1). Le pavage quasipériodique sous-jacent est le pavage de Penrose. Il représenté par le graphe blanc: chaque sommet correspond à un site m dans l'équation (1), et chaque arrête correspond à un lien $t_{m,n}$ entre deux sites. La couleur code la probabilité de présence de l'électron (la couleur a été "élargie" au voisinage de chaque site pour plus de visibilité).

Dans cette thèse, les quasicristaux sont modélisé par des pavages quasipériodiques uni ou bidimensionnels. Sur ces pavages, nous étudions les propriétés d'un unique électron de conduction. Le hamiltonien de l'électron, de type liaisons fortes, est donné par

$$\hat{H} = - \sum_{\langle m,n \rangle} t_{m,n} |m\rangle \langle n| + \text{H.c} + \sum_m V_m |m\rangle \langle m|, \quad (1)$$

où les entiers m et n indexent les atomes, et où $|m\rangle$ est la fonction d'onde localisée sur l'atome numéro m . $t_{m,n}$ est l'amplitude de saut de l'atome m à l'atome n , et V_m est un potentiel sur site. Les $t_{m,n}$ et V_m sont choisis de façon à respecter la symétrie du pavage quasipériodique sous-jacent. De tels modèles ont des *propriétés critiques*: leur spectre possède une composante singulière, et leurs états propres sont génériquement multifractals. La figure (1) montre un exemple d'un tel état propre, pour un modèle de type (1) introduit par [Sutherland \[1986\]](#). Sur l'échantillon choisi ici, la distribution des amplitudes adopte une structure en forme d'étoile à cinq branches, qui

est elle-même constituée de structures similaires, à une plus courte échelle. Cette “invariance d’échelle” de la distribution locale des amplitudes est le reflet de la nature multifractale de l’état électronique.

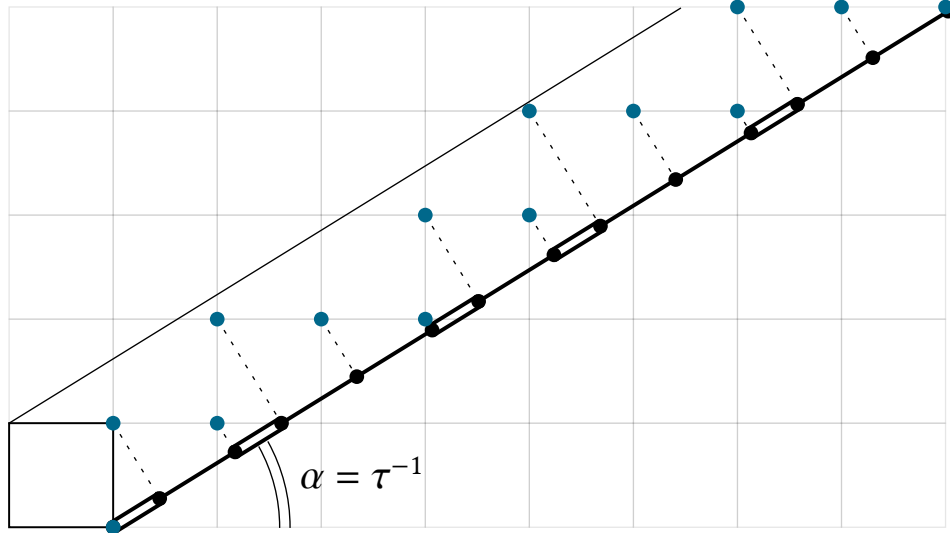


Figure 2. – Illustration de la méthode de coupe et projection, utilisée ici pour construire la chaîne de Fibonacci $\tau = (1 + \sqrt{5})/2$ est le nombre d’or.

Dans une première partie, nous introduisons les pavages quasipériodiques d’un point de vue géométrique, et présentons deux méthodes de construction : la méthode de coupe et projection, et les règles de substitution. Attardons-nous un instant pour décrire la méthode de coupe et projection. Grossièrement, elle consiste en la projection d’une “tranche” de points d’un réseau de dimension D sur un sous-espace de dimensions $d < D$. Cette opération permet de construire un pavage périodique ou quasipériodique. La figure (1.6) illustre cette construction dans le cas où on part d’un réseau carré ($D = 2$). La “tranche” est ici obtenue en translatant le carré unité (en bas à gauche de la figure) le long de la droite de pente τ^{-1} , où τ est nombre d’or. Les points de la “tranche” sont en bleu sur la figure. Ils sont projetés sur cette même droite, formant une chaîne de points. La distance entre deux points sur cette chaîne peut être “petite” (indiquée par un double lien sur la figure), ou “grande” (simple lien) de leurs plus proches voisins. Cette chaîne quasipériodique est appelé chaîne de Fibonacci.

Nous considérerons en fait dans cette thèse qu’un pavage est quasipériodique si et seulement si il n’est pas périodique, et peut être construit par la méthode de coupe et projection décrite ci-dessus. Nous présentons dans le même temps quelques propriétés des pavages quasipériodiques : la répétitivité, l’ordre à longue distance et l’invariance d’échelle. Dans le cas unidimensionnel, nous introduisons la notion de complexité qui nous sert à appuyer l’idée que les pavages quasipériodiques sont les pavages apériodiques les plus proches de la périodicité.

Dans une deuxième partie, nous nous concentrons plus particulièrement sur l’un de pavages quasipériodiques les plus simples, la chaîne de Fibonacci (figure (3)). Sur cette chaîne, les modèles de type (1) possèdent un spectre purement singulier (la densité d’état intégrée est un escalier de Cantor), et des états propres critiques (c’est-à-dire ni localisés ni étendus, mais multifractals). À l’aide d’un groupe de renormalisation, on peut exploiter la construction par substitution de la chaîne de Fibonacci (non explicitée dans ce résumé), pour montrer le caractère singulier du spectre. Concrètement, le groupe de renormalisation permet de montrer que $\hat{H}(L)$, le hamiltonien

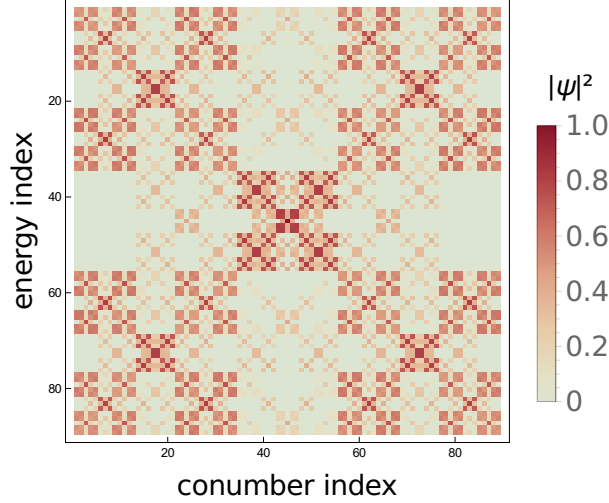


Figure 3. – Densité d’état électronique, en fonction de la “co-numérotation” (conumber en anglais) et de l’énergie. Une structure fractale est clairement visible

du système sur un chaîne de taille L , s’écrit

$$\hat{H}(L) \simeq \left(z\hat{H}(L/\tau^2) - t_B \right) \oplus \left(\bar{z}\hat{H}(L/\tau^3) \right) \oplus \left(z\hat{H}(L/\tau^2) + t_B \right), \quad (2)$$

où t_B , z et \bar{z} sont des paramètres physiques. On voit ainsi que le hamiltonien à l’échelle L peut être décrit comme une somme de hamiltoniens à de plus courtes échelles L/τ^2 , L/τ^3 . Comme ces hamiltoniens sont similaires au hamiltonien d’origine, cette équation révèle une propriété d’invariance d’échelle du hamiltonien. De cela découle le caractère singulier du spectre.

En utilisant ce même groupe de renormalisation, nous dérivons une relation de récurrence perturbative pour les états électroniques, similaire à l’équation (2). Nous montrons à l’aide de cette équation que les états propres sont multifractals, et calculons leurs dimensions fractales. La figure (3) montre le caractère fractal de la densité électronique. La “co-numérotation” est une façon de réarranger les positions atomiques, qui peut être considérée comme une sorte d’équivalent de la transformation de Fourier pour un cristal périodique. On peut donc considérer la figure (3) comme l’équivalent pour notre chaîne quasipériodique d’une représentation de la densité électronique dans la zone de Brillouin, et en fonction de l’énergie, pour une chaîne périodique.

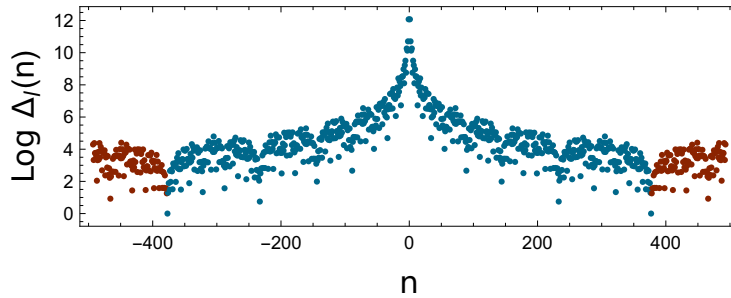


Figure 4. – Largeur des gaps spectraux d’une chaîne périodique approchant la chaîne quasipériodique de Fibonacci, en fonction de l’indice des gaps.

Dans une troisième partie, élargissant ensuite notre champ d’étude à un ensemble de chaînes quasipériodiques, nous nous intéressons au théorème d’indexation des gaps, qui décrit comment la géométrie d’une chaîne donnée contraint les valeurs que peut prendre la densité d’états intégrée

dans les gaps du spectre électronique. Ainsi par exemple, pour la chaîne de Fibonacci, le théorème prédit que la densité d'états de tout Hamiltonien "raisonnable" ne peut prendre dans les gaps que les valeurs

$$\text{idos} = n\tau^{-1} \pmod{1} \quad (3)$$

où n est entier, et $\tau = (1 + \sqrt{5})/2$ est le nombre d'or. Ainsi, tout gap peut être indexé de manière unique par un entier n , qui s'avère être un nombre d'enroulement topologique.

Nous nous intéressons à la façon dont l'énoncé de ce théorème est modifié lorsque l'on considère une séquence d'approximants périodiques approchant une chaîne quasipériodique. Nous montrons dans ce contexte qu'on peut distinguer des gaps stables restant ouverts à la limite quasipériodique, et des gaps transitoires, qui se ferment à la limite quasipériodiques. Le caractère stable/transient d'un gap est donné par la valeur de son indice n : les gaps d'indice trop grand (en rouge sur la figure (4)) étant transitoires.

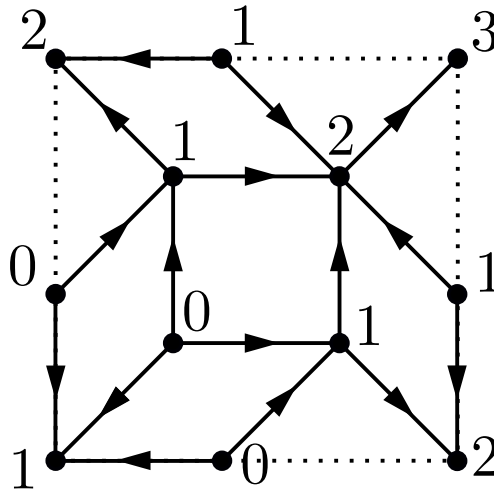


Figure 5. – Champ de flèches et champ de hauteurs sur un morceau du pavage quasipériodique d'Ammann-Beenker.

Enfin, dans une dernière partie, nous montrons comment des champs de hauteurs géométriques peuvent être utilisés pour construire des états électroniques exacts sur des pavages en une et deux dimensions. Plus précisément, nous définissons tout d'abord sur le pavage un champ de flèches irrotationnel, comme illustré sur la figure (5). Nous imposons que ce champ de flèches soit *local*, c'est-à-dire défini par l'agencement local des tuiles. Nous intégrons ensuite ce champ de flèches, obtenant ainsi une quantité scalaire définie en chaque sommet du graphe du pavage, que nous appelons le champ de hauteur, h . Nous utilisons alors ce champ de hauteur pour construire une fonction d'onde, sous la forme

$$\psi(m) = e^{\kappa h(m)}, \quad (4)$$

où κ est un paramètre libre. Nous montrons que cette fonction d'onde est état propre de hamiltoniens de la forme (1), pour les chaînes quasipériodiques construites par coupe et projection, et pour les pavages quasipériodiques bidimensionnels de Penrose (figure (1)) et d'Ammann-Beenker (figure (5)).

De façon remarquable, la localité du champ de flèches n'implique pas celle du champ de hauteur : il peut être distribué indépendamment de l'environnement local. C'est ce qu'illustre la figure (1): l'état représenté (qui est de type (4)) a une structure invariante d'échelle (donc non-locale), découplée de l'environnement local donné par le pavage sous-jacent. Quand ce découplage se produit, tout état $\psi(m) = e^{\kappa h(m)}$ construit avec le champ de hauteur h est multifractal.

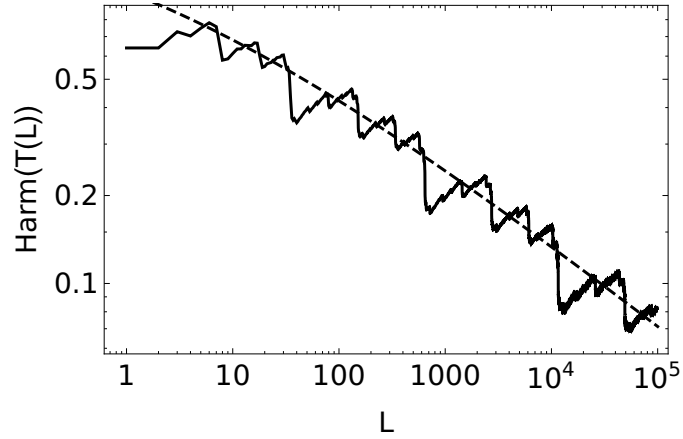


Figure 6. – Moyenne harmonique de la conductivité au niveau de Fermi d’un échantillon de taille L de la chaîne de Fibonacci. Tirets: prédiction théorique, ligne: calcul numérique.

Ces états sont robustes aux perturbations du hamiltonien, sous réserve que ces dernières respectent les symétries du pavage sous-jacent. Nous relierons les dimensions fractales de ces états à la distribution de probabilités des hauteurs, que nous calculons de façon exacte. Dans le cas des chaînes quasipériodiques, nous montrons que la conductivité suit une loi d’échelle de la taille de l’échantillon (figure (6)), dont l’exposant est relié à cette même distribution de probabilités.

Remerciements

J'ai eu la chance de rencontrer au cours de ma vie nombre de personnes extraordinaires qui ont su me communiquer leur passion pour la science. J'aimerais remercier en particulier deux de mes profs de prépa : Luc Abergel et Marc-Antoine Blain, pour nous avoir défendu l'idée audacieuse, que les maths et la physique sont plus qu'un outil de sélection aux concours.

Durant trois ans, le Laboratoire de Physique des Solides fut ma seconde maison. Je m'y suis senti comme chez moi, et cela grâce à tous ses membres, depuis le service informatique jusqu'à l'équipe théorie dans laquelle j'ai été accueilli à bras ouverts, en passant par toutes les autres équipes du laboratoire, qui interagissent ensemble avec bonheur, en particulier lors de événements qui rythment la vie du laboratoire : fête de la science, fête du laboratoire et journée des doctorants. Un merci tout particulier à la formidable équipe administrative, qui gère le labo avec une efficacité et une bonne humeur peu commune. Merci également à Fred B, mon "parrain" de thèse, qui m'a suivi avec bienveillance, et qui, épaulé par Fred R et par Wiebcke, m'a aidé et soutenu lors de mon passage à Ma Thèse en 180 Secondes. Merci encore à Marie-France, formidable instigatrice de la fête de la science, à laquelle j'ai participé chaque année avec plaisir aux côtés de Marianne.

Que serait l'équipe théorie, sans les permanents qui l'animent ? Je salue ici Gilles M, à la passion joyeuse et profonde pour la science, Mark, pour qui musique et physique riment harmonieusement, Khuôn-Viêt, qui m'a guidé dans le monde exigeant et passionnant de l'enseignement, Marc, aux vastes discussions éclairantes et éclairées, Pavel, à l'enthousiasme discret et communicatif, Pascal, à l'humour fin et caustique, Fred P, mon mentor, qui m'a toujours poussé à aller plus loin dans la quête de la compréhension des quasicristaux, et enfin tou-te-s les autres membres de l'équipe, qui ont contribué à leur manière à la vie du groupe. Pour conclure cette litanie, je remercie du fond du cœur Anu, ma directrice de thèse, dont je ne saurais trop vanter ici la profonde intuition physique, l'écoute et la gentillesse. Anu, ce doctorat fut fantastique, et c'est grâce à toi.

Doctorant-e-s et postdoctorant-e-s, vous êtes devenus au fil de ces trois ans de complicité bien plus que des collègues. Merci pour tous les moments partagés, au labo et en dehors. J'ai une pensée toute particulière pour Anaïs, théoricienne d'adoption et amie de longue date, pour Yunlong à la curiosité sans bornes, pour Fred aux remarques qui font mouche, pour Vardan, le plus français de tous les français, pour Oscar, fellow ArchLinuxian, pour Manali et Olesia, meilleures cobureau que je puisse imaginer, ainsi que pour Sergueï, sans qui ma productivité n'aurait pas été la même.

La physique n'est que l'un des nombreux aspects de ma vie de doctorant, et sans doute pas le plus important, comme je l'ai réalisé auprès de mes amis. Merci donc à Rémi, pour les balades en montagne, les rires et les soirées jeux, à Gabriel et Thibault, pour les concerts et festivals, à Nadia, Anaïs, Baur, et Nicolas pour les discussions et les expéditions multiples en France et ailleurs, à Thibaud dont je ne me lasse pas des propos décalés, émaillées d'imitations de personnalités diverses, à Pierre qui est trop loin, et dont la présence m'est chère (et je ne parle pas que du prix du billet d'avion), à Cécile, pour tous les moments de complicité et d'échange, à Laure la philosophe, pour les discussions souvent hautement intellectuelles mais toujours humaines, à Yann, pour les échanges délirants et sérieux à la fois. Merci enfin à mes inénarrables colocs, Aurélien, Guillaume, Sébastien et Charlotte pour les délires, et le soutien sans faille même dans

les moments les plus durs : ménage, concerts de l'Afreubo . . .

Durant les derniers mois de mon doctorat, Lucile a fait irruption dans ma vie, apportant beaucoup d'amour et un grain de folie. Lucile, grâce à toi, grâce à ton soutien constant (incluant la pénible relecture de mon manuscrit !) et à ta présence rayonnante, la difficile période de rédaction fut aussi à mes yeux la plus belle.

Last but not least, j'ai la chance incroyable d'avoir une famille aimante et attentive, qui m'a toujours encouragé en me laissant libre de mes choix. Maman, papa, Alix, Nani et Dod, merci.

Contents

Introduction	xiii
1. Building quasicrystals	1
1.1. Almost periodic functions	1
1.1.1. Repetitivity	2
1.1.2. Almost periodicity as periodicity in higher dimension	2
1.2. Quasiperiodic tilings	3
1.2.1. Repetitivity	4
1.2.2. The C&P method	4
1.2.3. Diffraction pattern of a C&P tiling	6
1.3. Quasiperiodic chains	8
1.3.1. Words and complexity	8
1.3.2. Sturmian words	9
1.4. Substitutions	10
1.4.1. 1D substitutions	10
1.4.2. 2D substitutions: the example of the Ammann-Beenker tiling	11
1.5. Conclusion	13
2. Electronic properties of the Fibonacci chain solved in perturbation theory	15
2.1. Introduction	15
2.2. Quantum chains	16
2.2.1. Bloch's theorem for tight-binding chains	16
2.2.2. Spectrum and eigenstates of the periodic chain	18
2.2.3. Multifractal analysis of the spectrum of the periodic chain	19
2.3. The Fibonacci chain: model and definitions	22
2.3.1. Approximants	22
2.4. Renormalization group and the multifractal nature of the Fibonacci spectrum	23
2.4.1. The perturbative renormalization group	23
2.4.2. Multifractal properties of the spectrum	25
2.5. Renormalization paths, equivalence between energy labels and conumbers.	26
2.6. Fractal dimensions of the eigenstates to first order	29
2.7. Higher order renormalization group and multifractality	31
2.7.1. Renormalization group for the eigenstates	31
2.7.2. Local eigenstate dimensions	32
2.7.3. The spectrally averaged fractal dimensions of eigenstates	34
2.7.4. The local spectral dimensions and their average	35
2.8. Relations between fractal dimensions and dynamical exponents	36
2.8.1. A relation between fractal dimensions	36
2.8.2. Quantum diffusion and spectral fractal dimensions	37
2.8.3. An upper bound for the diffusion moments	37
2.9. Conclusion and perspectives	38

3. Labeling gaps of quasiperiodic chains	39
3.1. The gap labeling theorem	39
3.2. Nearest neighbor tight-binding model on quasiperiodic chains	40
3.3. Application: the Fibonacci quasicrystal	40
3.3.1. Renormalization group and recursive gap labeling	41
3.3.2. Transient and stable gaps of the Fibonacci chain	42
3.4. Transient and stable gaps for generic Sturmian chains	44
3.5. Conclusion and perspectives	45
4. Some exact eigenstates on 1D and 2D quasiperiodic tilings	47
4.1. SKK state on the Fibonacci chain, and its properties	49
4.1.1. The Fibonacci chain and hopping Hamiltonian	49
4.1.2. The $E = 0$ eigenstate	50
4.1.3. Arrows and height field	50
4.1.4. Diffusion equation for the height function	52
4.2. Multifractal properties of SKK states	54
4.2.1. Fractal dimensions of a generic SKK state	54
4.2.2. The fractal dimensions of the $E = 0$ state of the Fibonacci chain	56
4.3. Transmission coefficient on the Fibonacci chain	56
4.4. SKK states on other aperiodic chains	58
4.4.1. SKK states on chains of the metallic mean series	58
4.4.2. Absence of SKK state on the b3 non-Pisot substitution	59
4.5. Discussion and conclusions for 1D chains	60
4.6. SKK states on 2D tilings and their properties	60
4.6.1. Tight-binding models on 2D tilings	61
4.6.2. Properties of the 2D height field. Fractal dimensions of the ground state.	62
4.6.3. Results for the AB tiling	65
4.6.4. A variational calculation for the ground state	69
4.6.5. Varying the on-site potential	70
4.6.6. Results for the Penrose tiling	72
4.6.7. Discussion and conclusions for 2D quasicrystals	74
4.7. Are the ground states of 1D chains SKK states?	74
4.7.1. SKK states and logarithmic derivative	75
4.7.2. Computing the logarithmic derivative	75
4.8. Conclusion and perspectives	77
5. Conclusions	79
A. Fractals	81
A.1. Scale invariance property	81
A.2. Measuring fractal set	82
A.2.1. The box-counting algorithm	82
A.2.2. The Hölder pointwise exponent	83
A.2.3. Multifractals and the generalized fractal dimensions	84
A.3. Computing fractal dimensions and the multifractal spectrum	87
A.4. Statistical physics and multifractal analysis	88
A.4.1. Multifractal analysis in the language of statistical physics	88
A.4.2. Rényi entropies and quenches	89
A.5. Discrete scale invariance and log-periodic oscillations	90

B. Properties of Sturmian sequences	91
B.1. Counting letters	91
B.2. Sturm functions	91
B.3. Mod 1 arithmetic and Sturmian sequences	92
B.3.1. Basic properties	92
B.3.2. Mod 1 arithmetic and internal space coordinates	92
B.3.3. Approximants	93
B.3.4. Approximants and conumbering	94
C. Brillouin-Wigner perturbation theory	97
D. Renormalization group for the eigenstates of the Fibonacci chain	99
E. Variational method	101
E.0.1. The variational energy	101
E.0.2. The variational equations	102

Introduction

The structures the most studied in condensed matter physics are either crystalline (periodic), or amorphous (disordered). However, in this thesis we study quasicrystals, systems which neither crystalline nor amorphous, which are in some sense in between the two. Before motivating this study on physical grounds, we briefly present quasiperiodicity, via a “real life” example taken from [Bédaride and Fernique \[2013\]](#).

Having decided to re-tile your bathroom, you go to the closest department store, where two types of tiles are available: squares and a rhombuses (Fig. (1a)). They are accompanied by the following intriguing offer: “Pay cash for squares – and get all the rhombuses you want for free!”.

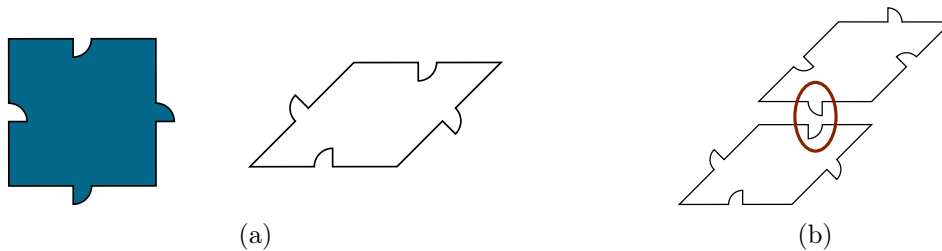


Figure 1. – (a): The two tiles available at the store. (b): A forbidden configuration.

Wanting to re-tile your bathroom in the cheapest possible way, you briefly think of taking only the free rhombuses, before realizing that because of the notches on the edges of the tiles, tiling with rhombuses only is not possible, as shown on Fig. (1b). So, you need at least some squares to accommodate the rhombuses. A tiling with squares only would be possible but that would of course be a loss of money. What is the cheapest possible tiling, i.e., what is the largest possible fraction of free rhombuses on can introduce? After thinking about it, you realize (see [Bédaride and Fernique \[2013\]](#)) that the cheapest tiling has $\sqrt{2} \simeq 1.4$ rhombus per square, and looks like this:

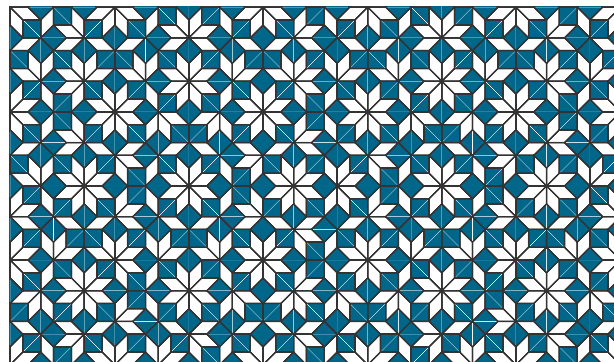


Figure 2. – A patch of the Ammann-Beenker tiling (notches were omitted).

This tiling, called the *Ammann-Beenker tiling*, has curious properties. It must be *aperiodic* since the number of rhombuses per square is not rational, however, it looks *almost* periodic, in the sense that it almost overlap with a copy of itself translated by a well-chosen vector, as seen

Introduction

on Fig. (3). The Ammann-Beenker tiling is an example of a *quasiperiodic tiling*: an aperiodic yet long-range ordered structure.

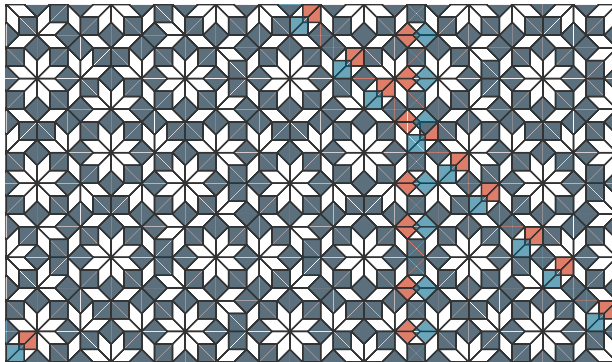


Figure 3. – Ammann-Beenker tiling (blue) almost overlapping with its translated copy (red).

It is part of the larger family of the *aperiodic tilings*, whose origin can be traced back to 1961, when the logician Hao Wang and his student Robert Berger started working on the following question: *Is the tiling problem decidable?* In other words, is there an algorithm which, when provided with a set of tiles, returns “yes” or “no” depending on whether one can tile the plane with them or not. Robert Berger proved in 1964 that no such algorithm can be written, and his proof involved the construction of a set of 20,426 tiles that can only be used to tile the plane aperiodically (see Berger [1966]). The first aperiodic tiling was born.

The Penrose tiling is perhaps the most famous example of aperiodic tiling. It is made of “fat” and “thin” rhombuses decorated with arrows, as shown on Fig. (4a). Two tiles can be adjacent if their arrows match on the edge they share. Assembling them according to this rule necessarily produces the Penrose tiling, a patch of which is shown on Fig. (4b). The tiling’s edges have 10 possible orientations, and it turns out they all occur with the same probability: the Penrose tiling is thus 10-fold symmetric. One can show that this symmetry is forbidden for a periodic structure (see e.g. the introduction of Baake and Grimm [2013]). Therefore, by relaxing the periodicity constraint, one gains access to a broader class of symmetries. Furthermore, just like the Ammann-Beenker tiling, the Penrose tiling is quasiperiodic and possesses almost periods.

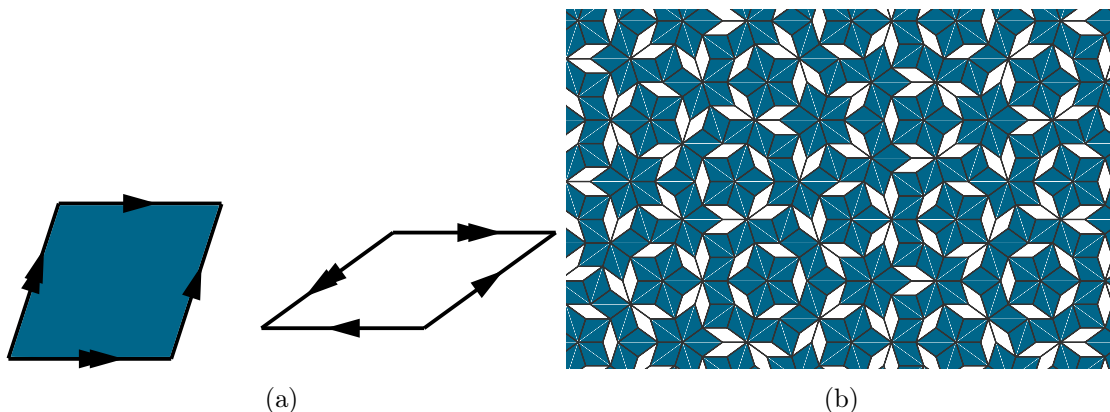


Figure 4. – (a): The two tiles of the Penrose tiling. (b): A patch of the Penrose tiling (arrows were omitted).

In the eighties, quasiperiodic tilings made their appearance in the realm of physics. In April 1982, Dan Shechtman was analyzing a series of rapidly solidified AlMn samples he had produced, when he noticed something strange: electron diffraction of some samples showed Bragg peaks – signature

of a long-range ordered structure – together with a 10-fold symmetry – incompatible with a periodic crystalline structure. At that time, no structures apart from crystals were known to yield Bragg peaks, hence the initial puzzlement of Shechtman and of the physics community at large. Shechtman and his collaborators later understood (Shechtman et al. [1984]) that the atoms in such alloys organized in a quasiperiodic fashion, forming a structure similar to the Penrose tiling. For his discovery, Shechtman was awarded the Wolf prize in 1999 and the Nobel prize in chemistry in 2011. Experimentalists soon discovered new alloys showing crystallographically forbidden symmetries: a 12-fold symmetric NiCR structure Ishimasa et al. [1985], another type of 10-fold symmetric AlMn structure Bendersky [1985], and 8-fold symmetric WNiSi and CrNiSi phases Wang et al. [1987]. Such structures, organized in a quasiperiodic fashion, are called *quasicrystals*. Note that quasicrystals need not exhibit non-crystallographic symmetries Feng et al. [1990]. Quasiperiodic structures are not restricted to intermetallic alloys: they also spontaneously form in soft matter systems, see e.g. Iacovella et al. [2011] and references therein. Finally, let us mention that quasiperiodic structures have been artificially engineered, see e.g. Gellermann et al. [1994], Tanese et al. [2014].

What are the optical, acoustic, magnetic, electronic transport properties of quasicrystals? How do these properties vary with temperature, pressure, ... What happens at the interface between a quasicrystal and another material? All these questions, that are of interest when studying crystals, can be asked again in the case of quasicrystals. Although 35 years have passed since their discovery, the questions listed above are still vastly unexplored from a theoretical point of view. Indeed, with quasicrystalline structures being one the one hand too far from periodicity for Bloch's theorem to apply, and the other hand too correlated for the tools from disordered system to be relevant, theoreticians are deprived of their favorite tools for handling condensed matter problems. But if quasicrystals are so hard to approach theoretically, this may be a good sign that the physics of these systems is new and interesting.

In this thesis, we study toy models for non-interacting electrons on simple 1D and 2D quasiperiodic tilings. The interest for such models is not new, and is in fact *anterior* to the experimental discovery of quasicrystals (see Kohmoto et al. [1983] and references therein). In these systems one can find devil's staircase-like energy spectra, fractal eigenstates ... strange structures seldom appearing in physically reasonable systems! How does these unusual properties stem from quasiperiodicity? This is the question we want to address in this thesis.

In Chap. 1, we present recipes for constructing quasiperiodic tilings, and we discuss their basic geometrical properties. In particular, we argue that quasiperiodic tilings are, among aperiodic tilings, the closest to being periodic.

In Chap. 2, we examine everyone's favorite example of 1D quasiperiodic system: the Fibonacci chain. With the help of a perturbative renormalization group, we explain how the fractality of the spectrum and eigenstates emerges from the scale-invariance properties of the chain. This chapter is based on Macé et al. [2016].

In Chap. 3, we discuss one of the few exact results available for quasiperiodic chains: the gap labeling theorem, relating the integrated density of states' values to the geometry of the chain. We discuss in particular the gap labeling in finite chains, and the passage to the infinite size limit. We discuss how the labeling depends on the geometry of the chain by considering different examples. This chapter is based on Macé et al. [2017].

In Chap. 4, we present exact solutions for some eigenstates of hopping models on one and two dimensional quasiperiodic tilings and show that they are critical, fractal states, by explicitly computing their multifractal. These eigenstates are shown to be generically present in 1D quasiperiodic chains. We then describe properties of the ground states for a class of tight-binding Hamiltonians on the 2D Penrose and Ammann-Beenker tilings. This chapter is based on Macé et al. [2017]

Definitions and conventions used in this thesis

Name(s)	Notation(s)	Definition
Floor <i>or</i> Integer part	$\lfloor x \rfloor$	largest integer smaller or equal to x
Ceiling	$\lceil x \rceil$	smallest integer larger or equal to x
Modulo <i>or</i> Remainder	$x \bmod y$	$x - \left\lfloor \frac{x}{y} \right\rfloor y$
Fractional part	$\{x\}$	$x - \lfloor x \rfloor$
Fourier transform	$F(f)(k)$ or $\hat{f}(k)$	$\int_{\mathbb{R}} f(x) e^{-ikx} dx$
Inverse Fourier transform	$F^{-1}(\hat{f})(x)$ or $\check{f}(x)$	$\int_{\mathbb{R}} \hat{f}(k) e^{ikx} \frac{dk}{2\pi}$
Energy index	a	\emptyset
Position index	m or n	\emptyset
Number of inflations	l or t	\emptyset

Chapter 1.

Building quasicrystals

In this chapter, we describe *quasiperiodic tilings*, which we use to model quasicrystals.

We first introduce *almost periodic functions*, and describe their fundamental properties: *repetitivity*, *almost periodicity* and *periodicity in higher dimension*. We next introduce quasiperiodic tilings and argue that they can be viewed as discrete counterparts of quasiperiodic functions. In particular, we discuss how many quasiperiodic tilings can be seen as cuts of higher dimensional periodic lattices, via the *cut-and-project method*. We show on a simple example that the diffraction figure such tilings exhibit *Bragg peaks* – signature of a long-range order –, a feature which is experimentally observed in quasicrystals. We then examine in more details the properties of 1D quasiperiodic tilings, and argue that they are the aperiodic tilings which are *the closest to being periodic*. Finally, we introduce *substitution methods* that can be used to build many quasiperiodic tilings.

Contents

1.1. Almost periodic functions	1
1.1.1. Repetitivity	2
1.1.2. Almost periodicity as periodicity in higher dimension	2
1.2. Quasiperiodic tilings	3
1.2.1. Repetitivity	4
1.2.2. The C&P method	4
1.2.3. Diffraction pattern of a C&P tiling.	6
1.3. Quasiperiodic chains	8
1.3.1. Words and complexity	8
1.3.2. Sturmian words	9
1.4. Substitutions	10
1.4.1. 1D substitutions	10
1.4.2. 2D substitutions: the example of the Ammann-Beenker tiling	11
1.5. Conclusion	13

1.1. Almost periodic functions

An almost periodic function is a superposition of harmonics:

$$f(x) = \sum_n c_n e^{ik_n x}. \tag{1.1}$$

In particular, periodic functions like $\cos(x)$ are almost periodic. Almost periodic functions also include aperiodic functions like

$$f(x) = \cos(x) + \cos(\tau^{-1}x), \quad (1.2)$$

where $\tau = (1 + \sqrt{5})/2$ is the golden ratio. The choice of the golden ratio is arbitrary: replacing it by any other irrational number would also cause the function f to be almost periodic.

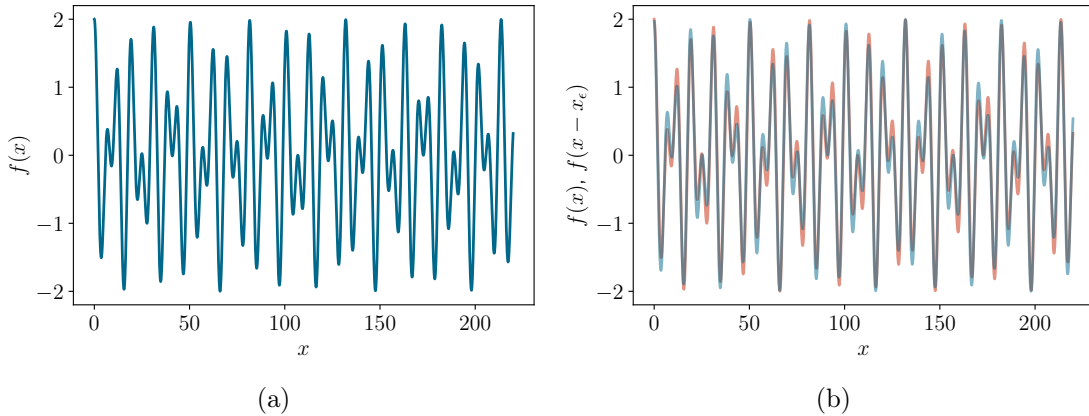


Figure 1.1. – (a): The almost periodic function (1.2). (b): The almost periodic function (in red) superimposed with its translate (in blue).

1.1.1. Repetitivity

Fig. (1.1a) shows a plot of this function, which indeed looks “almost” periodic: the patterns of the graph of the function almost repeats themselves everywhere: almost periodic functions are highly *repetitive*. Almost periodic functions have the property that they almost overlap with copies of themselves translated by appropriately vectors, as shown by Fig. (1.1b). More precisely, one can find ϵ -almost periods x_ϵ such that

$$|f(x - x_\epsilon) - f(x)| \leq \epsilon \quad (1.3)$$

for ϵ as small as we want. For the almost period $x_\epsilon = 50$ shown on Fig. (1.1b), we have $\epsilon \simeq 0.26$.

1.1.2. Almost periodicity as periodicity in higher dimension

Consider the periodic function

$$\tilde{f}(x, y) = \cos(x) + \cos(y) \quad (1.4)$$

whose contour plot is shown on Fig. (1.2). The almost periodic function introduced earlier (Eq. (1.2)) can be expressed as

$$f(x) = \tilde{f}(x, \tau^{-1}x) \quad (1.5)$$

Thus, our almost periodic function f can be seen as a cut of the 2D periodic function \tilde{f} along the line $y = \tau^{-1}x$, as shown on Fig. (1.2). In general *almost periodic functions can be seen as cuts of periodic functions in higher dimension*. This property also holds for quasiperiodic tilings, which can be seen as cuts of higher dimensional periodic tilings.

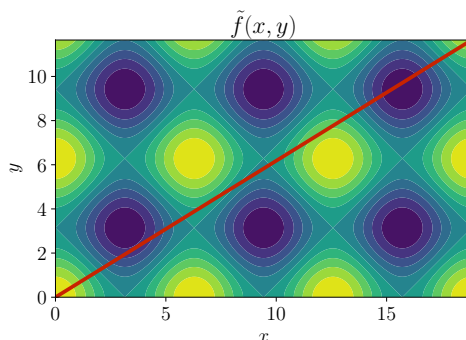


Figure 1.2. – The almost periodic function (1.2) can be seen as a cut (in red) of the 2D periodic function (1.4).

1.2. Quasiperiodic tilings

A tiling is an arrangement of non-overlapping tiles covering the plane. It can be periodic, or aperiodic. Quasiperiodic tilings are a specific class of aperiodic structures which can be viewed as discrete counterparts of almost periodic functions. Throughout this section, we take the example of the quasiperiodic Ammann-Beenker tiling [Ammann et al. \[1992\]](#), involving lozenges and squares, as shown on the left part of Fig. (1.3a).

Such tilings are interesting for physicists as they model quasicrystals. The right part of Fig. (1.3a) shows such a model: atoms are placed at the apexes of the tiles, and the edges of the tiles represent chemical bonds between the atoms. In the remainder of this thesis, we will indifferently call “tiling” a covering of the plane by tiles (left part of Fig. (1.3a)) or the corresponding model of atoms (right part of Fig. (1.3a)).

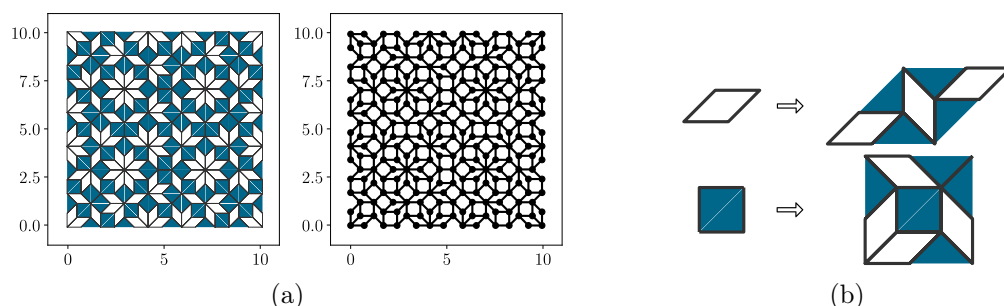


Figure 1.3. – (a): Left: a piece of the quasiperiodic Ammann-Beenker tiling. Right: the corresponding model of atoms. Lengths are expressed in units of the nearest neighbors distance. (b): The inflation rules used to produce the quasiperiodic Ammann-Beenker tiling (see text for the details).

The Ammann-Beenker tiling, like many other quasiperiodic tilings, can be produced by the *substitution (or inflation) method*:

1. Start with a given tile or arrangement of tiles
2. Replace every tile in the arrangement by a set of tiles, following a predetermined set of rules (see e.g. Fig. (1.3b))
3. Repeat step 2.

The substitution method is discussed in more details in Sec. 1.4. For the moment let us just use it to prove that the Ammann-Beenker tiling is indeed aperiodic. As seen on Fig. (1.3b) substitution

replaces a rhombus by 3 rhombuses and 2 squares, while it replaces a square by 4 rhombuses and 3 squares. Therefore, if the number of rhombuses and squares is respectively N_R and N_S in a given tiled region, then the number of rhombuses and squares in the inflated region is

$$\begin{pmatrix} N'_R \\ N'_S \end{pmatrix} = \begin{bmatrix} 3 & 4 \\ 2 & 3 \end{bmatrix} \begin{pmatrix} N_R \\ N_S \end{pmatrix}. \quad (1.6)$$

The matrix introduced here is called the *substitution matrix* (or inflation matrix) of the tiling. To create larger and larger patches of the Ammann-Beenker tiling, one can apply the substitution rule repetitively to an initial tiled region. After an asymptotically large number of substitutions, the number of rhombuses per square on the patch is given by the ratio of the two components of the eigenvector of the substitution matrix associated with the largest eigenvalue. One finds here $N_R/N_S \sim \sqrt{2}$. Therefore, there are $\sqrt{2}$ rhombuses per square on the Ammann-Beenker tiling. This fraction is irrational, thus proving that the Ammann-Beenker tiling is aperiodic.

1.2.1. Repetitivity

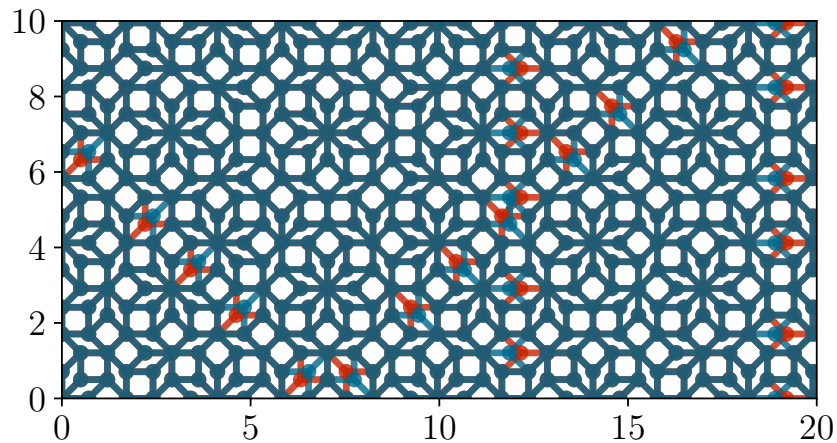


Figure 1.4. – A piece of the quasiperiodic Ammann-Beenker tiling (blue) superimposed with a translate of itself (red). The two pieces “almost” perfectly superimpose, differing only along lines.

Quasiperiodic tilings share with almost periodic functions the *repetitivity* property: every pattern (arrangement of tiles) present in the tilings repeats, as can be seen on Fig. (1.3a). Furthermore, quasiperiodic tilings are *almost periodic*, in exactly the same sense as quasiperiodic functions: a copy of the tiling translated by a carefully chosen vector overlaps almost everywhere with itself. Fig. (1.4) illustrates this property for the Ammann-Beenker tiling.

1.2.2. The C&P method

Fig. (1.5) displays a portion of the Ammann-Beenker tiling, with each edge colored differently according to its orientation. Remark that only 4 orientations are present in the tiling. One can associate to each of these 4 orientations one of the 4 unit vectors of \mathbb{R}^4 . Let us for example choose the mapping:

$$\begin{aligned} (1, 0, 0, 0) &\leftrightarrow \text{horizontal edges (in green)} \\ (0, 1, 0, 0) &\leftrightarrow \pi/4 \text{ inclined edges (yellow)} \\ (0, 0, 1, 0) &\leftrightarrow \text{vertical edges (red)} \\ (0, 0, 0, 1) &\leftrightarrow 3\pi/4 \text{ inclined edges (blue)} \end{aligned} \quad (1.7)$$

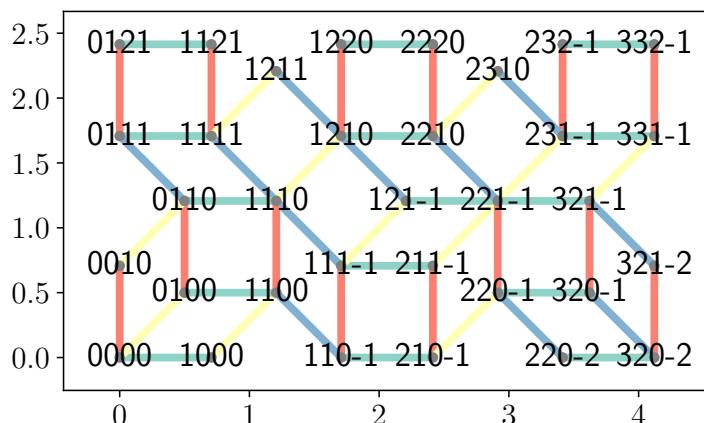


Figure 1.5. – A portion of the Ammann-Beenker tiling, with each edge colored differently according to its orientation. Nodes are labeled with their 4D coordinates (see text for the details).

Mapping all the edges, the whole tiling is lifted to a 4D “staircase-like” surface. In particular, every node of the tiling corresponds to a point of integer coordinates in 4D, as shown on Fig. (1.5)). Said differently, the points of the quasiperiodic Ammann-Beenker tiling can be interpreted as projections of points of \mathbb{Z}^4 , the periodic square tiling in 4D.

Just like almost periodic functions, many quasiperiodic tilings – including the Ammann-Beenker tiling – have the property of being interpreted as cuts of *periodic* lattices when lifted to a higher dimensional space.

One can construct quasiperiodic tilings the other way around, using the so-called cut-and-project (C&P) method. We restrict ourselves to what is often called the “canonical” C&P method, which we describe now:

1. Choose a higher dimensional space E of dimension D , hosting a D -dimensional hypercubic lattice.
2. Choose a d -dimensional subspace $E_{\parallel} \subset E$, which will host the quasiperiodic tiling. We shall often loosely refer to the E_{\parallel} subspace as the *slope* of the tiling.
3. Select the lattice points falling in the infinite “slice” obtained by translating the unit cell of the lattice along E_{\parallel} ,
4. project these points to E_{\parallel} .

It is not our purpose here to describe the C&P method in its full generality; the interested reader can find a more detailed exposition in the articles [Kalugin et al. \[1985\]](#), [Duneau and Katz \[1985\]](#), [Elser \[1986\]](#) or in the book [Baake and Grimm \[2013\]](#).

Fig. (1.6) shows the canonical C&P method in the case $D = 2$, $d = 1$. In that case, the higher dimension lattice is a 2D cubic lattice. The unit cell (shown in bold on the figure) is translated along the line E_{\parallel} , of slope $\alpha = \tau^{-1}$ where τ is the golden ratio. The lattice points falling in the so produced slice are shown in blue. They are then projected onto E_{\parallel} , yielding a chain of points called the *Fibonacci chain*.

Along the Fibonacci chain, nearest neighbors are either separated by a “large” or a “short” distance, represented respectively by single and double lines on Fig. (1.6), and corresponding respectively to projections of horizontal or vertical edges of the square lattice. If the slope α had been rational, say $\alpha = p/q$, the line E_{\parallel} would have intercepted the lattice point of coordinates (q, p) . Therefore, the chain on E_{\parallel} would have been *periodic*, of period $p + q$ since the slice selects q horizontal and p vertical edges going from the origin to the point (q, p) . In the case of the

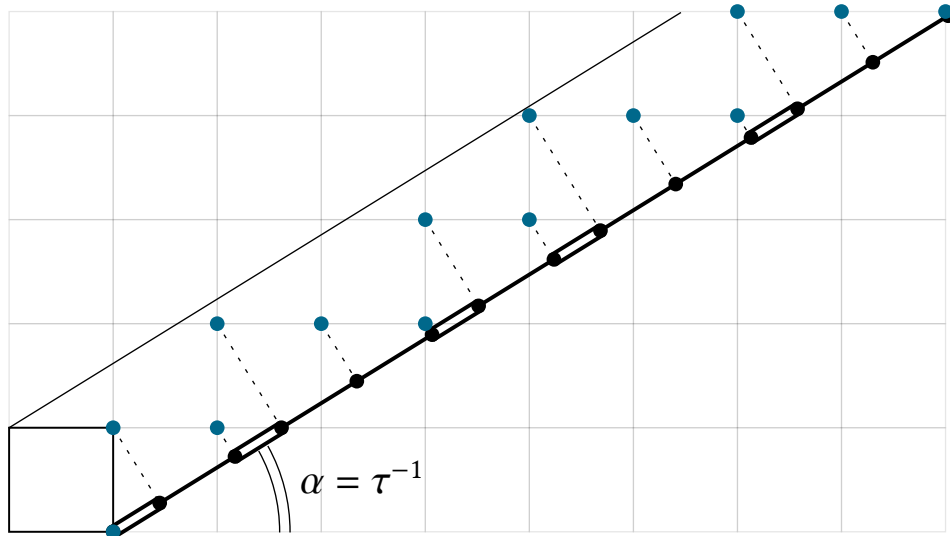


Figure 1.6. – The cut and project method used to construct the Fibonacci quasiperiodic chain.

Fibonacci chain, the slope is irrational, $\alpha = \tau^{-1}$. Therefore, E_{\parallel} intercepts no lattice point except the origin. Thus, the chain is *aperiodic*, and in fact *quasiperiodic*, as we shall see later. In this thesis, a quasiperiodic chain of irrational slope α produced in that way is referred to as a canonical C&P chain, or as a Sturmian chain. This last denomination is justified in Sec. 1.3.

Quasiperiodic tiling	D	d
canonical C&P chains	2	1
Ammann-Beenker	4	2
Penrose	5	2

Table 1.1. – The different quasiperiodic tilings studied in the thesis.

Table (1.1) presents the different C&P tilings that will focus on here. Canonical C&P chains (and in particular the Fibonacci chain) will be studied in Chap. 2, 3 and 4 while the two-dimensional Ammann-Beenker and Penrose tilings will be studied in Chap. 4.

1.2.3. Diffraction pattern of a C&P tiling.

For the moment, we define a quasiperiodic tiling as an aperiodic tiling with some kind of long range order, as evidenced by the fact that the tiling almost overlaps with a copy of itself translated. From a physical point of view, performing a diffraction experiment can reveal the long range order of a structure. Based on this observation, we introduce the following definition of a quasicrystal.

Definition 1 (Quasicrystal) *A quasicrystal is a material which is both aperiodic – in at least one direction of space – and long range ordered. The latter is manifested by the occurrence of sharp spots in its diffraction pattern.*

In this part we compute the diffraction pattern of the C&P chains introduced earlier, and show that it consists of Bragg peaks. This motivates the use C&P tilings to model quasicrystals. This remark was made very early in the development of quasicrystals theory, see Kalugin et al. [1985], Duneau and Katz [1985], Levine and Steinhardt [1986], Elser [1986].

We shine light on a chain of atoms, modeled by point-like particles perfectly reflecting light. According to Huygens–Fresnel principle, and disregarding light interference within the sample,

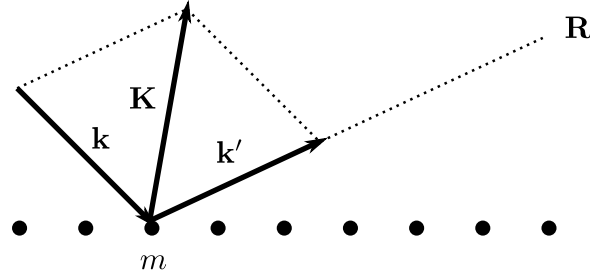


Figure 1.7. – Schematic setup of the diffraction experiment of a chain of atoms: the incident wave has wavevector \mathbf{k} , and \mathbf{k}' is the wavevector of the wave emitted by atom m towards the observation point \mathbf{R} . $\mathbf{K} = \mathbf{k}' - \mathbf{k}$ is the scattering vector.

the amplitude diffracted at point \mathbf{R} by the m^{th} atom, located at point $\mathbf{r}(m)$, is

$$\psi(\mathbf{R}) = A_0 e^{-i(\mathbf{k} \cdot \mathbf{r}(m) + \mathbf{k}' \cdot (\mathbf{R} - \mathbf{r}(m)))}, \quad (1.8)$$

where $A_0 = \sqrt{I_0/N}$, with I_0 the total intensity of the incident beam. Introducing the scattering vector $\mathbf{K} = \mathbf{k}' - \mathbf{k}$, as shown on Fig. (1.7), one gets

$$\psi(\mathbf{R}) = A_0 e^{-i\mathbf{k}' \cdot \mathbf{R}} e^{i\mathbf{K} \cdot \mathbf{r}(m)} \quad (1.9)$$

Let us write $\mathbf{K} \cdot \mathbf{r}(j) = Kr(j) \cos \vartheta = k_\vartheta r(j)$, with $k_\vartheta = K \cos \vartheta$. We are interested the total diffracted amplitudes, which writes¹

$$A(\vartheta) = \sum_j e^{ik_\vartheta r(j)}. \quad (1.10)$$

This sum is a priori not easy to evaluate since the function $r(j)$ giving the position of the atom is non-trivial for a quasiperiodic chain, as can be seen on Fig. (1.6). However, using the C&P construction, we can instead sum over the points of the square lattice falling in the band:

$$A(\vartheta) = \sum_{\mathbf{r} \in \text{band}} e^{ik_\vartheta r_{\parallel}(m,n)} \quad (1.11)$$

where r_{\parallel} is the parallel coordinate of the square lattice point \mathbf{r} . We recall that if the slope of the C&P tiling is $\alpha = \tan \theta$, then the parallel and perpendicular coordinates of the square lattice point $\mathbf{r} = (m, n)$ are

$$\begin{pmatrix} r_{\parallel} \\ r_{\perp} \end{pmatrix} = \begin{bmatrix} \cos \theta & \sin \theta \\ -\sin \theta & \cos \theta \end{bmatrix} \begin{pmatrix} m \\ n \end{pmatrix} \quad (1.12)$$

Restricting the sum to the band complicates the computation. Let us instead sum over all lattice points and weight the sum by the function $\mathbb{1}_W(r_{\perp})$ that takes value 1 if point \mathbf{r} is inside the band, and 0 otherwise:

$$A(\vartheta) = \sum_{\mathbf{r} \in \mathbb{Z}^2} e^{ik_\vartheta r_{\parallel}} \mathbb{1}_W(r_{\perp}) \quad (1.13)$$

Explicitly,

$$\mathbb{1}_W(r_{\perp}) = \begin{cases} 1 & \text{if } 0 \leq r_{\perp} < W \\ 0 & \text{otherwise} \end{cases} \quad (1.14)$$

1. dropping the constant prefactor $A_0 e^{-i\mathbf{k}' \cdot \mathbf{R}}$

where W is the width of the band: $W = \cos \theta + \sin \theta$. Performing sum over a lattice is made easy by the *Poisson summation formula* relating the sum of a function over a lattice to the sum of its Fourier transform:

$$\sum_{\mathbf{r} \in \mathbb{Z}^2} f(\mathbf{r}) = \sum_{\mathbf{p} \in 2\pi\mathbb{Z}^2} \hat{f}(\mathbf{p}) \quad (1.15)$$

Applying the Poisson summation formula to our case, and performing the Fourier transform, one gets

$$A(\vartheta) = 2\pi W \sum_{\mathbf{p} \in 2\pi\mathbb{Z}^2} \delta(p_{\parallel} - k_{\vartheta}) e^{-iWp_{\perp}/2} \operatorname{sinc}\left(\frac{Wp_{\perp}}{2}\right) \quad (1.16)$$

Now, the diffracted intensity being the modulus squared of the diffracted amplitude: $I(\vartheta) = \lim_{N \rightarrow \infty} I_0 |A(\vartheta)|^2 / N$, we get

$$I(\vartheta) \propto I_0 \sum_{\mathbf{p} \in 2\pi\mathbb{Z}^2} \delta(p_{\parallel} - k_{\vartheta}) \operatorname{sinc}^2\left(\frac{Wp_{\perp}}{2}\right) \quad (1.17)$$

So, the diffraction spectrum of any canonical C&P chain consists purely of Bragg peaks, as announced. It is clear from this simple calculation that the origin of the Bragg peak structure is the underlying higher dimensional lattice. A similar calculation would yield a Bragg peak diffraction spectrum for any other C&P tiling.

Let us consider the particular case $\alpha = 0$. In that case the chain is not quasiperiodic, but periodic. Bragg peaks are located at Fourier space positions $p_{\parallel} = 2\pi m$ with m integer. Therefore, the Bragg peaks are indexed by a single integer, and their set forms a lattice.

Let us now consider the case of a quasiperiodic chain, i.e. the case $\alpha = \tan \theta$ irrational. Let us consider for example the case $\alpha = 1/\sqrt{2}$. Then Bragg peaks are located at Fourier space positions $p_{\parallel} \propto \sqrt{2}m + n$, with m and n integers. Therefore, the Bragg peaks are indexed by two integers, and their set is not a lattice, but a dense set.

These results are generic, and are summed up in Tab. (1.2).

	Periodic	Quasiperiodic
Diffraction spectrum	Bragg peaks	Bragg peaks
Set of Bragg peaks	discrete (lattice)	dense
Indexed by	d integers	$D > d$ integers

Table 1.2. – Properties of the diffraction spectrum for d dimensional periodic and quasiperiodic sets of atoms.

1.3. Quasiperiodic chains

Quasiperiodic tilings are somehow in between periodic and disordered tilings. Are they closer to periodic or to disordered tilings? In this section, we try to give an answer to this yet ill-posed question, in the context of C&P chains introduced earlier.

1.3.1. Words and complexity

As we have seen before (see Fig. (1.6)), canonical C&P chains involve two distances, that are shown as single and double bonds on the figures. Let us associate to the single bond (large distance) the letter A and to the double bond the letter B, as shown on Fig. (1.8). To every chain of two lengths we can associate a word of two letters, and vice-versa.

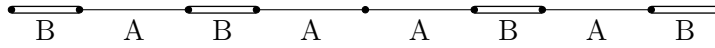


Figure 1.8. – A piece of the Fibonacci chain and the corresponding word.

Let w be an infinite word, i.e. an infinite succession of letters A and B. We are actually going to work mainly with semi-infinite words here, but results derived here can easily be extended to infinite words, as done for example in [Fogg \[2002\]](#). A *factor of length N* of w is a succession of N contiguous letters appearing in the word. For example, AB is a factor of length 2 of the word $w = BABAA\dots$, as it appears after the first letter of w . We define the *complexity* $\Omega(w, N)$ as the number of distinct factors of length N appearing in w .

Obviously the complexity function cannot grow faster than 2^N but how slowly can it grow? To answer the question, we consider an infinite (or semi-infinite) word, and we construct the *tree of words* [Kellendonk and Savinien \[2012\]](#), [Julien et al. \[2015\]](#): a tree graph constructed as follows. Vertices at level N list the factors of length N . A factor v of the level $N - 1$ shares an edge with a factor w of the level N if w can be constructed by adding one letter to the right of v . For example, consider, the periodic word w of period AB: $w = ABAB\dots$. Its tree of words is shown on Fig. (1.9).

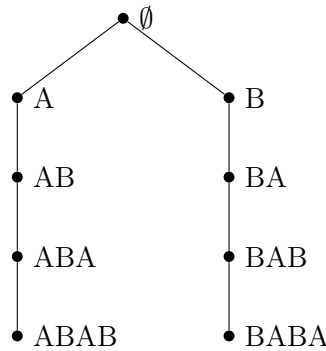


Figure 1.9. – The first levels of the tree of words of the periodic word ABAB...

Remark that the tree of this periodic word does not grow after level $N = 1$ ($N = 0$ is the root of the tree). In general, *a word is periodic of period N if and only if its tree stops growing at level $N - 1$* . Indeed, suppose that at level $N - 1$ on the tree of a given word w , each vertex has only one child. Then there is only one way of adding a letter to the right of any factor of length $N - 1$. But then, there is again only one way to add a letter to the right of a subword of the length N , and by recursion the tree stops growing starting from level N . Thus, w is periodic of period N . We conclude: *A word ω is aperiodic if and only if its complexity function grows at least linearly. More precisely,*

$$\boxed{\Omega(\text{aperiodic word}, N) \geq N + 1} \tag{1.18}$$

This is the Morse–Hedlund theorem, which is commented in more details in [Fogg \[2002\]](#).

1.3.2. Sturmian words

Words whose complexity grows the slowest (i.e. linearly) – and which are in this sense the closest to being periodic – are called *Sturmian words*.

The Fibonacci word is an example of Sturmian word. Fig. (1.10) shows the first levels of the tree of the Fibonacci word, and one can indeed check that the tree width grows linearly.

It is easy to understand that *all C&P words are Sturmian*. Take an irrational number, and consider the word produced by the C&P method. We set as shown on Fig. (1.6) the origin of our

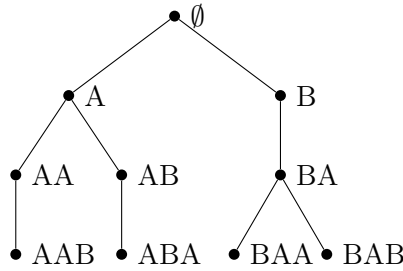


Figure 1.10. – The first levels of the Fibonacci tree of words.

chain at the (unique) point where the slope E_{\parallel} intersects \mathbb{Z}^2 . To enumerate the possible factors of length N , we translate the slope along its normal direction, and consider the set of words of length N that appear on the right of the origin. This set is exactly the set of factors of length N , because translating the slope while keeping the origin fixed amounts to translating the origin while keeping the slope fixed. When we translate the slope, we pass from one word to the next by what is called a *phason flip*. Two phason flips cannot occur at the same time, since the slope is irrational. Moreover, after having translated the slope along one unit cube of \mathbb{Z}^2 , we are back to the original setup, and in the interval of N letters we consider, $N + 1$ phason flips have occurred, yielding at most $N + 1$ different words of length N . Thus the complexity is at most $N + 1$. It cannot be less, because the word is aperiodic. We conclude it is exactly $N + 1$.

In fact it turns out that *the Sturmian words are exactly the C&P words.*, as proved in Chap. 6 of Fogg [2002]. This result corroborates our intuition that C&P tilings are the least complex among aperiodic tilings, and in this sense, the closest to being periodic.

1.4. Substitutions

In this last section, we describe in more details the Ammann-Beenker substitution rule introduced earlier, after briefly showing how some Sturmian chain can be constructed by substitution.

1.4.1. 1D substitutions

Constructing the Fibonacci chain by substitution

Consider the following *substitution rule*:

$$S : \begin{cases} A \rightarrow AB \\ B \rightarrow A \end{cases} \quad (1.19)$$

Starting with a finite word $w_0 = B$, we can apply the substitution rule to obtain a series of longer and longer chains : $w_1 = S(C_0) = B$, $w_2 = S(C_1) = AB$, $\dots w_l = S^l(C_0)$. The semi-infinite chain w_{∞} coincides with the C&P chain obtain by keeping on Fig. (1.6) the part of the chain to the right of the projection of point $(0, 1)$. The (bi)infinite Fibonacci chain can also be produced by applying the same substitution on the initial word $w'_0 = B|A^2$: $w'_1 = S(B)|S(A) = A|AB$, $w'_2 = S(A)|S(AB) = AB|ABA$, \dots We shall indifferently refer to w_{∞} and to w'_{∞} as “the” Fibonacci chain, disregarding the differences between infinite and semi-infinite chains. For a more detailed discussion, the reader is referred to Chap. 4 of Baake and Grimm [2013].

2. The bar marks the origin, corresponding to the point $(0, 1)$ on Fig. (1.6)

Substitution and scale invariance

In the C&P picture, A and B letters are represented by long and small segments, whose ratio of lengths L_B/L_A is equal to the golden ratio $\tau = (1 + \sqrt{5})/2$. Therefore, from a geometrical point of view, the substitution transforms a small segment of length L_B into a segment whose length L_A is τ times larger. Similarly, it transforms a large segment of length L_A into a segment whose length $L_A + L_B$ is again τ times larger. Therefore, the substitutions rescales the lengths by a factor of τ . Since the infinite Fibonacci chain is by construction invariant under the substitution, it has a scale invariance property. This scale invariance property will be exploited in Chap. 2 to explain the multifractal nature of the spectrum and eigenstates of a quantum model built on the Fibonacci chain.

Constructing Sturmian chains by substitution

We have seen that the Fibonacci chain can be constructed by substitution. Is this true for every canonical C&P chain? The following theorem Yasutomi [1999] answers in the negative.

Theorem 1 *A Sturmian word can be obtained by substitution if and only if its slope α is a quadratic irrational and if its intercept ρ is in the field extension of α : $\rho = m + n\alpha$, with m and n rational numbers.*

We recall that a quadratic irrational is an irrational root of a quadratic polynomial with integer coefficients. We easily check that the Fibonacci chain verifies the conditions of the theorem. Indeed, its slope is the inverse of the golden ratio, ω , which satisfies the quadratic equation $\omega^2 = 1 - \omega$, and its intercept is $\rho = 0$.

The converse is also false: not all substitutions correspond to a canonical C&P chain. In Chap. 4 we shall study such a non-C&P substitution.

1.4.2. 2D substitutions: the example of the Ammann-Beenker tiling

In this thesis we study two 2D quasiperiodic tilings, the Penrose and Ammann-Beenker tilings. As we already mentioned, both of them can be constructed by the canonical C&P method. Alternatively, they can also be built using a substitution rule. We only discuss here the Ammann-Beenker substitution, but the principle is the same in the case of the Penrose tiling.

The substitution rule for the Ammann-Beenker tiling was already shown on Fig. (1.3b). In order to alleviate the notations, we will now operate on rhombuses and half-squares (also known as triangles) instead of working on the whole squares. The substitution rule is then recast as shown on Fig. (1.11). Notice that there are two non-equivalent ways to inflate a half-square, both of which are shown on the figure. For a given half-square inserted in a tiling patch, only one of the two possible inflations is compatible with the local arrangement of the tiles. In order to conveniently book-keep which inflation to use, arrows are drawn on the edges of the tiles. These arrows will be given a physical meaning in Chap. (4): as we shall see, they are involved in the structure of some electronic eigenstates.

In view of modeling quasicrystals, we are no so much interested in a tile model (left panel of Fig. (4.1)) as in a model of atoms linked to neighboring atoms (right panel of Fig. (4.1)). Therefore, we are interested in knowing how the substitution rule acts on the atomic positions, shown in Fig. (1.11) as dots. As presented on Fig. (1.5), we can label atomic positions with 4D vectors of integers. In the C&P formalism, these vectors are the coordinates of the 4D lattice points which are then projected to E_{\parallel} to form the tiling. One can show that the 4D vector \mathbf{v} labeling a given

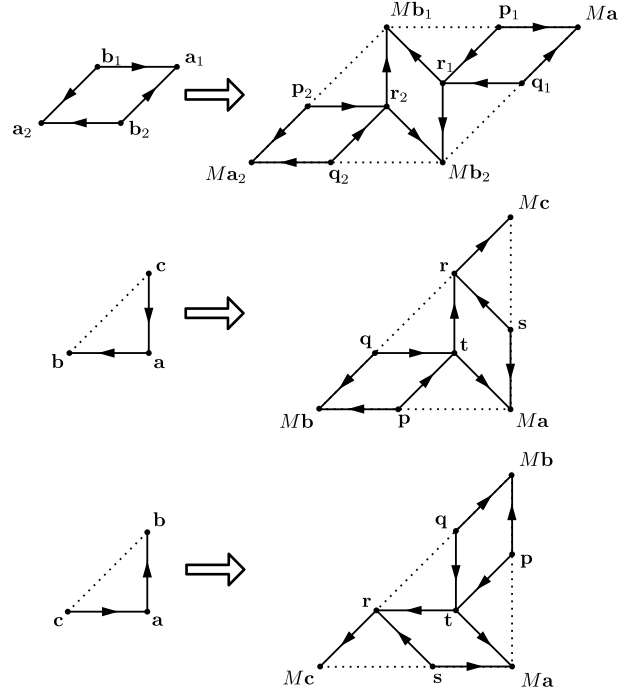


Figure 1.11. – A reformulation of the Ammann-Beenker substitution rule.

atom is transformed by substitution into the vector $M\mathbf{v}$ where M is the matrix

$$M = \begin{bmatrix} 1 & 1 & 0 & -1 \\ 1 & 1 & 1 & 0 \\ 0 & 1 & 1 & 1 \\ -1 & 0 & 1 & 1 \end{bmatrix}. \quad (1.20)$$

The substitution also create new atoms. Using the notation introduced in Fig. (1.11), the 4D vectors of the atoms created when inflating a rhombus are

$$\begin{aligned} \mathbf{p}_1 &= (M - 1)\mathbf{a}_1 + \mathbf{b}_1 \\ \mathbf{p}_2 &= (M - 1)\mathbf{a}_2 + \mathbf{b}_1 \\ \mathbf{q}_1 &= (M - 1)\mathbf{a}_1 + \mathbf{b}_2 \\ \mathbf{q}_2 &= (M - 1)\mathbf{a}_2 + \mathbf{b}_2 \\ \mathbf{r}_1 &= \mathbf{p}_1 + \mathbf{q}_1 - M\mathbf{a}_1 \\ \mathbf{r}_2 &= \mathbf{p}_2 + \mathbf{q}_2 - M\mathbf{a}_2 \end{aligned} \quad (1.21)$$

Similarly, the 4D vectors of the atoms created when inflating a half-square are

$$\begin{aligned} \mathbf{p} &= (M - 1)\mathbf{b} + \mathbf{a} \\ \mathbf{q} &= \mathbf{r} - \mathbf{c} + \mathbf{b} \\ \mathbf{r} &= (M(\mathbf{c} + \mathbf{b}) + \mathbf{c} - \mathbf{b})/2. \\ \mathbf{s} &= (M - 1)\mathbf{a} + \mathbf{c} \\ \mathbf{t} &= \mathbf{q} + \mathbf{a} - \mathbf{b} \end{aligned} \quad (1.22)$$

A python implementation of the Ammann-Beenker substitution as presented here can be found on the git repository of this thesis: https://framagit.org/Yukee/PhD_thesis/blob/master/demo/Ammann-Beenker.ipynb.

1.5. Conclusion

In this chapter, we have presented some of the numerous ways of building quasiperiodic tilings. We have also exhibited some of the geometrical of these structures: repetitivity, complexity, diffraction patterns, inflation symmetry. We are now ready to study the single electron problem on quasiperiodic structures in one and two dimensions.

Chapter 2.

Electronic properties of the Fibonacci chain solved in perturbation theory

Contents

2.1. Introduction	15
2.2. Quantum chains	16
2.2.1. Bloch’s theorem for tight-binding chains	16
2.2.2. Spectrum and eigenstates of the periodic chain	18
2.2.3. Multifractal analysis of the spectrum of the periodic chain	19
2.3. The Fibonacci chain: model and definitions	22
2.3.1. Approximants	22
2.4. Renormalization group and the multifractal nature of the Fibonacci spectrum	23
2.4.1. The perturbative renormalization group	23
2.4.2. Multifractal properties of the spectrum	25
2.5. Renormalization paths, equivalence between energy labels and com- numbers.	26
2.6. Fractal dimensions of the eigenstates to first order	29
2.7. Higher order renormalization group and multifractality	31
2.7.1. Renormalization group for the eigenstates	31
2.7.2. Local eigenstate dimensions	32
2.7.3. The spectrally averaged fractal dimensions of eigenstates	34
2.7.4. The local spectral dimensions and their average	35
2.8. Relations between fractal dimensions and dynamical exponents	36
2.8.1. A relation between fractal dimensions	36
2.8.2. Quantum diffusion and spectral fractal dimensions	37
2.8.3. An upper bound for the diffusion moments	37
2.9. Conclusion and perspectives	38

2.1. Introduction

As distinct from periodic crystals on the one hand, where electronic states are typically extended, and disordered systems on the other hand, where states are typically localized for low dimension and/or strong enough disorder, generic electronic states in quasicrystals are believed to have an intermediate “critical” character. The study of tight-binding models on the quasiperiodic Fibonacci chain, is particularly important, as a first step towards understanding the physics of these systems. These models have been extensively investigated theoretically – actually even *before* the discovery of quasicrystals! Let us mention [Kohmoto et al. \[1983\]](#), [Tang and Kohmoto \[1986\]](#), [Kohmoto et al. \[1987\]](#), [Bellissard et al. \[1989\]](#), [Damanik \[2009\]](#), [Sire and Mosseri \[1990\]](#)

and references therein. There have also been many experimental studies of electronic properties of this model. To cite some recent works, in [Verbin et al. \[2015\]](#) investigated transport due to topologically protected edge states in a Fibonacci photonic waveguide. In [Tanese et al. \[2014\]](#), the density of states of a Fibonacci tight-binding model was studied by direct observation of polariton modes in a one-dimensional cavity, and shown to have the fractal structure, log-periodic oscillations and gaps labeled as predicted by theory [Bellissard et al. \[1989\]](#).

In this chapter, we expose how *multifractal analysis* can help us understand better the structure of the spectrum and of the eigenstates of such models. We base our investigations on a renormalization group (RG) introduced independently by [Kalugin et al. \[1986\]](#) and [Niu and Nori \[1986\]](#). This RG was used in [Piéchon et al. \[1995\]](#), [Zheng \[1987\]](#) to compute the fractal dimensions of the spectrum, and in [Thiem and Schreiber \[2013\]](#) to compute the fractal dimensions of the eigenstates to first order in perturbation theory. The goal of this chapter, which is based on the article [Macé et al. \[2016\]](#) is twofold:

1. Extend the RG to describe the eigenstates at higher order in perturbation theory, thus capturing their multifractal structure – which was not captured by the first-order RG.
2. Interpret the RG construction in the higher dimensional space furnished by the C&P method.

This chapter is organized as follows. In [Sec. 2.2](#) we introduce the tight-binding model and recall its basic properties in the periodic case. In [Sec. 2.3](#) we introduce the Fibonacci chain, and in [Sec. 2.4](#) we present the perturbative RG and use it to compute the fractal dimensions of the spectrum. We compare this result to the simple case of the periodic chain. In [Sec. 2.5](#) we interpret the RG in the higher-dimensional setup of the C&P algorithm. In particular, we discuss the relevant concept of *renormalization paths*, and use it in [Sec. 2.6](#) to compute to first order the fractal dimensions of the eigenstates. We then extend the RG to higher order in [Sec. 2.7](#), and discuss the multifractal properties of the states in this context. We conclude with some conjectures about the relation between multifractal exponents in [Sec. 2.8](#).

2.2. Quantum chains

In this section we explain our framework: we study the dynamics of a single electron, and we disregard its spin (or equivalently we assume that the Hamiltonian leaves the spin invariant, and we study a given spin sector).

Many results have been derived in this framework. We expose them here.

Let $|m\rangle$ be the state localized on the m^{th} atom of the chain. We will consider in this chapter tight-binding Hamiltonians of the form

$$\hat{H} = - \sum_m t_m |m-1\rangle \langle m| + \text{H.c.} \quad (2.1)$$

This Hamiltonian describes the dynamics of a single electron that can hop, at each infinitesimal time step, from one site to its nearest neighbors. The sequence of hopping amplitudes $\dots, t_m, t_{m+1}, \dots$ can be periodic, quasiperiodic or random. How does the nature of the sequence impact the spectral and eigenstates properties of the chain? This is the question we are interested in the chapter.

2.2.1. Bloch's theorem for tight-binding chains

We consider the Hamiltonian (2.1) introduced previously. Since this Hamiltonian encodes the dynamics on a periodic chain, the series of couplings $\dots, t_m, t_{m+1}, \dots$ must be periodic. Let L be the number of atoms in a unit cell of our chain. Then, $t_{m+L} = t_m$. We wish to decouple the

intra and inter unit cell degrees of freedom. To this end, for the site m introduce the integers n and r such that

$$m = nL + r \quad (2.2)$$

with $0 \leq r \leq L - 1$. As shown on Fig. (2.1), the integer n varies from one unit cell to the next: it encodes the inter unit cell degrees of freedom. Meanwhile, the r integer varies inside a given unit cell, encoding the intra unit cell degrees of freedom.

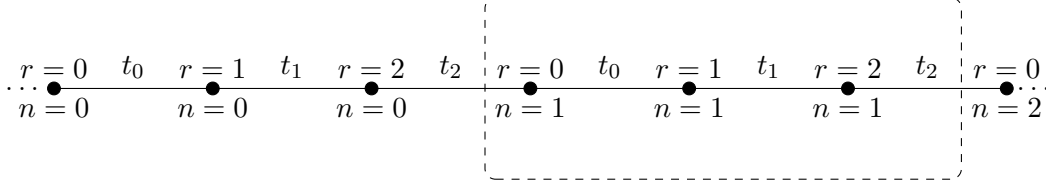


Figure 2.1. – A piece of a periodic chain of period $L = 3$ described by a Hamiltonian of type (2.8). The dashed rectangle delimits the unit cell labeled by $n = 1$.

We can write any basis vector as a tensor product of the inter and intra unit cell degrees of freedom: $|m\rangle = |n\rangle \otimes |r\rangle$, or simply $|m\rangle = |n\rangle |r\rangle$. The Hamiltonian rewrites

$$\hat{H} = - \sum_{n \in \mathbb{Z}} \left(t_0 |n-1\rangle |L-1\rangle \langle n| \langle 0| + |n\rangle \langle n| \sum_{r=1}^{L-1} t_r |r-1\rangle \langle r| + \text{H.c.} \right) \quad (2.3)$$

The only obstacle to writing the Hamiltonian as a tensor product of the inter and intra unit cell degrees of freedom is the first term appearing in the sum, that couples unit cells n and $n - 1$. In order to perform the decoupling, we go to Fourier space. We introduce $|k\rangle$, the state of wavevector k , which is related to the position basis by

$$|k\rangle = \sum_{n \in \mathbb{Z}} \frac{e^{-ikn}}{\sqrt{2\pi}} |n\rangle \quad (2.4)$$

Notice that here we defined the $|k\rangle$ state as the Fourier transform of the *inter-unit cell degrees of freedom only*. The $|k\rangle$ form an orthonormal basis of the inter-unit cell Hilbert space, since $\langle k'|k\rangle = \delta(k - k')$ and $\int_0^{2\pi} |k\rangle \langle k| dk = 1$. Using the inverse Fourier transform we can express any inter-unit cell state as a superposition of $|k\rangle$ states:

$$|m\rangle = \int_{-\pi}^{\pi} \frac{e^{ikm}}{\sqrt{2\pi}} |k\rangle dk, \quad (2.5)$$

leading us to the important result

$$\sum_n |n - n_0\rangle \langle n| = \int_{-\pi}^{\pi} e^{-ikn_0} |k\rangle \langle k| dk \quad (2.6)$$

As we can see from this last formula, passing to Fourier space, any translation invariant Hamiltonian (not necessarily restricted to nearest neighbor hoppings) will be written as a tensor product of the inter and intra unit cell degrees of freedom. In our case,

$$\hat{H} = - \int_{-\pi}^{\pi} |k\rangle \langle k| \left(t_0 e^{-ik} |L-1\rangle \langle 0| + |n\rangle \langle n| \sum_{r=1}^{L-1} t_r |r-1\rangle \langle r| + \text{H.c.} \right) dk \quad (2.7)$$

Introducing the vector of intra cell states $|\mathbf{r}\rangle = (|0\rangle, \dots, |L-1\rangle)$, we can rewrite the Hamiltonian as

$$\hat{H} = \int_{-\pi}^{\pi} |k\rangle |\mathbf{r}\rangle h(k) \langle \mathbf{r}| \langle k| dk \quad (2.8)$$

where $h(k)$ is an $L \times L$ matrix. For example, for $L = 4$, the $h(k)$ matrix writes

$$h(k) = \begin{bmatrix} 0 & -t_0 & 0 & -t_3 e^{ik} \\ -t_0 & 0 & -t_1 & 0 \\ 0 & -t_1 & 0 & -t_2 \\ -t_3 e^{-ik} & 0 & -t_2 & 0 \end{bmatrix}. \quad (2.9)$$

Any eigenstate of an Hamiltonian of a periodic chain thus writes

$$|\psi_a\rangle = |u_{a,k}\rangle |k\rangle \quad (2.10)$$

where $|u_{a,k}\rangle$ is the eigenvector number a of $h(k)$. The corresponding eigenvalue $E_a(k)$ is the energy of the eigenstate. In the position basis, the eigenstate writes

$$\psi_a(m = nL + r) = u_{a,k}(r) e^{-ikn} \quad (2.11)$$

This is one way of formulating Bloch's theorem for periodic chains¹.

Since $h(k)$ depends smoothly on k , the energies are smooth functions of k . The allowed energies thus form *bands*, separated by *energy gaps*, which may or may not be opened, depending on the parameters of the Hamiltonian. See Fig. (2.2) for a generic example.

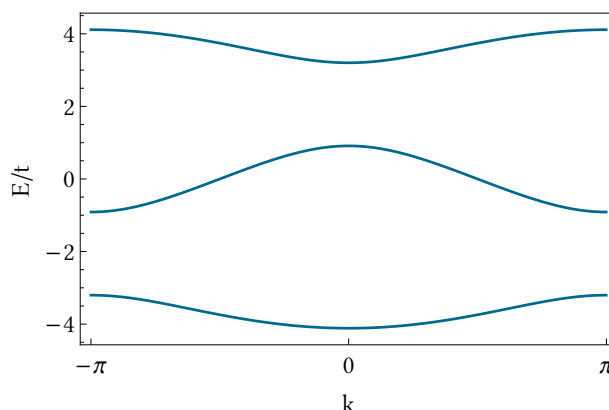


Figure 2.2. – The spectrum of the tight-binding Hamiltonian (2.8), of period $L = 3$, with $t_0 = t$, $t_1 = 2t$, $t_2 = 3t$.

2.2.2. Spectrum and eigenstates of the periodic chain

We consider here the simplest case of a chain of period 1 with no on-site potentials, and uniform hopping amplitudes:

$$\hat{H} = -t \sum_m |m+1\rangle \langle m| + \text{H.c.} \quad (2.12)$$

We start by analyzing this well known case to gain some insight on the physics of quasiperiodic chains.

1. Here the wavevector k varies in the interval $[-\pi, \pi)$, while according to the most usual convention it varies in $[-\pi/L, \pi/L)$ for a chain of period L , since usually one writes $\psi_a = u_{a,k}(r) e^{-iknL}$.

Standard unit cell

Since the chain has period 1, there is 1 atom by unit cell and the h matrix introduced in Eq. (2.8) is just equal to the energy at wavevector k :

$$h(k) = E(k) = -2t \cos(k). \quad (2.13)$$

L atoms unit cell

Following Sire and Mosseri [1990], in order to compare more easily with the quasiperiodic case, we take as a unit cell a chain of L consecutive atoms.

The h matrix is now $L \times L$, and writes

$$h_L(k) = \begin{bmatrix} 0 & -t & 0 & \dots & 0 & -te^{ik} \\ -t & \ddots & -t & & & 0 \\ 0 & \ddots & \ddots & \ddots & & \vdots \\ \vdots & & \ddots & \ddots & \ddots & 0 \\ 0 & & & \ddots & \ddots & -t \\ -te^{-ik} & 0 & \dots & 0 & -t & 0 \end{bmatrix} \quad (2.14)$$

One finds that the L energy states are indexed by an integer $a \in [0, L)$, and can be written (see Sire and Mosseri [1990]):

$$E_a(k) = -2t \cos\left(\frac{2a\pi - k}{L}\right). \quad (2.15)$$

In particular the bandwidth of the band number a is

$$\Delta_a = |E_a(\pi) - E_a(0)| \quad (2.16)$$

In the following, we will be particularly interested in the large unit cell limit $L \rightarrow \infty$, in which the bandwidth becomes

$$\Delta_a \underset{L \rightarrow \infty}{\sim} \frac{\pi}{L} \left| \sin\left(\frac{2a\pi}{L} + \frac{\pi}{2L}\right) \right|. \quad (2.17)$$

The a^{th} eigenstate of $h_L(k)$ is

$$u_{a,k}(m) = \mathcal{N}_a \exp\left(\pm i \frac{2a\pi - k}{L} m\right) \quad (2.18)$$

where \mathcal{N}_a is a normalization coefficient. Denoting by n the inter-unit cell index, the eigenstate of the full Hamiltonian writes $u_{a,k}(m)e^{-ikn}$, according to (2.11).

2.2.3. Multifractal analysis of the spectrum of the periodic chain

As discussed in Appx. A, multifractal analysis is a tool for characterizing scale-invariant objects. The spectrum of the periodic chain is (almost) trivially scale-invariant, and is not particularly exciting. However, we will apply multifractal analysis to this simple spectrum, in order to gain some intuition, useful when focusing on the more involved case of the Fibonacci chain spectrum.

We introduce the *density of states* (or DOS) ρ defined as

$$\rho(E)dE = \text{fraction of states in the interval } [E, E + dE) \quad (2.19)$$

We shall also note $\rho([E_1, E_2])$ the fraction of states in the interval $[E_1, E_2)$:

$$\rho([E_1, E_2]) = \int_{E_1}^{E_2} \rho(E)dE. \quad (2.20)$$

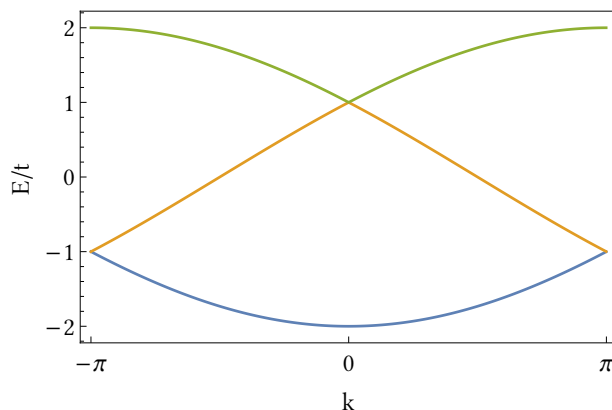


Figure 2.3. – The $L = 3$ energy bands of the periodic chain of period 1 with the period artificially tripled.

In the context of multifractal analysis, we interpret the DOS as a mass distribution, of which we want to analyze the scaling. As explained in Appx. A, we can do so by partitioning the interval in which the DOS lies into a set of interval (or boxes). We recall that the partition function writes

$$\Gamma(q, \tau) = \sum_E \frac{\rho([E, E + \Delta E])^q}{(\Delta E)^\tau} \quad (2.21)$$

We now have to choose how we actually partition the support of the DOS into a set of boxes. Choosing as a unit cell a chain of L consecutive atoms, one obtains, as shown on Fig. (2.3), L energy bands, which naturally partition the energy axis in L non-overlapping intervals. This partitioning naturally extends to quasiperiodic chains, as we will see, and as discussed for example in Rüdinger and Sire [1996]. Each band contains a fraction $1/L$ of the states. Thus, the previous partition function writes

$$\Gamma(q, \tau) = \left(\frac{1}{L}\right)^q \sum_{a=0}^{L-1} \frac{1}{(\Delta_a)^\tau} \quad (2.22)$$

where a indexes the L energy bands. We are interested in the limit where the partitioning is finer and finer, that is the limit where the number of bands L goes to infinity. The bandwidth (2.17) converges in this limit to a periodic function of a/L . We exploit this fact to transform the sum in an integral. Letting $u = 2(a + 1/4)/L$,

$$\Gamma(q, \tau) \underset{L \rightarrow \infty}{\sim} \frac{L^{\tau+1}}{L^q} \frac{1}{\pi^\tau} \underbrace{\int_{1/(2L)}^{1-3/(2L)} \frac{du}{|\sin(\pi u)|^\tau}}_{=I(\tau)} \quad (2.23)$$

When $u = 1/(2L) \rightarrow 0$, the integrated function behaves as $1/u^\tau$. Thus if $\tau < 1$, $I(\tau)$ converges in the $L \rightarrow \infty$ limit. We call $I_\infty(\tau)$ its limit. Thus,

$$\Gamma(\tau < 1) \underset{L \rightarrow \infty}{\sim} \frac{L^{\tau+1}}{L^q} \frac{I_\infty(\tau)}{\pi^\tau} \quad (2.24)$$

We deduce that

$$q(\tau < 1) = 1 + \tau \quad (2.25)$$

In this “trivial” case, the fractal dimensions are equal to 1. On the other hand, if $\tau > 1$, the integral diverges. The divergences come the boundaries of the integral, where the integrated

function behaves as $1/u^\tau$, implying that

$$I(\tau > 1) \underset{L \rightarrow \infty}{\sim} \text{cst}(\tau) \times L^{\tau-1} \quad (2.26)$$

We conclude that

$$q(\tau > 1) = 2\tau \quad (2.27)$$

Inverting relations (2.25) and (2.27), and recalling that the fractal dimensions verify $d_q = \tau_q/(q-1)$ (see Appendix A.2.3), we obtain

$$d_q = \begin{cases} 1 & \text{if } q \leq 2 \\ \frac{q}{2(q-1)} & \text{if } q \geq 2. \end{cases} \quad (2.28)$$

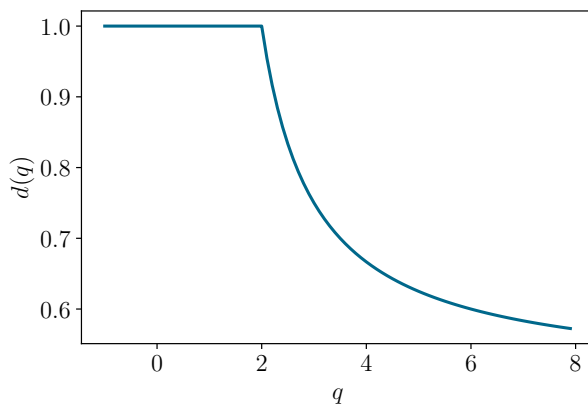


Figure 2.4. – The fractal dimensions of the periodic chain.

Fig. (2.4) shows the fractal dimensions as a function of q . The box-counting dimension d_0 equals 1, so the spectrum of the periodic chain is not a fractal, as we intuitively expected. However, we may be surprised by the fact that the fractal dimensions become non-trivial when $q \geq 2$: $0 < d_{q \geq 2} < 1$.

To understand better this behavior, let us compute the multifractal spectrum. Computing it from the fractal dimensions is straightforward, as explained in Sec. A.2.3. In the case of the spectrum of the periodic chain, the multifractal spectrum consists of the two points $\alpha = 1$, $f(1) = 1$ and $\alpha = 1/2$, $f(1/2) = 0$. The point $(1, 1)$ is the “unsurprising” point one would also have obtained when performing multifractal analysis of a line of uniform density. The point $(1/2, 0)$ is more interesting: it is the point making fractal dimensions for $q \geq 2$ non-trivial. Since $f(\alpha)$ is the fractal dimension (or box-counting dimension) of the set of points whose scaling is α , the fact that $f(1/2) = 0$ means that the points whose scaling is non-trivial form a set of dimension 0, that is, a set of isolated points. Where are these isolated points? It is easy to spot them since – owing to their non-trivial scaling – they correspond to singularities of the DOS.

As seen on Fig. (2.5), the DOS has two singularities at the edges of the spectrum: $E = \pm 2t$. Around these points the DOS diverges as the inverse of a square root: $\rho(E) \underset{E \rightarrow \pm 2t}{\sim} \text{cst} \times |2t \mp E|^{-1/2}$, which implies that the fraction of state scales as $|2t \mp E|^{1/2}$, meaning that the Hölder exponent (defined in Sec. A.2.2) at these two points is indeed $\alpha = 1/2$.

As we have seen in this simple example, the multifractal analysis can be viewed as a way to detect singularities in the DOS and to classify them according to their scaling.

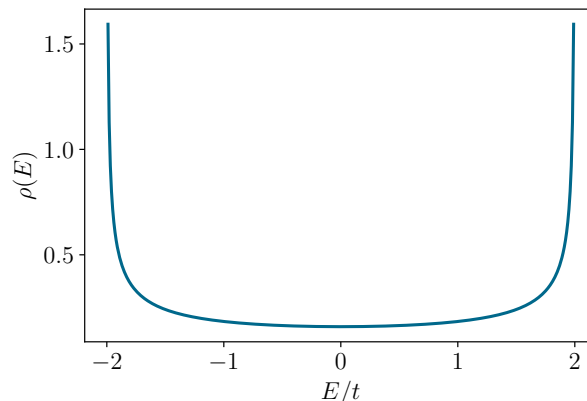


Figure 2.5. – The DOS of the periodic chain.

2.3. The Fibonacci chain: model and definitions

We now turn back to the more general model of (2.1):

$$\hat{H} = - \sum_m t_m |m-1\rangle \langle m| + \text{H.c.} \quad (2.29)$$

In the periodic case we considered in the previous section, the hopping amplitudes were uniform and set to $t_m = t$. We now consider the case where the hopping amplitude t_m is non-uniform and can take the value t_A or t_B .

To any sequence of letters A and B corresponds a sequence of hopping amplitudes. In the remaining of this chapter, we consider the specific case of the *Fibonacci sequence*, already introduced in the previous chapter (see Fig. (1.6)). t_m varies along the chain according to the rule

$$t_m = \begin{cases} t_A & \text{if } S_\omega(m) = 1, \\ t_B & \text{if } S_\omega(m) = 0. \end{cases} \quad (2.30)$$

where $S_\omega(m)$ is the *Sturm function* defined as $S_\omega(m) = \lfloor \omega(m+1) \rfloor - \lfloor \omega m \rfloor$. See Appx. B for a proof of equation (2.30) and more details about Sturmian sequences of letters. Also note that the point $m = 0$ is the point where the slope intercepts a lattice point in the C&P construction of Fig. (1.6).

The Fibonacci chain can alternatively be constructed recursively by the *substitution method*, as explained in Sec. 1.4. We recall that starting with the finite chain $C_0 = B$, to which we apply the substitution rule

$$S : \begin{cases} A \rightarrow AB \\ B \rightarrow A \end{cases} \quad (2.31)$$

we obtain a series of longer and longer chains : $C_1 = S(C_0) = B$, $C_2 = S(C_1) = AB$, \dots $C_l = S^l(C_0)$. The semi-infinite chain C_∞ coincides with the chain obtained by C&P (see Sec. 1.4), and we will also refer to this chain as the Fibonacci chain.

2.3.1. Approximants

In numerical calculations, we will replace the Fibonacci chain C_∞ by a periodic system, whose elementary cell is the finite chain C_l (the so-called l^{th} periodic approximant). In the C&P formalism, and in formula (2.30), this amounts to replacing the irrational slope ω by a rational approximation, $\omega_l = F_{l-2}/F_{l-1}$, where F_l is the l^{th} Fibonacci number (defined as $F_{l+1} = F_l + F_{l-1}$), starting from $F_1 = F_2 = 1$).

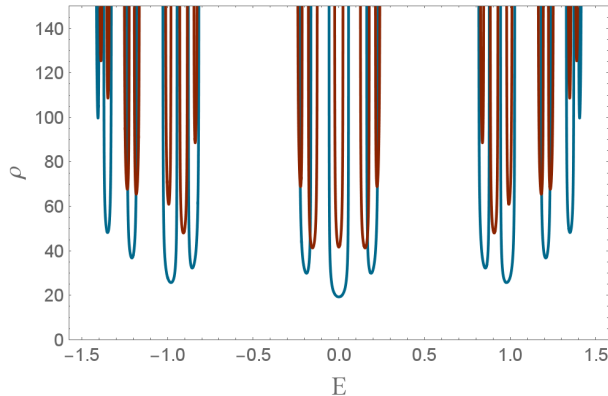


Figure 2.6. – The numerically computed DOS of the approximants $l = 7$ (blue) and $l = 8$ (red), with $t_A = 0.5$, $t_B = 1$.

Fig. (2.6) shows the DOS of two consecutive Fibonacci approximants. As can be seen, the l^{th} approximant has F_l mini-bands, each coming with a pair of Van Hove singularities. When the number of the approximant, l , is increased, the DOS fluctuates on smaller and smaller energy scales, converging in the $l \rightarrow \infty$ – or quasiperiodic – limit to the DOS of the Fibonacci chain. The number of singularities of the DOS diverges in the quasiperiodic limit. This is in contrast with the periodic case, where there were only two singularities, at the edges of the energy spectrum (see Sec. 2.2.3). Multifractal analysis is an essential tool for understanding the properties of such a highly singular spectrum.

2.4. Renormalization group and the multifractal nature of the Fibonacci spectrum

In this section, we describe a perturbative renormalization group introduced independently by Kalugin et al. [1986] and Niu and Nori [1986], and, following Zheng [1987], Piéchon et al. [1995], use it to compute the multifractal spectrum of the Fibonacci chain.

2.4.1. The perturbative renormalization group

Atoms and molecules.

Up to a global rescaling of the energies, the Hamiltonian depends on the single parameter $\rho = t_A/t_B$, with $\rho \ll 1$ in the strong modulation limit. In this chapter, we focus on this limit. The weak modulation limit $\rho \sim 1$ was also studied by Sire and Mosseri [1990], while Barache and Luck [1994] studied a related model in another limit.

In the strongly modulated limit, one has a natural classification of sites into “molecule-”type (m) and “atom-”type sites (a) depending on their local environment. Atom-type sites have weak bonds on the left and on the right, so they are weakly coupled to the rest of the chain. Molecule-sites are linked by a strong bond to another molecule-site, and have a weak bond on either side. In the limit $t_A \rightarrow 0$, these pairs form isolated diatomic molecules, while the remaining sites correspond to isolated atoms.

When $\rho = 0$, the atoms and the molecules decouple. The spectrum consists of three degenerate levels: $E = \pm t_B$, corresponding to molecular bonding and antibonding states, and $E = 0$, for the isolated atomic state. When $\rho \neq 0$, the states in each of the three degenerate levels weakly couples to each other, thus lifting the degeneracy. We now consider separately the case of the atomic and of the molecular energy levels.

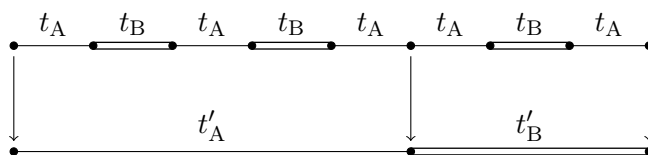
Atomic levels


Figure 2.7. – Illustration of the atomic deflation rule: here the fifth approximant is mapped to the second.

At first order, each atomic state, localized on an atomic site, couples to the atomic states localized on the two neighboring atoms (Fig. (2.7)). Two neighboring atomic sites can be separated either by a *weak-strong-weak* sequence of couplings (as happens for the two rightmost atomic sites of Fig. (2.7)), or by a *weak-strong-weak-strong-weak* sequence of couplings (as happens for the two leftmost atomic sites of Fig. (2.7)). In perturbation theory, the effective jump amplitude coupling two neighboring atoms thus takes two possible values, a strong and a weak one. The effective jump amplitudes can be computed using Brillouin-Wigner perturbation theory (Appendix D), as done in Niu and Nori [1986], Kalugin et al. [1986]. To first order, the effective couplings turn out to be linked to the old ones by a multiplicative factor \bar{z} : $t'_B = \bar{z}t_B$, $t'_A = \bar{z}t_A$, with $\bar{z} = \rho^2$. We call *atomic deflation* the replacement of the initial couplings by the effective ones.

Crucially, after atomic deflation, the sequence of renormalized couplings is again arranged according to the Fibonacci sequence. More precisely, the atomic deflation maps the chain C_l to the chain C_{l-3} . Indeed, iterating the Fibonacci substitution rule (2.31) three times one obtains

$$S^3 : \begin{cases} A \rightarrow ABAAB \\ B \rightarrow ABA \end{cases} \quad (2.32)$$

Thus, up to a circular permutation, the Fibonacci rule iterated three times precisely maps a weak coupling to the sequence weak-strong-weak-strong-weak and a strong coupling to weak-strong-weak. Since this transformation maps the chain C_l to the chain C_{l+3} , the inverse transformation – which is the atomic deflation, indeed maps C_l to C_{l-3} as announced.

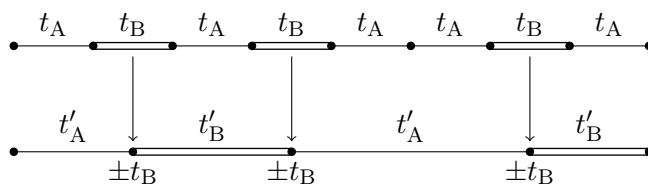
Molecular levels.


Figure 2.8. – Illustration of the molecular deflation rule: the fifth approximant is mapped to the third.

In a similar fashion, each state localized on a diatomic molecule, is coupled to the neighboring molecules through only two possible effective couplings between two neighboring molecules. Upon replacement of the couplings between molecules by renormalized couplings, one passes from the chain C_l to the chain C_{l-2} (see figure (2.8) for an example). We call this geometrical transformation the *molecular deflation*. The renormalized couplings are linked to the old ones by a multiplicative factor z . One finds $t''_B = zt_B$, $t''_A = zt_A$, with $z = \rho/2$. In addition, the molecular renormalization introduces on-site potentials $\pm t_A$ on the deflated chain, shifting the whole energy spectrum by $+t_B$ (bonding molecular levels), or $-t_B$ (antibonding molecular levels).

To summarize, the Hamiltonian of the l^{th} approximant decouples into the direct sum of three Hamiltonians:

$$\hat{H}_l = \underbrace{\left(z\hat{H}_{l-2} - t_B\right)}_{\text{bonding levels}} \oplus \underbrace{\left(\bar{z}\hat{H}_{l-3}\right)}_{\text{atomic levels}} \oplus \underbrace{\left(z\hat{H}_{l-2} + t_B\right)}_{\text{antibonding levels}} + \mathcal{O}(\rho^4) \quad (2.33)$$

In the limit $l \rightarrow \infty$, the chain becomes quasiperiodic and its eigenstates and its spectrum are nontrivial: they exhibit multifractality [Kohmoto et al. \[1983\]](#), [Tang and Kohmoto \[1986\]](#), [Kohmoto et al. \[1987\]](#), [Zheng \[1987\]](#). Finally, remark that swapping the role of the A and B letters changes ρ to $1/\rho$. Therefore, the limit $\rho \gg 1$ can also be described by the same RG, as explained in [Niu and Nori \[1990\]](#).

2.4.2. Multifractal properties of the spectrum

Just like in the periodic case 2.2.3, following [Piéchon et al. \[1995\]](#), [Zheng \[1987\]](#), we use the thermodynamic formalism to compute the fractal dimensions. The partition function of the l^{th} approximant writes:

$$\Gamma_l(q, \tau; t_A, t_B) = \left(\frac{1}{F_l}\right)^q \sum_{a=0}^{F_l-1} \frac{1}{(\Delta_a)^\tau}, \quad (2.34)$$

where we have employed the same notation as in the periodic case: a indexes the F_l energy bands and Δ_a is the width of the band of index a .

Using the perturbative RG introduced in the previous section, we relate via Eq. (2.33) the spectrum of the l^{th} approximant to the spectra of the approximants $l-2$ (via molecular deflation) and $l-3$ (via atomic deflation). Each of the 2 molecular spectra contain a fraction F_{l-2}/F_l of the energy bands, while the atomic spectrum contains the remaining F_{l-3}/F_l fraction of the energy bands. So,

$$\Gamma_l(q, \tau; t_A, t_B) = 2 \left(\frac{F_{l-2}}{F_l}\right)^q \Gamma_{l-2}(q, \tau; t'_A, t'_B) + \left(\frac{F_{l-3}}{F_l}\right)^q \Gamma_{l-3}(q, \tau; t'_A, t'_B) \quad (2.35)$$

After an atomic deflation, the couplings are renormalized: as seen in the previous section, $t'_{A/B} = \bar{z}t_{A/B}$ with $\bar{z} = \rho^2$. Similarly, after a molecular deflation, $t''_{A/B} = zt_{A/B}$ with $z = \rho/2$. We thus obtain

$$\Gamma_l(q, \tau; t_A, t_B) = 2 \left(\frac{F_{l-2}}{F_l}\right)^q z^{-\tau} \Gamma_{l-2}(q, \tau; t_A, t_B) + \left(\frac{F_{l-3}}{F_l}\right)^q \bar{z}^{-\tau} \Gamma_{l-3}(q, \tau; t_A, t_B) \quad (2.36)$$

In the quasiperiodic limit, $F_{l-2}/F_l \sim \omega^2$ and $F_{l-3}/F_l \sim \omega^3$ where ω is the inverse of the golden ratio. The fractal dimensions $d(q)$ are related to τ by $\tau(q) = (q-1)d(q)$, with $\tau(q)$ the value of τ making the partition function converge in the quasiperiodic limit (see Appx. A.2.3). The fractal dimensions $d(q)$ of the spectrum of the Fibonacci chain are thus given, in the strong quasiperiodicity limit, by

$$\boxed{1 = 2\omega^{2q} z^{-(q-1)d(q)} + \omega^{3q} \bar{z}^{-(q-1)d(q)}} \quad (2.37)$$

Up to now, we have strictly followed the reasoning exposed in [Zheng \[1987\]](#), [Piéchon et al. \[1995\]](#). We can in fact go a bit beyond what is exposed in the aforementioned article, and solve explicitly the equation, obtaining

$$d(q) = \frac{1}{1-q} \frac{\log \left[\omega^{-q} (\sqrt{1 + \omega^{-q}} - 1) \right]}{\log \rho} + \mathcal{O} \left(\frac{1}{(\log \rho)^2} \right) \quad (2.38)$$

In particular, we find for the box-counting dimension

$$d(0) = \frac{\log(\sqrt{2} - 1)}{\log \rho} + \mathcal{O}\left(\frac{1}{(\log \rho)^2}\right) \quad (2.39)$$

in agreement with the result of [Damanik and Gorodetski \[2011\]](#), obtained using a trace-map.

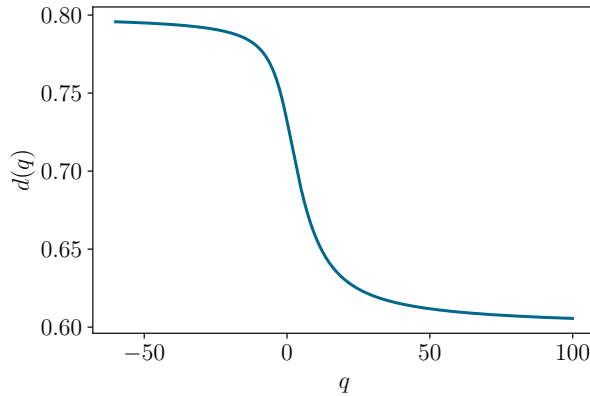


Figure 2.9. – The fractal dimensions of the Fibonacci chain, computed in the strong quasiperiodicity limit (2.38). The coupling was set to $\rho = 0.3$.

Notice that formula (2.38) is valid only in the strong quasiperiodicity limit. In that regime – as one can easily check numerically – the fractal dimensions given by (2.38) verify $0 < d(q) < 1$, as shown on Fig. (2.9). Thus, *the spectrum of the Fibonacci chain is multifractal, at least in the strong quasiperiodicity limit*. Furthermore, since $0 < d(q) < 1$ for all values of q , *the spectrum has no regular components*: the DOS is singular at every energy in the spectrum. One also says that the spectrum is *singular continuous*.

This contrasts with the situation for the periodic chain, whose fractal dimensions are non-trivial only for $q \geq 2$ (see Eq. (2.28)), a signature that the DOS is regular, except at some points, which in that case are the two Van Hove singularities at the edges of the spectrum.

Although the reasoning exposed here only holds in the strong quasiperiodicity limit, *the conclusions obtained concerning the multifractal nature of the spectrum hold for every non-trivial coupling: $\rho \neq 0, 1, \infty$* . See [Sütő \[1989\]](#) and [Damanik \[2009\]](#) for a review. Finally, let us mention [Sire and Mosseri \[1989\]](#) which explicitly computes the fractal dimensions in the *periodic limit* $\rho \sim 1$.

2.5. Renormalization paths, equivalence between energy labels and combers.

Renormalization paths of the energy bands.

Eq. (2.33) tells us that the spectrum of the Hamiltonian \hat{H}_l is the union of three energy clusters – the antibonding molecular cluster, the atomic cluster and the bonding molecular cluster – each of which is a scaled version of the spectrum of a smaller approximant. Molecular clusters are separated from the atomic cluster by a gap of width $\Delta \sim t_B(1 - z)$. Each of these main clusters can be decomposed into three sub-clusters, and so on. The spectrum has therefore a recursive, Cantor set-like description, as shown by Fig. (2.10).

One can assign to the energy bands belonging to the bonding, atomic or antibonding clusters respectively the labels $+$, 0 or $-$. To this, one can append another $+$, 0 or $-$ according to the

2.5. Renormalization paths, equivalence between energy labels and conumbers.

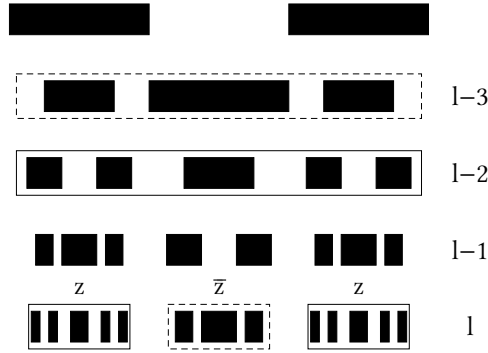


Figure 2.10. – Spectrum of the approximant H_l ($l = 8$) constructed geometrically from the spectra of H_{l-2} and H_{l-3} (relation (2.33)). z and \bar{z} are the two scaling factors.

sub-cluster type of each energy. Repeating this procedure recursively, one obtains for each energy band a unique sequence of letters called its *renormalization path* Piéchon et al. [1995], Kohmoto et al. [1987]. Figure (2.11) shows the renormalization paths of two particular energy bands. Let us note that although the renormalization path labeling of the energy bands has been derived in the perturbative limit, it continues to hold for $0 < \rho < 1$ since no gap closes.

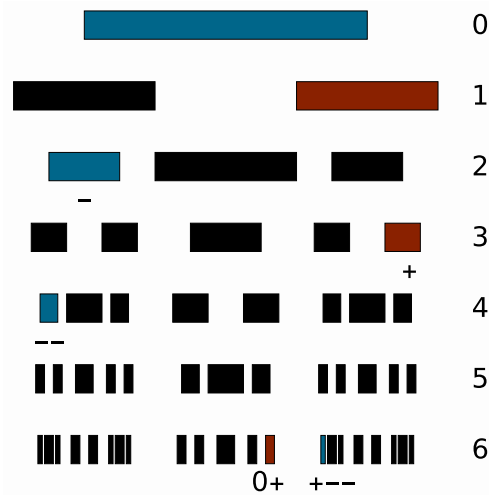


Figure 2.11. – Every energy band can be labeled by its renormalization path. As an example, here are shown the renormalization paths of the energy bands labeled by $0+$ (red) and $+--$ (blue).

Renormalization paths of the sites.

One assigns to every atomic (resp molecular) site of the chain C_l a label “a” (resp “m”). Because the set of atoms and the set of molecules of C_l are mapped to the chains C_{l-3} and C_{l-2} respectively, one can repeat the labeling procedure recursively. Thus, to each site is associated a sequence of letters, that we call the *renormalization path* of the site. Note that because we have not distinguished between bonding and antibonding states on molecules, several molecular states can have the same renormalization path.

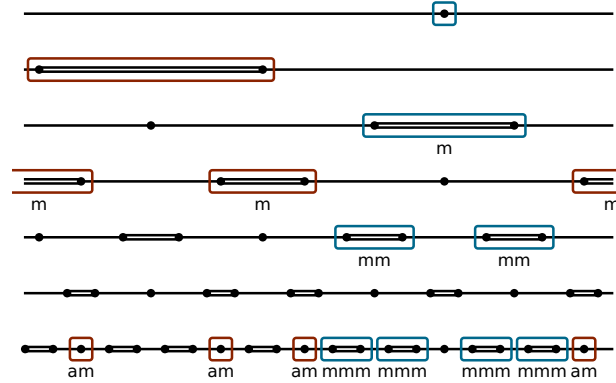


Figure 2.12. – Every site can be labelled by its renormalization path, as shown here for the sites of non-zero amplitude, at first order, of the eigenstates labelled by $0+$ (red) and $+ - -$ (blue).

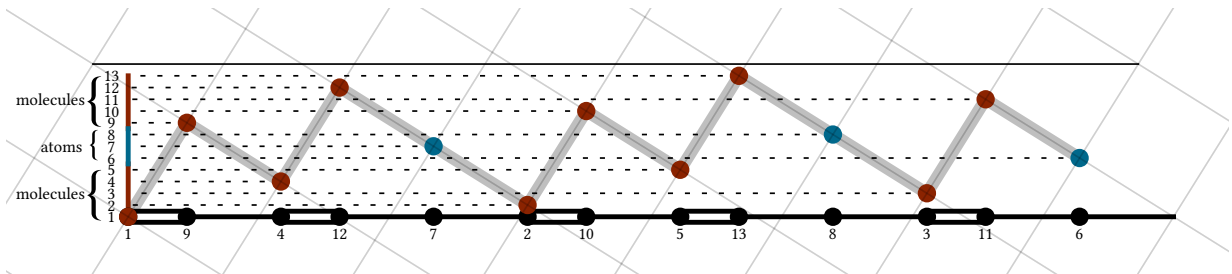


Figure 2.13. – Example of the cut and project method showing sites along the horizontal physical axis, and their conumber along the perpendicular space (vertical) axis. Conumbering naturally orders sites according to their local environment: atomic sites (in blue) are clustered around the center of the windows, while molecular sites (in red) are grouped at the sides.

Symmetry between renormalization paths for sites and energies.

In the perturbative limit, because of (2.33), an eigenstate associated to an atomic/molecular energy band has nonzero amplitude only on atomic/molecular sites. This is again true at every step of the renormalization process, so that by recursion, a given eigenstate has nonzero amplitude at first order only on sites whose renormalization path matches the one of the energy level associated energy band (provided that we make the identification $\pm \leftrightarrow m$ and $0 \leftrightarrow a$).

In order to further understand the symmetry between the renormalization paths for sites and energies, we now make use of the C&P method. Let us recall very briefly (see 1.2.2 for more details) that the cut and project method considers the sites on the chain C_l as projections along an axis E_{\parallel} of selected sites on a square lattice (see Fig. (2.13)). We can also consider the projection of the selected sites along the E_{\perp} axis, orthogonal to E_{\parallel} . The projection of the sites on E_{\perp} forms a regular lattice whose density increases with the approximant size. In E_{\perp} , as seen on Fig. (2.13), the sites regroup in 3 clusters : a central atomic cluster surrounded by two molecular clusters. Keeping only sites belonging to the atomic/molecular clusters exactly amounts to performing an atomic/molecular decimation. Since the deflated chains are again Fibonacci chains, the 3 clusters are made of 3 molecular-atomic-molecular subclusters, and so on. Thus, in E_{\perp} the sites are ordered exactly in the same way as the energy bands. This hints that looking at the sites in E_{\perp} is of interest. We therefore choose to label the sites according to their projection on E_{\perp} (from

bottom to top on fig. (2.13)). Let us call m the index of each site according to the order in which it appears in real space. Then, for the 1th approximant, the conumbers (or perpendicular space labels) c are given by

$$c(m) = F_{l-1}m \pmod{F_l}. \quad (2.40)$$

This relabeling of the sites was first introduced by Mosseri [1988], and was called *conumbering*. For more details on conumbering, see Appx. B. Because of the symmetry between the ordering of the sites in E_\perp and the ordering of the energy bands, the conumber labels play the same role as the energy labels. This symmetry will prove itself useful in our analysis of the eigenstates.

As an illustration of the relevance of conumbering, we show the local density of states as a function of the energy labels and the conumber labels. This plot is invariant under the exchange of the position/energy axes, in the strong quasiperiodicity limit (figure (2.14)), for the reason explained previously. Crucially, this symmetry is revealed only if one uses conumbering for the sites, and remains hidden otherwise.

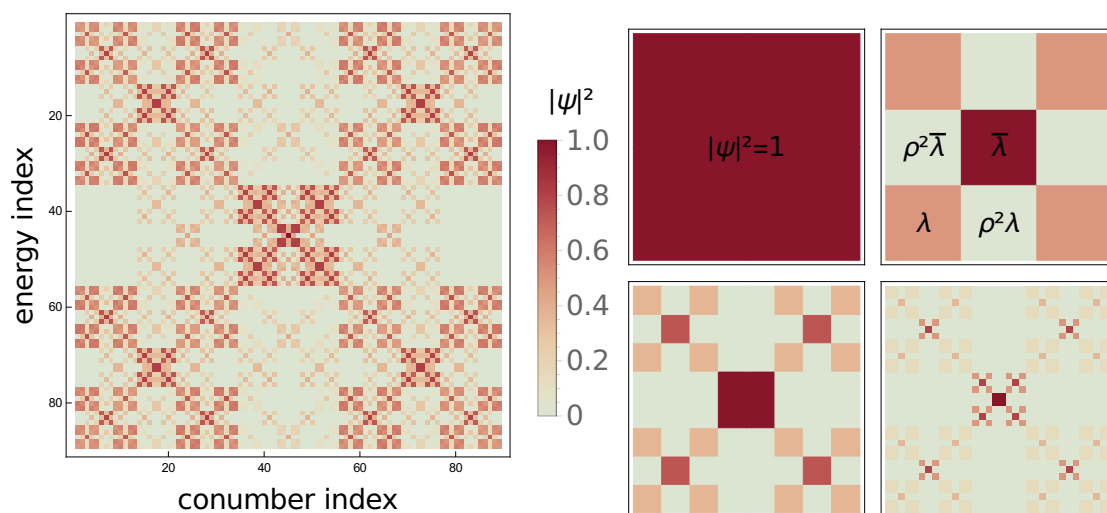


Figure 2.14. – Upper figure: intensity plot of the numerically computed LDoS. x-axis: conumber index, y-axis: energy index. Color represents the presence probability (i.e. the LDoS). Lower figure: the first few steps of the geometrical construction of the LDoS according to our perturbation theory.

2.6. Fractal dimensions of the eigenstates to first order

From Fig. (2.14), it is clear that the probability to find the electron of energy E on the site of conumber c , $|\psi_c(E)|^2$, forms a 2D fractal. The purpose of this section is to compute the associated fractal dimensions.

Because of the symmetry – shown in the previous section – between the energy and conumber indices, computing the fractal dimensions of the 2D object $(c, E) \rightarrow |\psi_c(E)|^2$ is equivalent to computing the fractal dimensions of the 1D object $c \rightarrow |\psi_c(E)|^2$, which is simply the presence probability distribution in conumber (or perpendicular) space E_\perp , at energy E .

It may seem questionable to compute the fractal dimension of an eigenstate in perpendicular space: after all, this space has no direct physical meaning! Let us however prove that it makes no difference: *a given eigenstate form in parallel and perpendicular spaces two objects whose fractal dimensions coincide.*

Let us begin by computing the fractal dimensions of an eigenstate in physical space E_\parallel . In the following, we keep the total length of the system fixed, to some arbitrary value, say 1. Then,

the inter-site distance for the l^{th} approximant is $1/F_l$. Therefore, the mass at scale $\epsilon = 1/F_l$ (see Appendix A for a definition) can be approximated by

$$M_q^{(l)}(E) = \sum_m |\psi_m^{(l)}(E)|^{2q} \quad (2.41)$$

where $\psi^{(l)}(E)$ is the eigenstate of energy E on the l^{th} approximant. The fractal dimensions are then given by the scaling of the mass (see Appendix A) as the size of the approximant is increased:

$$d_q^\psi(E) = \frac{-1}{q-1} \lim_{l \rightarrow \infty} \frac{\log M_q^{(l)}(E)}{\log F_l} \quad (2.42)$$

Now, since conumbering is a permutation of the indices, the q -mass we just introduced coincides with the q -mass in perpendicular space. We conclude that the fractal dimensions of eigenstate in real space and in perpendicular space coincide, as announced. This obviously holds for any C&P tiling.

Let us now compute the fractal dimensions. As recalled in Appendix A, a value $0 < d_q^\psi(E) < 1$ indicates a fractal object. More precisely, in the context of eigenstates, $d_q^\psi = 1$ indicates that an extended state, while $d_q^\psi = 0$ characterizes a localized state. States whose fractal dimensions have intermediate values are called *critical*. Their multifractal properties can be probed by varying q .

At leading order in ρ the renormalization of the eigenstates is simple, and well understood, see Piéchon [1996]. For a eigenstate in the atomic cluster, we have $|\psi_m^{(l)}(E)| = |\psi_{m'}^{l-3}(E')|$. For a eigenstate in the molecular cluster, $|\psi_m^{(l)}(E)| = |\psi_{m'}^{l-2}(E')|/\sqrt{2}$. E and E' are the energies on the original chain and on the deflated one respectively. Therefore, we obtain immediately the leading order fractal dimensions of the eigenstate associated to the energy E :

$$\boxed{d_{q,0}^\psi(E) = x(E) \frac{\log 2}{\log \omega^{-1}} + \mathcal{O}(\rho^2)}, \quad (2.43)$$

where

$$x(E) = \lim_{l \rightarrow \infty} \frac{n_m(E)}{n} \quad (2.44)$$

with $n_m(E)$ the number of $+/-$ letters in the renormalization path of E , i.e. $x(E)$ is the fraction of RG steps spent in molecular clusters. x is a non trivial function of the energy (figure (2.15)), whose structure is reminiscent of the one of the local density of states (2.14). In the quasiperiodic limit, x varies continuously between 0 and $1/2$, and $d_{q,0}^\psi(E)$ is a continuous function of x . The distribution of x is given by

$$\Omega(x(n_0, n_m)) = 2^{n_m} \frac{(n_0 + n_m)!}{n_0! n_m!} \quad (2.45)$$

Where $\Omega(x)$ is the number occurrences of a given value of x . It coincides with the distribution of the widths of the energy bands Piéchon et al. [1995]. Therefore, in the quasiperiodic limit, the distribution of x is given by f , the Legendre transform of the fractal dimensions of the spectrum: $P(x) \sim F_l^{f(x)-1}$. This distribution is sharply peaked around the most probable value, $x_{mp} = 2(3\omega - 1)/5 \simeq 0.3416\dots$. States with this value of x are statistically the most significant.

Since the fractal dimensions only depend on x , we perform the change of variables $d_{q,0}^\psi(E) \rightarrow d_{q,0}^\psi(x)$. Since $0 \leq x \leq 1/2$, we have $0 < d_q^\psi(x) < 1$: the eigenstates are critical, as we expect for a quasiperiodic system.

The parameter x determines completely the fractal properties of the eigenstates². For example, $x_a = 0$ for the level in the center having the renormalization path $00\dots$ (cf figure (2.15)). The

2. But it doesn't completely specify a site (or a state).

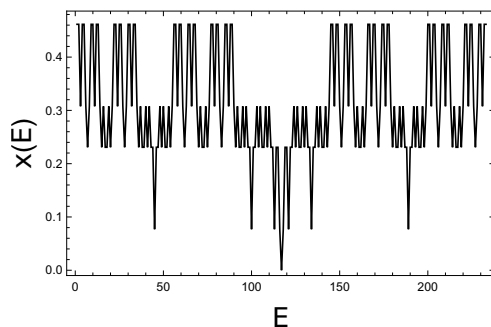


Figure 2.15. – The parameter x as a function of the energy labels (or equivalently of the sites in conumbering), for the approximant of 233 sites. Lines are drawn to guide the eye.

corresponding eigenstate has a zero fractal dimension, and is thus completely localized. On the other hand, the maximal value of $x = \frac{1}{2}$ is reached for the levels $E = E_{\min}, E_{\max} = \pm t_B/(1 - z)$ at the edges of the spectrum, for which the renormalization paths are $++ \dots$ and $-- \dots$. The corresponding eigenstates are the most extended. They occupy a fraction $(1/F_l)^{-\frac{\log 2}{2 \log \omega}}$ of the sites.

To conclude, we note that, to leading order in ρ , the fractal dimensions of the eigenstate do not depend on q . Thus *the eigenstates are monofractals* – not multifractals – at this order in ρ and multifractality appears only at the next-to-leading order, as discussed in the next section. This first-order description of the eigenstates has been compared to numerical results by [Thiem and Schreiber \[2013\]](#), where the agreement was found not to be very good. We argue that this is because the eigenstates becomes rapidly multifractal as ρ is increased. Fortunately it is possible to calculate higher order corrections, and thereby vastly improve our theoretical predictions concerning the eigenstates, as shown below.

2.7. Higher order renormalization group and multifractality

At higher order the picture of molecular and atomic eigenstates and energies remains relevant, but it is now possible for an atomic eigenstate to have nonzero amplitude on molecular sites, and vice-versa. In this section we explain our ansatz for the eigenstates. In the next section, we will apply it to the computation of the fractal dimensions of the eigenstates.

2.7.1. Renormalization group for the eigenstates

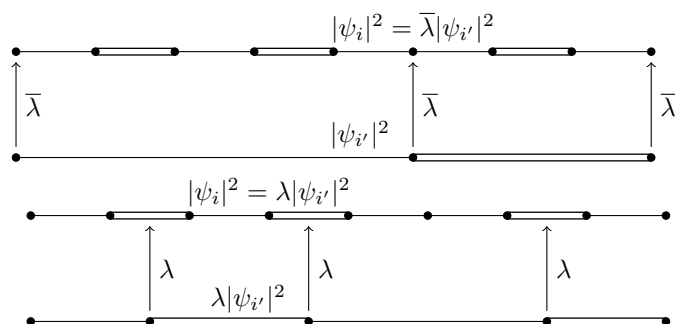


Figure 2.16. – Schematization of the RG procedure. Top figure: a eigenstate of the atomic cluster, bottom figure: a eigenstate of the molecular cluster.

At leading order in ρ , we know that the eigenstate amplitudes on the 1th approximant are related by a trivial multiplicative factor to the ones on a smaller approximant. At higher order, we still relate eigenstate coefficients on large approximants to eigenstates on smaller ones through multiplicative factors. We call these multiplicative factors $\bar{\lambda}$ if the eigenstate is of atomic type, and λ if it is of molecular type (figure (2.16)).

$$\begin{aligned} |\psi_m^{(l)}(E)|^2 &= \bar{\lambda} |\psi_{m'}^{(l-3)}(E')|^2 \text{ if } E \text{ is atomic} \\ |\psi_m^{(l)}(E)|^2 &= \lambda |\psi_{m'}^{(l-2)}(E')|^2 \text{ if } E \text{ is molecular} \end{aligned} \quad (2.46)$$

λ and $\bar{\lambda}$ are renormalization group parameters, and they play in the renormalization of the eigenstates the role z and \bar{z} plays in the renormalization of the energy bands.

We find (details of the calculations are given in Appx. D):

$$\bar{\lambda}(\rho) = \frac{2}{(1 + \rho^2)^2 + \sqrt{(1 + \rho^2)^4 + 4\rho^4}} \quad (2.47)$$

$$\lambda(\rho) = \frac{1}{1 + \rho^2\gamma(\rho) + \sqrt{1 + (\rho^2\gamma(\rho))^2}} \quad (2.48)$$

with $\gamma(\rho) = 1/(1 + \rho^2)$. At leading order in ρ , we recover $\lambda(0) = 1/2$, $\bar{\lambda}(0) = 1$ as expected. At next order,

$$\bar{\lambda}(\rho) = \frac{1}{1 + \rho^2} + \mathcal{O}(\rho^2) \quad (2.49)$$

$$\lambda(\rho) = \frac{1}{2 + \rho^2} + \mathcal{O}(\rho^2) \quad (2.50)$$

Although our calculations are done in the strong modulation limit, in the periodic limit $\rho \rightarrow 1$, we obtain the exact expression for the renormalization factors:

$$\bar{\lambda}(\rho) \xrightarrow{\rho \rightarrow 1} \omega^3 \quad (2.51)$$

$$\lambda(\rho) \xrightarrow{\rho \rightarrow 1} \omega^2 \quad (2.52)$$

2.7.2. Local eigenstate dimensions

For $q \geq 0$ and when $\rho \ll 1$, we can write

$$\chi_q^{(l)}(E) \simeq \begin{cases} (\bar{\lambda}(\rho)^q / \bar{\lambda}(\rho^q)) \chi_q^{l-3}(E') & \text{if } E \text{ is atomic,} \\ (\lambda(\rho)^q / \lambda(\rho^q)) \chi_q^{l-2}(E') & \text{if } E \text{ is molecular.} \end{cases} \quad (2.53)$$

Iterating this relation, we understand that the fractal dimensions depends only on the renormalization path of the energy E we started with. Actually, it only depends on the parameter x (2.44). Solving the recurrence we obtain an explicit expression for the fractal dimensions in the quasiperiodic limit:

$$(q-1)d_q^\psi(x) = \log \left[\left(\frac{\lambda(\rho)^q}{\lambda(\rho^q)} \right)^x \left(\frac{\bar{\lambda}(\rho)^q}{\bar{\lambda}(\rho^q)} \right)^{(1-2x)/3} \right] / \log \omega. \quad (2.54)$$

It is easy to check that we recover the first-order expression for the fractal dimensions (2.43) if we take $\rho = 0$.

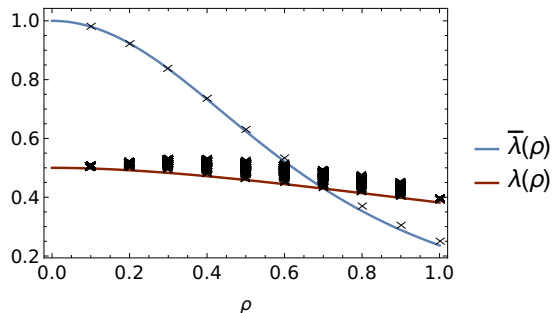


Figure 2.17. – Numerical results and theoretical predictions for the renormalization factors $\bar{\lambda}(\rho)$ and $\lambda(\rho)$. Dots: Numerical results ($l = 19, 4181$ sites). Solid lines: theoretical predictions (2.55).

From this we can express the renormalization factors in terms of the fractal dimensions for $q \rightarrow \infty$, setting $x = 0$ for $\bar{\lambda}$, and $x = 1/2$ for λ :

$$\begin{aligned}\bar{\lambda}(\rho) &= \omega^{3d_{\infty}^{\psi}(0)} \\ \lambda(\rho) &= \omega^{2d_{\infty}^{\psi}(\frac{1}{2})}\end{aligned}\tag{2.55}$$

Thus, computing numerically the fractal dimensions for q large gives us a numerical estimation of the renormalization factors, that we can compare to the theoretical predictions. We expect the agreement to be good in the strong modulation $\rho \ll 1$ and in the weak modulation $\rho \sim 1$ regimes, because we know that in these limits the renormalization factors are exact. In fact, we see that the agreement with numerics is good for all values of ρ (Fig. (2.17)).

It can be seen in Fig. (2.17) that the values of λ calculated numerically have a spread, which is not described by the theoretical formula. This is because, when ρ is far from 0 or 1, x is not enough to describe the renormalization parameter λ . One actually needs to know the whole renormalization path of the states, whereas our formula takes into account only a single parameter x . The theoretical expression gives λ accurately in only two cases: the states that are always bonding or always antibonding (ie the states at the edge of the spectrum). The states with alternating bonding and antibonding character have the largest deviation from the theoretical value, in the perturbative limit. The figure shows, as well, that the agreement with numerics is extremely good for the $\bar{\lambda}$ renormalization factor, corresponding to the eigenstate at $E = 0$. The small discrepancy between the numerics and the analytical predictions is only due to numerical finite-size effects. Indeed, the fractal dimensions of this $E = 0$ eigenstate have been determined exactly by Kohmoto et al. [1987], using trace map methods. Interestingly, these exact fractal dimensions coincide with our perturbative predictions for $\bar{\lambda}$ (2.55), for all values of ρ , meaning that our perturbative expression for $\bar{\lambda}$ is in fact exact.

We now check our theoretical predictions against numerical results. The inset of figure (2.18) shows how the fractal dimension for a given q (here we chose $q = 2$) depend on the chosen state of energy E . We observe that the value of the fractal dimension organizes in lines. Along each line $d_q^{\psi}(E)$ is constant up to small variations and corresponds to a given value $x(E) = x$. That is, up to small corrections that should vanish in the limit $\rho \rightarrow 0$, the fractal dimension of a given eigenstate does not depend on the energy E , but only on $x(E)$. This is in agreement with the theoretical predictions (2.54). Figure (2.18) shows, for example, the x dependence of the fractal dimension for $q = 2$. Calculated numerical results are seen to be in very good agreement with the theoretical predictions. As the figure shows, the multifractal properties of the eigenstates – which were not captured at leading order in ρ – are relevant, even for the small value coupling ratio $\rho = 0.1$. For $x = 0$ the first order contribution to the fractal dimensions vanishes, so that

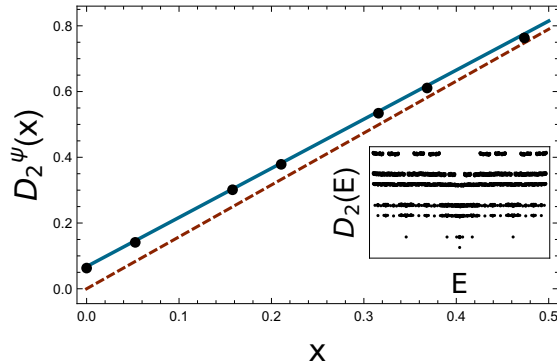


Figure 2.18. – Numerical results and theoretical predictions for the fractal dimensions of the eigenstates. Dots: Numerical results ($l = 19$, 4181 sites). Dashed line: theoretical prediction at leading order (eq. (2.43)), solid line: theoretical prediction including multifractal corrections (eq. (2.54)). Inset: The fractal dimension $d_2^\psi(E)$ for every energy. In accordance with theoretical predictions, the fractal dimensions organize in lines, each line corresponding to a given value of $x(E)$.

only the multifractal correction term remains.

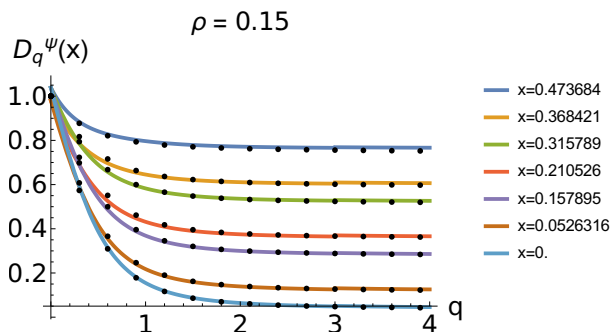


Figure 2.19. – The fractal dimensions $d_q^\psi(x)$ of the eigenstates for the different values of x accessible numerically. Dots are numerically computed data points, solid lines are the theoretical predictions (Eq. (2.54)).

To conclude this section, we show the q dependence of the fractal dimensions for fixed values of x (Fig. (2.19)). The agreement with the theoretical predictions is excellent for all positive values of q . This demonstrates that our theoretical analysis indeed captures the q dependence of the fractal dimensions. Since it is the multifractality of the eigenstates that is responsible for the nontrivial q dependence of the fractal dimensions, we conclude again that the multifractal corrections are relevant even at small coupling.

2.7.3. The spectrally averaged fractal dimensions of eigenstates

In the previous section we have defined the fractal dimensions of individual eigenstates, and have seen that they were associated with the energy level parameter x . In this section we calculate scaling properties of the eigenstates after averaging over all states. We define an averaged fractal dimension \overline{D}_q^ψ by

$$\langle \chi_q \rangle = \frac{1}{F_l} \sum_E \chi_q(E) \sim \left(\frac{1}{F_l} \right)^{(q-1)\overline{D}_q^\psi} \quad (2.56)$$

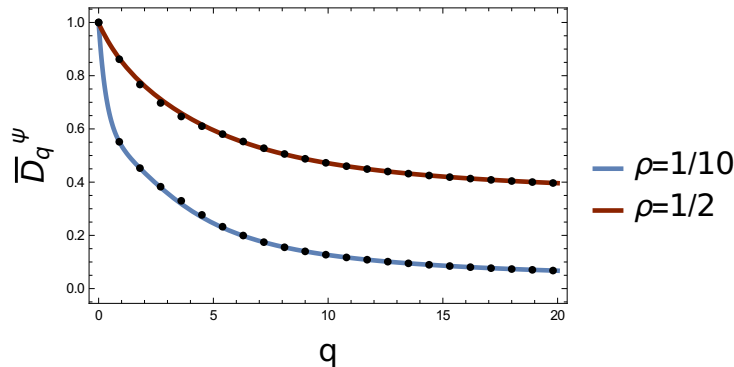


Figure 2.20. – The averaged fractal dimensions of the eigenstates \overline{D}_q^ψ as a function of the multifractal parameter q , for $\rho = 0.1, 0.5$. Dots: numerical results, solid line: theoretical predictions.

This quantity, studied in disordered systems at the Anderson localization transition [Mirlin et al. \[2006\]](#), has been computed numerically by [Thiem and Schreiber \[2011\]](#) for the Fibonacci model. Within our perturbation theory, we obtain an implicit equation for the averaged fractal dimensions:

$$2\omega^2 \frac{\lambda(\rho)^q}{\lambda(\rho^q)} \omega^{-2(q-1)\overline{D}_q^\psi} + \omega^3 \frac{\overline{\lambda}(\rho)^q}{\overline{\lambda}(\rho^q)} \omega^{-3(q-1)\overline{D}_q^\psi} = 1 \quad (2.57)$$

This equation is perturbative, valid to order ρ^{2q} . The derivation can be found in the Appendix, which also takes into account higher orders in ρ , resulting in a lengthier expression. Note the similarity of structure between (2.57) and the implicit equation obtained for the spectral dimensions (Eq. (2.37), see also [Piéchon et al. \[1995\]](#)).

The resulting theoretical predictions are compared with numerical results on a finite size system in Fig. (2.20). The agreement is excellent for all positive values of q compared to the lowest order theory used by [Thiem and Schreiber \[2011\]](#).

For larger ρ , (2.57) can be corrected to include higher order terms. The resulting theoretical prediction (see Appx. D) agrees with the numerical computations even for large ρ as shown in fig. (2.20) for the choice $\rho = 0.5$. The reason for this unexpected robustness of our perturbative theory outside its domain of validity is unclear. It supports the idea that the renormalization group picture stemming from the geometrical inflation/deflation property of the Fibonacci chain contains all the fundamental physics determining its electronic properties.

2.7.4. The local spectral dimensions and their average

In this section we consider the local density of states, and the associated fractal dimensions. For a finite-size system, the local density of states (LDoS) at site m is

$$d\mu_m(E) = \frac{1}{F_l} \sum_{a=1}^{F_l} \delta(E - E_a) |\psi_m(E_a)|^2 dE \quad (2.58)$$

The global density of states is obtained by the sum over all sites of the LDoS. The local density of states defines μ_m , the local spectral weight at site m associated to the band a of width $\Delta_a^{(l)}$:

$$\mu_m(\Delta_a^{(l)}) = \int_{E \in \text{band } a} d\mu_m(E) \quad (2.59)$$

The local spectral weight at site m sums up all the information about the spectral and eigenstate properties of the Hamiltonian. To probe the multifractality of the local density of states one defines

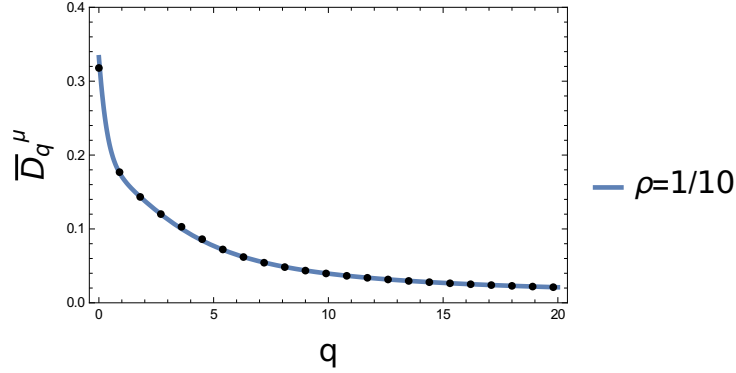


Figure 2.21. – The averaged local spectral dimensions D_q^μ as a function of the multifractal parameter q , for $\rho = 0.1$. Dots: numerical results, solid line: theoretical predictions (Eq. (2.62)).

the partition function

$$\Gamma_l(q, \tau; m) = \sum_a \frac{\left(\mu_m(\Delta_a^{(l)})\right)^q}{(\Delta_a^{(l)})^\tau} \quad (2.60)$$

using which one can compute the local spectral fractal dimensions for individual sites. One can also define a site-averaged gamma function through:

$$\langle \Gamma_l(q, \tau) \rangle = \frac{1}{F_l} \sum_m \Gamma^{(l)}(q, \tau; m) \quad (2.61)$$

The site-averaged local spectral dimensions D_q^μ , obey the implicit equation:

$$2\omega^2 \frac{\lambda(\rho)^q}{\lambda(\rho^q)} z^{(1-q)D_q^\mu} + \omega^3 \frac{\bar{\lambda}(\rho)^q}{\bar{\lambda}(\rho^q)} \bar{z}^{(1-q)D_q^\mu} = 1 \quad (2.62)$$

We compare these theoretical predictions with numerical data in Fig. (2.21) for $\rho = 0.1$ and $q > 1$, finding an excellent agreement between the two. We note, finally, that the theoretical prediction for the Hausdorff dimension D_0^μ given by the equation (2.62) agrees also well with the numerical result.

2.8. Relations between fractal dimensions and dynamical exponents

Comparing the relations (2.37), (2.57) and (2.62) for the global spectral, the average eigenstate and local spectral dimensions respectively, one sees that they bear great similarity. This suggests that there might be a relation between the three families of fractal dimensions. In this section, we present a relation between these dimensions, and, using a conjecture, relate it to the exponents of the spreading of wavepackets.

2.8.1. A relation between fractal dimensions

Consider the case $q = 0$. In this case, the local and global spectral dimensions coincide, and the eigenstate dimension is 1, so that we have $D_0^\mu = \overline{D}^{\psi_0} D_0$. A generalization of this relation appears

to hold also for all $q > 0$, namely $D_q^\mu = \overline{D^\psi}_q D_{1+(q-1)\overline{D^\psi}_q}$. This relation is satisfied numerically for values of $\rho \lesssim 0.2$. For larger values of ρ , it transforms into the inequality:

$$D_q^\mu \geq \overline{D^\psi}_q D_{1+(q-1)\overline{D^\psi}_q} \quad (2.63)$$

Numerical calculations show that this inequality appears to be satisfied for all values of $q > 0$, and for all values of ρ . It is saturated in both limits $\rho \rightarrow 0$ and $\rho \rightarrow 1$.

2.8.2. Quantum diffusion and spectral fractal dimensions

A simple way to probe the dynamical properties of a system is to study the diffusion of an initially localized wavepacket. Here, we consider a wavepacket initially localized at site $|m_0\rangle$. To study its diffusion, we track the time evolution of the q^{th} moment of the position operator, averaged over all possible starting positions of the wavepacket:

$$\langle \hat{x}^q(t) \rangle = \frac{1}{L} \sum_{m_0=1}^L \langle m_0 | e^{it\hat{H}} \hat{x}^q e^{-it\hat{H}} | m_0 \rangle. \quad (2.64)$$

For an infinite system ($L \rightarrow \infty$), we expect this observable to follow a simple scaling law of the form

$$\langle \hat{x}^q(t) \rangle \underset{t \rightarrow \infty}{\sim} t^{q\sigma_q}, \quad (2.65)$$

where we have introduced the *diffusion exponent* σ_q , containing the information about the dynamical scaling of the wavepacket. If $\sigma_q = 1$, as in the case of the periodic chain, the propagation is ballistic. For the Fibonacci chain, Piéchon [1996] found that $\sigma_q = D_{1-q}$ in the $\rho \ll 1$ limit. Based on numerical evidences for the Harper model, Piéchon [1996] went further and suggested that this relation may hold non-perturbatively.

2.8.3. An upper bound for the diffusion moments

Assuming the conjectured relation $\sigma_q = D_{1-q}$ holds true, we obtain from Eq. (2.63) the following upper bound for the diffusion exponent:

$$\sigma_{(1-q)\overline{D^\psi}_q} \leq \frac{D_q^\mu}{\overline{D^\psi}_q}. \quad (2.66)$$

This upper bound links the dynamical properties of the system (through the diffusion exponent σ), to the spectral properties (through D^μ), and the eigenstate properties (through D^ψ).

This upper bound is correct in the regime $\rho \ll 1$, but to hold non-perturbatively, the previously stated conjecture has to also hold. Unfortunately, numerical results seem to indicate a deviation when $\rho \sim 1$. Estimating accurately the diffusion exponent proved to be quite difficult, so these results need to be confirmed by more careful studies. Yuan et al. [2000] pointed out that the Piéchon conjecture may be wrong, also based on numerical results, in the case of the silver-mean chain, defined by the substitution

$$S : \begin{cases} A \rightarrow AAB \\ B \rightarrow A \end{cases}. \quad (2.67)$$

These two numerical analyses lead us to conclude that the upper bound (2.66), proposed in Macé et al. [2016], is probably incorrect, except in the regime $\rho \ll 1$.

2.9. Conclusion and perspectives

In this chapter we provide a theoretical description of the spectrum and the eigenstates of the Fibonacci pure-hopping model in the strong modulation limit, using a perturbative renormalization group scheme. We show how using the conumbering basis allows one to characterize eigenstates conveniently according to their renormalization path. We show that the system has an approximate symmetry, in the perturbative limit, under the exchange of site and energy indices. The leading order expressions for exponents are observed to agree with numerical calculations only for the smallest values of the coupling ratio ρ . We obtain the analytical description of the spectrum and eigenstates of the Fibonacci chain at next-to-leading order in ρ . These expressions show explicitly how the multifractality of eigenstates appears for larger values of ρ . The extended theory is shown to be in very good agreement with numerical results for values of ρ in a wide range from small values all the way upto ρ of order unity. Exponents for the local and global spectral measures for individual states are calculated. Averaged exponents are defined as well, and compared with numerical data.

The next stage of theoretical studies include examining the quantum diffusion properties on this chain, and verifying some of the claims we have made.

Chapter 3.

Labeling gaps of quasiperiodic chains

In this short chapter, we study the gap properties of nearest neighbor tight-binding models on quasiperiodic chains. For finite chains, we argue that two kind of gaps should be distinguished: stable and transient. We show that stable gaps have a well defined limit as the length of the chain goes to infinity. We also show that there is a direct relation between the gap size and the gap label.

Contents

3.1. The gap labeling theorem	39
3.2. Nearest neighbor tight-binding model on quasiperiodic chains	40
3.3. Application: the Fibonacci quasicrystal	40
3.3.1. Renormalization group and recursive gap labeling	41
3.3.2. Transient and stable gaps of the Fibonacci chain	42
3.4. Transient and stable gaps for generic Sturmian chains	44
3.5. Conclusion and perspectives	45

3.1. The gap labeling theorem

The gap labeling theorem (GLT) [Bellissard et al. \[1989\]](#), [Bellissard \[1992\]](#), [Bellissard et al. \[2000, 2001\]](#) is one of the few exact results known about electronic properties of one, two and three dimensional quasicrystals. It concerns the *integrated density of states* (IDOS), which is defined as $\text{idos}(E) = \text{fraction of energy states below energy } E$. Inside a spectral gap, the IDOS is of course constant, and the theorem constrains the values it can take. In the case of canonical C&P chain of slope α , the theorem states that

$$\text{idos}(E \in \text{gap}) = \frac{n}{1 + \alpha} \pmod{1} \tag{3.1}$$

where n is an integer called the label of the gap. Alternatively, one can write

$$\text{idos}(E \in \text{gap}) = \frac{n}{1 + \alpha} + m \tag{3.2}$$

with $m(n)$ the integer such that the IDOS satisfies $0 \leq \text{idos} < 1$.

The GLT can appear mysterious and profound. However, it has a simple derivation, making use of the approximants. Let $\alpha_l = p_l/q_l$ be a convergent of α . Convergents are the “best” rational approximations of a given irrational number. See the Appendix (B.3.3) for more details. Consider the periodic approximant built with α_l . Its spectrum consists in general of $N_l = p_l + q_l$ energy

bands (see Chap. 2, and Luck [1989], Sire and Mosseri [1989]), and thus the IDOS inside a gap is given by

$$\text{idos}(E \in \text{gap}) = \frac{j(E)}{N_l} \quad (3.3)$$

where $j(E)$ counts the number of bands below energy E . Since p_l and q_l are relatively prime, using Bézout's identity we can write $j = ap_l + bq_l = (a - b)q_l + bN_l$, with a and b integers. We let $n = a - b$ and we remark that

$$\text{idos}(E \in \text{gap}) = \frac{n}{1 + \alpha_l} \pmod{1} \quad (3.4)$$

Taking the quasiperiodic limit $l \rightarrow \infty$ at fixed n , we recover the GLT. Moreover, the formula (3.4) extends the GLT to approximants, which, as we will see, provides useful insight into the gap structure.

As such, the theorem contains little information: it only constrains the set of values the IDOS can take inside the gaps, but does not tell anything about the energy location of the gaps, or about their width. Nevertheless, as we shall see, the gap label n contains extra information, and is in particular relevant for characterizing the gap widths. This is not the first time the gap labeling theorem is given a physical meaning: in Levy et al. [2015] it is shown that gap labels can be interpreted as topological numbers, giving the winding number of edge states introduced in the gaps.

3.2. Nearest neighbor tight-binding model on quasiperiodic chains

In this chapter, we examine chains obtained by the canonical C&P method (see Chap. 1). We consider, just as in the previous chapter, the following model Hamiltonian where the hopping amplitude takes two values according to the quasiperiodic sequence:

$$\hat{H}(\alpha) = - \sum_m t_m |m-1\rangle \langle m| + \text{H.c.} \quad (3.5)$$

We recall that $t_m = t_A$ or $t_m = t_B$ if the letter in between sites $m-1$ and m respectively is an A or a B. Once the irrational α is fixed, the only free parameter in the model is the ratio of the two jump amplitudes $\rho = t_A/t_B$. We shall only consider, as in the previous chapter, the case where $0 < \rho < 1$.

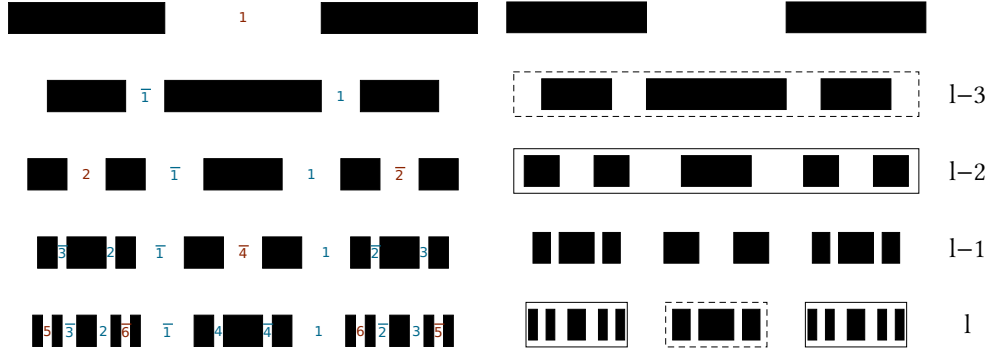
This model can be realized experimentally with light Gellermann et al. [1994] or cavity polaritons Tanese et al. [2014]. In the latter case, the details of the energy spectrum could be accurately measured, leading the authors to observe subtle phenomena such as the energy displacement of an edge state within a spectral gap. Theoretical studies of the spectral gaps are particularly relevant in these contexts.

3.3. Application: the Fibonacci quasicrystal

We now examine in detail the special case of the Fibonacci chain, and see how the gap labeling theorem adapts to the case of finite or periodic chains. The Fibonacci chain has slope $\alpha = \omega$, where $\omega = (\sqrt{5} - 1)/2$ is the inverse of the golden ratio. The gap labeling is thus

$$\text{idos}(E \in \text{gap}) = n\omega \pmod{1} \quad (3.6)$$

We recall (see Sec. 2.3.1 for more details) that the Fibonacci approximants are built with consecutive Fibonacci numbers: $p_l = F_{l-2}$, $q_l = F_{l-1}$. The l^{th} approximant has $N_l - 1 = F_l - 1$ gaps.



(a) The gap labels of the first few Fibonacci approximants. Blue: stable gaps, red: transient gaps. (b) The recursive construction of the Fibonacci spectrum.

Figure 3.1. – Energy spectra of the first few Fibonacci approximants. Here we took $\rho = 0.5$, and the spectra were approximated using the renormalization group method (see Chap. 2). On the left hand site figure, the notation $\bar{n} = -n$ was used.

Naively, we could expect all these gaps to remain open in the quasiperiodic limit $l \rightarrow \infty$. This is not true. For example, the approximants of the form $l = 3m$ have a gap at $E = 0$ (Fig. (3.1a)), but it closes in the quasiperiodic limit, as can be seen directly on the approximants, or by the fact that there is no n such that $n\omega \bmod 1 = 1/2$. We will say that such a gap is *transient*. On the contrary, the two largest gaps of the Fibonacci approximants (labeled $n = \pm 1$ see Fig. (3.1a)) appear to be *stable*: they stay open all the way to the quasiperiodic limit.

3.3.1. Renormalization group and recursive gap labeling

The behavior of an electron of the Fibonacci chain is well understood. One can show (see Chap. 2) that the spectrum of the l^{th} approximant can be approximated by a simple linear combination of the spectra of the approximants $l-2$ and $l-3$ (Fig. (3.1b)). This provides us with a recursive gap labeling procedure. Let $\mathbf{g} = (m, n)$ be the vector containing the labels of a gap (3.1). Let G_l be the set of all gap labels \mathbf{g} of the l^{th} approximant. Using the recursive spectrum construction of figure (3.1b) we see that G_l can be partitioned into 3 subsets containing the gap labels of the left, central and right clusters of energy bands. We have the following recursive relations:

$$\begin{aligned} G_l^{\text{left}} &= S^{-2} G_{l-2} \\ G_l^0 &= S^{-3} G_{l-3} + \mathbf{g}_1 \\ G_l^{\text{right}} &= S^{-2} G_{l-2} + \mathbf{g}_2 \end{aligned} \quad (3.7)$$

where $\mathbf{g}_1 = (1, -1)$ and $\mathbf{g}_2 = (0, 1)$ are the labels of the two main gaps (corresponding to $n = \pm 1$, see figure (3.1a)), and S is the geometrical substitution matrix

$$S = \begin{bmatrix} 1 & 1 \\ 1 & 0 \end{bmatrix} \quad (3.8)$$

that can be used to generate the Fibonacci sequence (see Sec. 2.3). Let us prove this formula.

Proof 1 (Recursive gap labeling for Fibonacci) Let g be the IDOS of a gap in G_{l-2} . Let g' be the IDOS of the unique gap in G_l^{left} under which there are as many bands as below g . In other words, g' verifies

$$F_l g' = F_{l-2} g. \quad (3.9)$$

By virtue of formula (3.4), one can write $g = nF_{l-3}/F_{l-2} + m$, and $g' = n'F_{l-1}/F_l + m'$. One has therefore the following relation between gap labels:

$$m'F_l + n'F_{l-1} = mF_{l-2} + nF_{l-3}. \quad (3.10)$$

For a, b integers, we introduce the following notation:

$$\begin{bmatrix} a \\ b \end{bmatrix}_l = aF_l + bF_{l-1} \quad (3.11)$$

Let us call the left hand side of this equation an “ l -vector”. One can pass from an l -vector to an $l+1$ -vector by applying the Fibonacci substitution matrix S :

$$\begin{bmatrix} a \\ b \end{bmatrix}_{l+1} = \left[S \begin{pmatrix} a \\ b \end{pmatrix} \right]_l \quad (3.12)$$

Moreover, two l -vectors whose components are strictly smaller than F_l in modulus are equal if and only if their components are equal:

$$\begin{bmatrix} a \\ b \end{bmatrix}_l = \begin{bmatrix} a' \\ b' \end{bmatrix}_l \Leftrightarrow \begin{pmatrix} a \\ b \end{pmatrix} = \begin{pmatrix} a' \\ b' \end{pmatrix} \quad (3.13)$$

This property simply follows from the fact that the two consecutive Fibonacci numbers F_{l-1} and F_l are coprime. Now, the equation (3.10) can be rewritten in l -vector form as

$$\begin{bmatrix} m' \\ n' \end{bmatrix}_l = \left[S^{-2} \begin{pmatrix} m \\ n \end{pmatrix} \right]_l \quad (3.14)$$

which leads to the equality between vectors:

$$\begin{pmatrix} m' \\ n' \end{pmatrix} = S^{-2} \begin{pmatrix} m \\ n \end{pmatrix} \quad (3.15)$$

This proves the first line of (3.7). The other two lines can be proven similarly.

This recursive relation provides us with a very simple geometrical interpretation of the GLT, in the simple case of the Fibonacci chain. Let us see why.

3.3.2. Transient and stable gaps of the Fibonacci chain

As we already point out earlier on, the gap at $\text{idos} = 1/2$ is transient. Indeed, calling Δ_0 the width of this gap at step $l = 0$ (see Fig. (3.1a)), we see that the width of this gap at step $l = 3m$ is

$$\Delta_{l=3m} = \bar{z}^m \Delta_0 \quad (3.16)$$

which indeed goes to 0 in the quasiperiodic limit $l \rightarrow \infty$.

Transient gaps

We say that a gap g' is an iterate of a gap g if g' is constructed from g by a RG operation. For example, the leftmost gap of the third approximant shown on Fig. (3.1a) is constructed from the gap of the first approximant by a RG molecular operation; it is thus an iterate of this gap. Iterates verify $\Delta_l(g') = z\Delta_{l-2}(g)$ or $\Delta_l(g') = \bar{z}\Delta_{l-3}(g)$. By extension, we also call iterates gaps that are constructed from a given gap by several RG operations. With this definition, it is clear that *all iterates of the transient gap at $\text{idos} = 1/2$ are also transient*. They are marked in red on Fig. (3.1a). We will show that they are the only transient gaps.

Stable gaps

The two main gaps which separate the atomic and the molecular clusters are stable. To prove it, let us compute their width Δ_l in perturbation theory and show that it is non zero in the quasiperiodic limit. One has

$$\Delta_l = t_B - \frac{\bar{z}}{2}W_{l-3} - \frac{z}{2}W_{l-2} \quad (3.17)$$

where W_l is the width of the spectrum of the l^{th} approximant. We easily check that

$$\Delta_l \xrightarrow{l \rightarrow \infty} t_B(1 - z) + \mathcal{O}(\rho^2) \quad (3.18)$$

which is indeed nonzero. Now, it is clear that all iterates of the two main gaps are also stable. Because all gaps are either iterates of the two main gaps or of the gap at $\text{idos} = 1/2$, we conclude that *a given gap is either an iterate of the gap at $\text{idos} = 1/2$, and is in this case transient, or is an iterate of one of the two main gaps, and is in this case stable.* On Fig. (3.1a) stable gaps are marked in blue and transient gaps in red.

Labeling of transient and stable gaps

When it exists (i.e. when l is a multiple of 3), the central gap has label

$$n_l = \frac{F_l}{2}. \quad (3.19)$$

So, the label of the central gap varies from approximants to approximants, while its IDOS stays constant. This is true for all transient gaps, since they are iterates of the central gap. For stable gaps, it is the other way around: their labeling is fixed, while their IDOS varies from approximants to approximants (but converges to a well defined value).

Conclusion to Fibonacci gap labeling

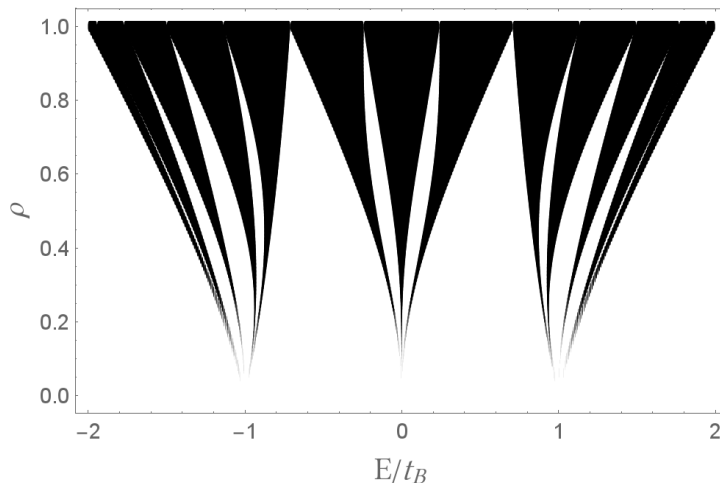


Figure 3.2. – Spectrum of the approximant $l = 6$ (13 sites) as a function of the parameter ρ .

On the example of the Fibonacci chain, we see how the GLT can be extended to the approximants, at the price of introducing transient gaps that are not present in the spectrum of the quasiperiodic system. Transient and stable gaps can be recursively characterized: the former are the iterates by the RG of the central gap, while the latter are the iterates of the two main gaps.

We used perturbation theory in the strong quasiperiodicity limit ($\rho \ll 1$) to derive all the results above. However, the conclusions states here remain valid *non-perturbatively*, as no gap closes when ρ is varied between 0 and 1, as shown on Fig. (3.2).

We now turn to the general characterization of the transient and stable gaps in the case of an arbitrary C&P chain.

3.4. Transient and stable gaps for generic Sturmian chains

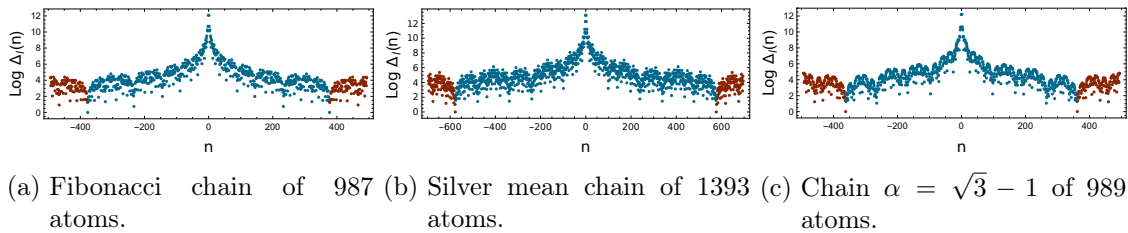


Figure 3.3. – Gap width as a function of gap label for several quasiperiodic chains. Blue: stable gap, red: transient gaps, according to criterion (3.21). The ratio of the couplings was set arbitrarily to $\rho = 0.5$.

In the previous part, we considered a gap centered around energy \bar{E} to be transient if its width $\Delta_l(\bar{E})$ vanished in the quasiperiodic limit:

$$\Delta_l(\bar{E}) \xrightarrow{l \rightarrow \infty} 0. \quad (3.20)$$

We introduce here a practical criterion to distinguish between transient and stable gaps. Let $\bar{E}_l(n)$ be the mean energy inside the gap of label n , for the l^{th} approximant. Define the displacement of a gap as $D_l(n) = |\bar{E}_{l+1}(n) - \bar{E}_l(n)|$. We say the gap n at step l is transient if its half-width does not overlap significantly its counterpart at step $l + 1$, ie if

$$D_l(n) > \frac{a(\rho)}{2} (\Delta_l(n) + \Delta_{l+1}(n)), \quad (3.21)$$

and stable otherwise. We have introduced the *overlap coefficient* $a(\rho)$, which quantifies the extent of overlap we require for a gap to be considered stable. We require $a \leq 1$, since otherwise the gaps at step l and $l + 1$ do not overlap at all. Numerically, we determine a by requiring that any stable gap at step l overlaps their counterpart at step $l + l'$ with l' arbitrarily large. As the ratio of the couplings ρ is decreased, gaps are enlarged and overlap more and more. Thus, the value of a also decreases with ρ . As an example, we find $a(0.5) = 0.5$ for the Fibonacci chain.

It is easy to see that criterion (3.21), applied to the Fibonacci chain, yields the same stable and transient gaps as criterion (3.20). It is not trivial that these two criteria are in general equivalent. However, it does appear to be the case for all the quasiperiodic chains we tested numerically. We will therefore consider them equivalent from now.

Figures (3.3a) (3.3b) (3.3c) show the widths of the gaps as a function of their label, for various quasiperiodic chains. The global structure is similar in every case: the gap width is a globally decreasing function of the gap index (this is consistent with perturbation theory in the limit $\rho \rightarrow 1$, see e.g. Luck [1989]). Here we also observe that width decreases as a power-law of the index, as shown on Fig. (3.4). In the case of the Fibonacci chain (Fig. (3.4a)), we notice log-periodic oscillations. We make the hypothesis that these log-periodic oscillations, frequently observed in fractal systems, come from the discrete scale invariance of the Fibonacci Hamiltonian (Eq. (2.33)). See appendix A.5 for a more detailed discussion on the link between discrete scale invariance and

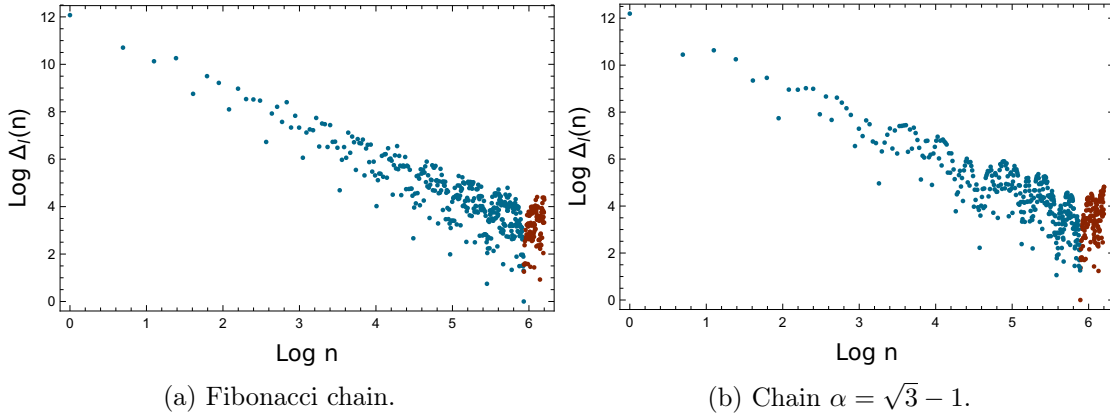


Figure 3.4. – Gap width as a function of gap label in log-log scale, for the same parameters as in Fig. (3.3).

log-periodic oscillations. In the case of the $\alpha = \sqrt{3} - 1$ chain (Fig. (3.4b)), we observe oscillations but cannot identify them as log-periodic. We conjecture that this is related to the fact that for this chain, the Hamiltonian cannot be written in a discrete scale invariant way similar to that of Eq. (2.33).

Finally, we observe that regardless of the chosen irrational α , there is a critical label above which all gaps are transient, and below which all gaps are stable.

3.5. Conclusion and perspectives

We have shown that the well known GLT is applicable not just to quasiperiodic chains but also to their approximants. The price to pay is the introduction of *transient gaps*, which vanish in the quasiperiodic limit. Fortunately, these gaps are easy to spot: they always have the highest gap label.

Moreover, we show that the gap label contains relevant physical information: it globally orders the gaps by decreasing width, and separates stable from transient gaps. The gap label, which had *a priori* no physical content, thus appears physically relevant.

A gap label is robust under deformation of the Hamiltonian, as long the gap does not close. This indicates that it is of topological nature. More precisely, when a defect is introduced in the chain, creating edge states, Levy et al. [2015] showed a direct correspondence between the gap labels and the winding number of the corresponding edge states.

Open problems include more finely describing the behavior of the gap width with the index and extending this description to higher dimensional quasicrystals, which are also known to have gaps Zijlstra [2004], de Prunelé [2002].

Chapter 4.

Some exact eigenstates on 1D and 2D quasiperiodic tilings

We present exact solutions for some eigenstates of hopping models on one and two dimensional quasiperiodic tilings and show that they are critical states, by explicitly computing their multifractal spectra. These eigenstates are shown to be generically present in 1D quasiperiodic chains. We then describe properties of the ground states for a class of tight-binding Hamiltonians on the 2D Penrose and Ammann-Beenker tilings. Exact and numerical solutions are seen to be in good agreement.

Contents

4.1. SKK state on the Fibonacci chain, and its properties	49
4.1.1. The Fibonacci chain and hopping Hamiltonian	49
4.1.2. The $E = 0$ eigenstate	50
4.1.3. Arrows and height field	50
4.1.4. Diffusion equation for the height function	52
4.2. Multifractal properties of SKK states	54
4.2.1. Fractal dimensions of a generic SKK state	54
4.2.2. The fractal dimensions of the $E = 0$ state of the Fibonacci chain	56
4.3. Transmission coefficient on the Fibonacci chain	56
4.4. SKK states on other aperiodic chains	58
4.4.1. SKK states on chains of the metallic mean series	58
4.4.2. Absence of SKK state on the b3 non-Pisot substitution	59
4.5. Discussion and conclusions for 1D chains	60
4.6. SKK states on 2D tilings and their properties	60
4.6.1. Tight-binding models on 2D tilings	61
4.6.2. Properties of the 2D height field. Fractal dimensions of the ground state.	62
4.6.3. Results for the AB tiling	65
4.6.4. A variational calculation for the ground state	69
4.6.5. Varying the on-site potential	70
4.6.6. Results for the Penrose tiling	72
4.6.7. Discussion and conclusions for 2D quasicrystals	74
4.7. Are the ground states of 1D chains SKK states?	74
4.7.1. SKK states and logarithmic derivative	75
4.7.2. Computing the logarithmic derivative	75
4.8. Conclusion and perspectives	77

Introduction

As we have discussed in previous chapters, there are many results concerning non-interacting electrons on 1D quasicrystals. Many spectral properties of quasiperiodic chains are known (Chap. 3), and the eigenstates are also well characterized (Chap. 2). In contrast, even the simplest models of 2 and 3 dimensional quasicrystals have resisted theoretical investigations. Consider for example the Ammann-Beenker tiling (Fig. (4.1)), and a tight-binding model for non-interacting electrons hopping between nearest neighbor vertices on this tiling:

$$\hat{H} = -t \sum_{\langle m,n \rangle} |n\rangle \langle m| + \text{H.c.} \quad (4.1)$$

Although this Hamiltonian is simple, no solutions were known for any of its eigenstates, apart from trivial confined eigenstates at the middle of the spectrum [Kohmoto and Sutherland \[1986\]](#). Such states are not specific to quasiperiodic systems, and may be present in tight-binding models on other bipartite lattices as, for example, the T3 (“dice”) lattice.

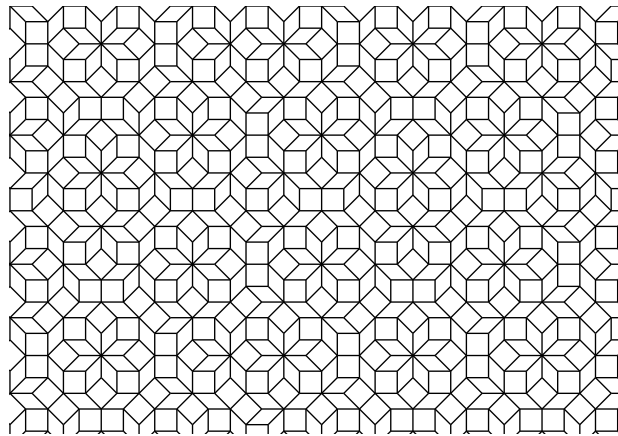


Figure 4.1. – A patch of the Ammann-Beenker tiling.

This situation changed recently, when [Kalugin and Katz \[2014\]](#), building on the work of [Sutherland \[1986\]](#), deduced the form of the ground state of the Hamiltonian (4.1) on the Penrose and Ammann-Beenker tilings.

Taking their cue from periodic crystals, where Bloch states are given by $\psi_k(r) = u_k(r)e^{ik \cdot r}$ with u a periodic function, [Kalugin and Katz \[2014\]](#) proposed that the ground state of the model (4.1) be given by a product of two factors, namely

$$\psi(m) = C(m)e^{\kappa h(m)} \quad (4.2)$$

In this expression, κ is a real constant (note that in [Kalugin and Katz \[2014\]](#) the notation $\lambda = \exp(2\kappa)$ is used). The pre-exponential factor $C(m)$ of the ansatz (4.2) is a quasiperiodic function, a site-dependent amplitude which depends only on the arrangement of the atoms around the site m . In other words, $C(m) \simeq C(n)$ if the arrangement of the atoms around site m matches the arrangement of the atoms around site n out to a large distance. The non-local *height field* $h(m)$ in the exponential depends on the geometrical properties of the tiling. We will refer to eigenstates of this form henceforth as Sutherland-Kalugin-Katz – or SKK eigenstates.

In this chapter, we consider generalizations of the results of Kalugin and Katz to other tight-binding models. We consider first the relatively simple case of models on 1D quasiperiodic chains, and show that they admit eigenstates of a form similar to that given in Eq. (4.2). These states

are found in the center of the spectrum. On the other hand the ground states of the 1D models we consider do not generically have this type of structure, as we will explain in Sec. 4.7.

Considering 2D tight-binding models on the Ammann-Beenker and Penrose tilings, we show that the ground states continue to have the SKK structure even when the Hamiltonian (4.1) is generalized to include onsite potentials. We show that these eigenstates are *critical*, i.e. neither localized nor extended, by an explicit analytical calculation of generalized fractal dimensions. These exact results provide confirmation of a long-held surmise based on numerical calculations Rieth and Schreiber [1998].

This chapter is organized as follows. In section 4.1, we examine the $E = 0$ state of the Fibonacci chain and show that it is of the SKK type. We discuss some of the properties of this state. In section 4.2 we show how the fractal dimensions of an SKK state can be computed from the asymptotics of the distribution of heights. We apply this result to the case of the Fibonacci chain. In section 4.4 we consider how the $E = 0$ state differs from one aperiodic chain to another. In section 4.6, we consider models on two dimensional tilings, namely the Ammann-Beenker and Penrose tilings. We show that they are SKK eigenstates, whose multifractal properties are calculated and compared with numerical data. Finally, in Sec. 4.7 we go back to the 1D case to show that, contrary to the 2D case, the ground state is not of the SKK type.

4.1. SKK state on the Fibonacci chain, and its properties

In this section, we will focus on one-dimensional models, which provide a good starting point in the study of SKK-like eigenstates. For definiteness, we begin with the example of the Fibonacci chain. Hopping models on a number of different aperiodic chains will be discussed later (Sec. 4.4).

4.1.1. The Fibonacci chain and hopping Hamiltonian

It will be useful in the following discussion to introduce some notation, along with a reminder of basic definitions already introduced in chapters 1 and 2. We recall that the Fibonacci substitution rule S , acting on the two letters alphabet $\mathcal{A} = \{A, B\}$, writes

$$S : \begin{cases} A \rightarrow AB \\ B \rightarrow A. \end{cases} \quad (4.3)$$

Letting the substitution act repeatedly on the letter B generates a sequence of words $C_l = S^l(B)$ of increasing length. Note that the lengths of the words are Fibonacci numbers. In the limit $l \rightarrow \infty$, one obtains an infinite Fibonacci word (see Chap. 1 for more details on symbolic substitutions).

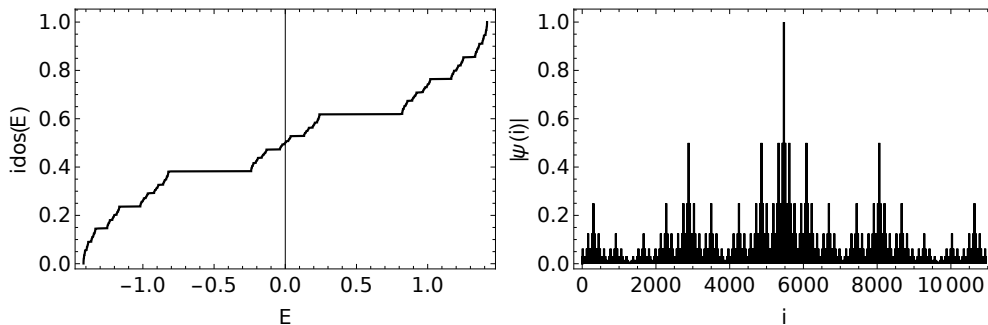
Still following Chap. 2, to the Fibonacci word we associate a collection of hopping amplitudes $\{t_m\}$, in the following way:

$$t_m = \begin{cases} t_A & \text{if the letter } m \text{ is } A \\ t_B & \text{if the letter } m \text{ is } B. \end{cases} \quad (4.4)$$

The Fibonacci Hamiltonian is then built using this sequence of hoppings:

$$\hat{H} = - \sum_m t_m |m\rangle \langle m+1| + \text{H.c} \quad (4.5)$$

In anticipation of the two-dimensional model of Sec. 4.6, and at the risk of belaboring the obvious, we note that the letters A and B play the role of 1D tiles, and that “atoms” are located in between the tiles. Up to a global rescaling of the energies, the only free parameter of this Hamiltonian is the ratio of the two hopping amplitudes $\rho = t_A/t_B$. If $\rho = 1$ the chain is periodic.



(a) The integrated density of states of the model (4.5) with $\rho = 0.5$. (b) Absolute value of wavefunction amplitudes in the $E = 0$ state.

Figure 4.2.

If $\rho = 0$ or $\rho = \infty$ the chain is a collection of decoupled molecules. We will exclude these 3 trivial cases and assume $\rho \neq 0, 1, \infty$ henceforth.

As seen in Chap. 2, the spectrum of the Fibonacci Hamiltonian is fractal Sütő [1989], as illustrated in the top panel of Fig. (4.2) which shows the integrated density of states, $\text{idos}(E)$ defined by the fraction of states of energy smaller than E . The fractal dimensions of the spectrum can be computed in the limits $\rho \sim 1$ (see Rüdinger and Sire [1996]) and $\rho \ll 1$ (see Piéchon et al. [1995] and Sec. 2.4.2 of this thesis). The structure of the eigenstates is also well understood in these two limits, as discussed in sections 2.6 and 2.7.

Away from these limits, however, the structure of the eigenstates is not known, with the notable exception of the $E = 0$ state at the center of the spectrum shown in Fig. (4.2). This state is of the SKK type, as we will discuss in the next section. In contrast, as we mentioned in the introduction, the 1D ground state does *not* have the SKK form, for reasons which will be discussed in Sec. 4.7.

4.1.2. The $E = 0$ eigenstate

The Hamiltonian (4.5) is particle-hole symmetric, i.e., to an eigenstate at energy E corresponds an eigenstate at energy $-E$, which is related to the former by a sign change on the subchain of even (or odd) sites. In particular, the central state at $\text{idos} = 1/2$, which we wish to study, has energy $E = 0$ and is doubly degenerate. We recall that this state can be built using the so-called trace-map method, used for instance by Fujiwara et al. [1989] to obtain a description of this state, and in particular to compute its fractal dimensions. The fractal dimensions of this state can also be computed exactly using a renormalization-group approach as we discussed in Sec. 2.7. We wish to show now that the $E = 0$ state is an SKK like state (4.2). To do this, we first introduce a decoration of the chain by *arrows* and a *height field* which is the integral of the arrows.

4.1.3. Arrows and height field

The tight-binding equations (4.5) for the central state are

$$t_{m+1}\psi(m+2) + t_m\psi(m) = 0 \quad (4.6)$$

Even and odd subchains are seen to be completely decoupled, so that one of the two $E = 0$ eigenstates can be chosen to vanish on the odd subchain, and the other state to vanish on the even subchain. We focus on the first of these eigenstates, designated by ψ . By symmetry all the same properties will also hold for the state living on the odd sites.

Rewriting the tight-binding equations (4.6), we have

$$\psi(2(m+1)) = -\rho^{a(2m \rightarrow 2(m+1))}\psi(2i) \quad (4.7)$$

4.1. SKK state on the Fibonacci chain, and its properties

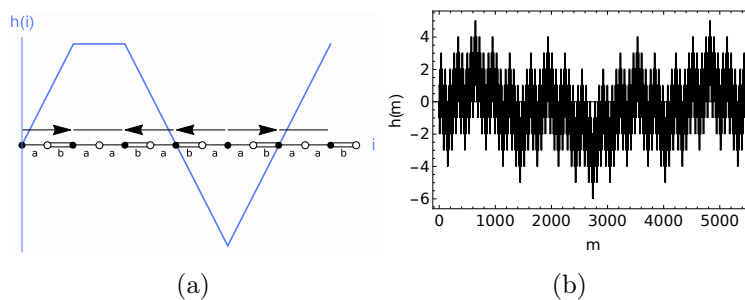


Figure 4.3. – (a): A segment of the Fibonacci chain showing a sequence of t_A (single bond) and t_B (double bond) couplings. The arrow field and the associated height field are shown for one of the subchains (the blue line is drawn to guide the eye). (b): The height field on a larger piece of the Fibonacci chain.

where we have introduced the *arrow function* a , defined on *pairs* of bonds, as follows

$$a : \begin{cases} a(AB) & = +1 \\ a(BA) & = -1 \\ a(AA) & = 0 \\ a(BB) & = 0 \end{cases} \quad (4.8)$$

where the last case of two consecutive B-bonds, not present in the Fibonacci chain, is included for future generalizations. The name “arrow” refers to the fact that one can associate to each pair of bonds an arrow pointing to the right (+1), or to the left (-1) or neither (0), cf Fig. (4.3).

Iterating the relation (4.7), one obtains the eigenstate in terms of a height function, $h(m)$

$$\psi(2m) = (-1)^m \rho^{h(m)} \psi(0) \quad (4.9)$$

where

$$h(m) = \sum_{0 \leq i < m} a(2i \rightarrow 2(i+1)) \quad (4.10)$$

The height function is thus the integral of the arrow field (see Fig. (4.3)) which is itself determined by the quasiperiodic structure of the chain. Comparing Eq. (4.9) with Eq. (4.2), one sees that the central state itself has not the SKK form, but writes as the product of an SKK and a periodic function:

$$\psi(2m) = (-1)^m \exp(\kappa h(2m)) \quad (4.11)$$

with $\kappa = \log(\rho)$. In the periodic limit $\rho \rightarrow 1$, one recovers the Bloch state $\psi(2m) = (-1)^m$.

Note that the reasoning leading to Eq. (4.9) is valid for an *arbitrary* sequence of couplings, random or deterministic. It is instructive to consider an example of a disordered chain for which the distribution of A-bonds and B-bonds is random. Consider to fix the ideas the case of A and B bonds distributed randomly, independently and in equal proportion along the chain. Then the arrow function is randomly distributed, with zero mean $\langle a \rangle = 0$, and the distribution of heights for the random chain is Gaussian, by virtue of the central limit theorem. The typical height corresponds to the standard deviation which is

$$\sigma^{rand}(m) \underset{m \rightarrow \infty}{\sim} \sqrt{m} \quad (4.12)$$

to leading order in m . Eq. (4.9) then implies that the wavefunction must have a stretched exponential form, since typical amplitude on the $2m^{\text{th}}$ site $|\psi(2m)| \sim e^{-cst\sqrt{m}}$. This form, first

shown for off-diagonal disordered models by Soukoulis and Economou [1981], is particular to the zero energy state, all other states being exponentially localized. The $E = 0$ state of the random system is very different from that of the quasiperiodic chain, where the typical height on site m scales as $\sqrt{\log m}$, as we will show next.

4.1.4. Diffusion equation for the height function

In the following, we consider how to characterize the height field for the hopping model on the Fibonacci chain. Let us define $r = AB$ (letter corresponding to a right arrow), $l = BA$ (letter corresponding to a left arrow), and $u = AA$ (letter corresponding to no arrow). In the case of the Fibonacci chain, as we noted before, the group BB never occurs.

The Fibonacci substitution rule (4.3) iterated three times results in an effective substitution rule S' for the arrows:

$$S' : \begin{cases} r \rightarrow rull \\ l \rightarrow rulr \\ u \rightarrow rullr \end{cases} \quad (4.13)$$

Let $\mathbf{v} = (N_r, N_l, N_u)$ be a vector whose entries are respectively the number of right, left and null arrows on a given chain. Upon inflation of this chain (4.13), it is transformed to $M\mathbf{v}$ where

$$M = \begin{bmatrix} 1 & 2 & 2 \\ 2 & 1 & 2 \\ 1 & 1 & 1 \end{bmatrix}. \quad (4.14)$$

The *inflation matrix* M provides information about the distribution of arrows. In particular, the relative frequencies of the arrows are given by the Perron–Frobenius eigenvector (i.e. the eigenvector associated with the largest eigenvalue). Here, one finds

$$\begin{aligned} f(r) &= \tau^{-2} \\ f(l) &= \tau^{-2} \\ f(u) &= \tau^{-3}, \end{aligned} \quad (4.15)$$

where τ is the golden ratio.

The substitution S' replaces a given arrow by a block of arrows. Notice that the effective arrow corresponding to this superblock is reversed compared to the original one. In other words, the substitution S' preserves the heights of the initial and final sites *up an overall sign*. Thus, under a single application of S' , sites of large (resp. small) wavefunction amplitude switch roles. Wavefunction amplitudes are left invariant when the substitution is applied an even number of times. This observation leads one to conclude that the wavefunction is probably delocalized, since the substitution acts to “push sites further apart”. Thus, the eigenstate has non-zero amplitude on sites that can be pushed arbitrarily far apart, and hence is not a localized state.

Consider now the sequence of regions of larger and larger size obtained by applying the substitution S' to an original region \mathcal{R}_0 :

$$\mathcal{R}_0 \xrightarrow{S'} \mathcal{R}_1 \xrightarrow{S'} \dots \xrightarrow{S'} \mathcal{R}_t \xrightarrow{S'} \mathcal{R}_{t+1} \xrightarrow{S'} \dots \quad (4.16)$$

Let us now focus on the height distribution function, which gives the number of times the height h is reached inside the region \mathcal{R}_t , and is relevant for the computation of the fractal dimensions of the central ($E = 0$) state. One can define environment-specific distributions, $N_\mu^{(t)}(h)$, where μ denotes the local environment. There are three different local environments on the Fibonacci chain which we define according to the nature of the arrow immediately following the site, namely,

4.1. SKK state on the Fibonacci chain, and its properties

$\mu = r, l, u$, appearing with the frequencies (4.15). The $N_\mu^{(t)}(h)$ give the number of times height h is found on the local environment μ in region \mathcal{R}_t . They are the three components of the vector $\mathbf{N}^{(t)}(h)$ which evolves with each inflation step.

We now write the recurrence formula which relates the vector $\mathbf{N}^{(t)}$ to $\mathbf{N}^{(t+1)}$. Recall that, after one inflation, the new heights are equal to the previous heights plus a shift of ± 1 or 0, and they undergo a change of sign. Introducing a *generalized inflation matrix* that operates on the heights, as discussed in Sutherland [1987], Tokihiro et al. [1988], Repetowicz et al. [1998], we find

$$\mathbf{N}^{(t+1)}(-h) = \sum_{h'=-1}^1 M(h')\mathbf{N}^{(t)}(h-h'), \quad (4.17)$$

where the 3×3 $M(h')$ matrices are termed generalized inflation matrices. $M_{\mu,\nu}(h)$ counts the number of times the environment μ corresponding to height h appears in $S'(\nu)$, the inflation of the environment ν associated to height 0. Their explicit expressions are given by

$$M(-1) = \begin{bmatrix} 0 & 0 & 1 \\ 0 & 0 & 0 \\ 0 & 0 & 0 \end{bmatrix} \quad (4.18)$$

$$M(0) = \begin{bmatrix} 1 & 2 & 1 \\ 1 & 0 & 1 \\ 0 & 0 & 0 \end{bmatrix} \quad (4.19)$$

$$M(1) = \begin{bmatrix} 0 & 0 & 0 \\ 1 & 1 & 1 \\ 1 & 1 & 1 \end{bmatrix} \quad (4.20)$$

Note that the sum of the generalized inflation matrices, $M = \sum M(h')$, is just the inflation matrix M of Eq. (4.14).

Eq. (4.17) is a Fokker-Planck-like equation, in which the number of inflations, t , plays the role of time, the height h plays the role of a spatial variable, and the generalized inflation matrices $M(\delta h)$ are transition rates. As such, one expects that the height frequency $P_\mu^{(t)}(h) = N_\mu^{(t)}(h) / \sum_h N_\mu^{(t)}(h)$ will converge to a Gaussian form in the large time limit. We prove that it is indeed the case for the Fibonacci chain, as well as for general substitutions under reasonable assumptions.

In order to do this, we introduce the generating function of the probability distribution (the *partition function*):

$$Z_\mu^{(t)}(\beta) = \sum_{h \in \mathbb{Z}} N_\mu^{(t)}(h) e^{\beta h} \quad (4.21)$$

The evolution equation (4.17) is recast to

$$\mathbf{Z}^{(t+2)}(\beta) = \tilde{M}(-\beta)\tilde{M}(\beta)\mathbf{Z}^{(t)}(\beta), \quad (4.22)$$

where $\tilde{M}(\beta) = \sum_h M(h) \exp(-\beta h)$, and where we iterated twice to take care of the sign change. From this recursion relation, and since all the coefficients of \tilde{M} are strictly positive, the Perron-Frobenius theorem applies, and the large time behavior of the partition function must be of the form

$$Z_\mu^{(2t)}(\beta) \underset{t \rightarrow \infty}{\sim} \omega^t(\beta) f_\mu(\beta), \quad (4.23)$$

where $\omega(\beta)$ is the largest eigenvalue of $\tilde{M}(-\beta)\tilde{M}(\beta)$, and $f_\mu(\beta)$ is the associated eigenvector. Explicit calculation gives

$$\omega(\beta) = \left(\frac{(1 + e^\beta)^2 + \sqrt{(1 + e^\beta)^4 + 4e^{2\beta}}}{2e^\beta} \right)^2. \quad (4.24)$$

Thus, in the $t \rightarrow \infty$ limit, the distributions all converge to the Gaussian distribution:

$$P_\mu^{(t)}(h) \sim \frac{f_\mu}{\sqrt{4\pi Dt}} \exp\left(-\frac{h^2}{4Dt}\right), \quad (4.25)$$

where D – which we call the diffusion coefficient by analogy with a diffusion process – is given by

$$D = \frac{1}{4} \frac{\partial^2 \log \omega}{\partial \beta^2} \Big|_{\beta=0} = \frac{1}{2\sqrt{5}}. \quad (4.26)$$

The typical height is given by the standard deviation, and grows like $\sigma^{\text{Fib}}(y) \sim \sqrt{2Dt}$, while the length of the chain, after t inflations is $L^{(t)} \sim \tau^{3t} L^{(0)}$. Thus, on a piece of tiling of size L , the typical height scales as $\sigma^{\text{Fib}}(L) \sim \sqrt{\log L}$. The wavefunction amplitudes should therefore typically decrease more slowly than for the random case we discussed earlier. We will show in the next section that the eigenstate is in fact a critical state, by explicitly computing its fractal dimensions.

A few comments can be made at this point: we note that the scaling of the partition function (4.57) and the Gaussian nature of the height distribution are generic properties. They will hold for any height field on any substitution tiling, provided that the height is invariant (up to a sign) under inflation, and provided that the entries of the corresponding inflation matrix M are strictly positive. These two properties hold for the 1D and 2D quasiperiodic substitution tilings we will discuss below, namely, the series of metallic mean chains in 1D, and the Penrose and Ammann-Beenker tilings in 2D. Only the particular form of $\omega(\beta)$ varies, depending on the tiling and the height field. In contrast, these properties do not hold for the b3 chain which is not quasiperiodic (see below).

Additionally, note that although the arrows can be constructed from the local environments, their integral, the height field, is distributed in an environment-independent fashion¹. This property implies that the fractal dimensions of the SKK eigenstates (4.2) depend only on the distribution of heights, as we will now see.

4.2. Multifractal properties of SKK states

Fractal dimensions are a way to completely and compactly characterize fractal sets, as discussed in more details in the Appendix A. Here, just like in Chapter 2, we analyze the fractal properties of the probability distribution $|\psi|^2$ of the electron in a given eigenstate. As explained in A.2.3, the q -mass of the eigenstate ψ is then defined as:

$$M_q(\psi, \mathcal{R}) = \frac{\sum_{m \in \mathcal{R}} |\psi(m)|^{2q}}{\left(\sum_{m \in \mathcal{R}} |\psi(m)|^2\right)^q} \quad (4.27)$$

where the sums run over all sites in a given region \mathcal{R} . The Rényi entropy is a measure of the fraction of the presence probability contained inside region \mathcal{R} .

4.2.1. Fractal dimensions of a generic SKK state

We begin by computing the fractal dimensions of a generic SKK state, and we later specialize (in Subsec. 4.2.2) to the case of the $E = 0$ state on the Fibonacci chain, introduced previously in Sec. 4.1.

1. This non-trivial fact can be understood in the context of the tiling cohomology: the height function is an element of the first cohomology group of the tiling, and as such, it cannot depend on the local environment [Sadun \[2015\]](#).

Let us consider a sequence of regions \mathcal{R}_t whose size grows to infinity. The q^{th} fractal dimension, $d_q(\psi)$, is the scaling of the q -mass with the volume of the region:

$$d_q(\psi) = \lim_{t \rightarrow \infty} \frac{-1}{q-1} \frac{\log M_q(\psi, \mathcal{R}_t)}{\log \Omega} \quad (4.28)$$

where Ω is the volume (number of sites) inside region \mathcal{R} .

The Legendre transform of the fractal dimensions is the so-called multifractal spectrum. More precisely (see A.2.3), one defines

$$\alpha_q = \frac{d\tau_q}{dq} \quad (4.29)$$

and

$$f(\alpha_q) = q\alpha_q - \tau_q, \quad (4.30)$$

where $\tau_q = (q-1)d_q$. The $f(\alpha)$ spectrum has a straightforward physical meaning: $\Omega^{f(\alpha)}$ is the fraction of sites around which the wavefunction has scaling α . In our case, a trivial (i.e. reduced to a point) multifractal spectrum is the signature of an extended or localized eigenstate², while a non-trivial multifractal spectrum is the signature of a critical eigenstate.

Having recalled these basic definitions, let us now carry out the computation of the fractal dimensions for a state of the SKK form.

In the following, we consider an eigenstate of the form $\psi(m) = C(m) \exp(\kappa h(m))$, on a quasiperiodic tiling that can be any of the examples considered previously: a substitution quasiperiodic chain, the Penrose tiling or the Ammann-Beenker tiling. We are going to prove that this state has a non-trivial multifractal spectrum, and is therefore critical.

We consider the sequence of regions constructed by repetitively applying the tiling inflation rule σ on a initial region \mathcal{R}_0 : $\mathcal{R}_t = \sigma^t \mathcal{R}_0$.

After a few algebraic manipulations of the above definitions, we arrive at

$$d_q(\psi) = \frac{1}{q-1} \lim_{t \rightarrow \infty} \log \left(\frac{Z^{(t)}(2\kappa)^q}{Z^{(t)}(2q\kappa)} \right) / \log Z^{(t)}(0) \quad (4.31)$$

where Z is the partition function already introduced in the specific case of the Fibonacci chain (4.21). Here we have used the important property that the height field is uncorrelated with the local configuration of the atoms.

Furthermore, in all the cases considered here, the partition function has the scaling

$$Z^{(t)}(\beta) \sim \omega^t(\beta). \quad (4.32)$$

Therefore we arrive at the – almost – explicit expression of the fractal dimensions

$$d_q(\psi) = \frac{1}{q-1} \log \left(\frac{\omega(2\kappa)^q}{\omega(2q\kappa)} \right) / \log(\omega(0)). \quad (4.33)$$

For the expression to be fully explicit, we need to compute ω for the specific tiling at hand, as we already did in the Fibonacci case (4.24).

We can also compute the $f(\alpha)$ spectrum. Letting $x = 2\kappa$, we have

$$\alpha_q = \log(\omega(x)) - x \frac{\omega'(qx)}{\omega(qx)} \quad (4.34)$$

2. One can indeed show that for a localized state, the multifractal spectrum is the point $(\alpha, f(\alpha)) = (0, 0)$ while for an extended state, the spectrum is the point $(\alpha, f(\alpha)) = (1, 1)$.

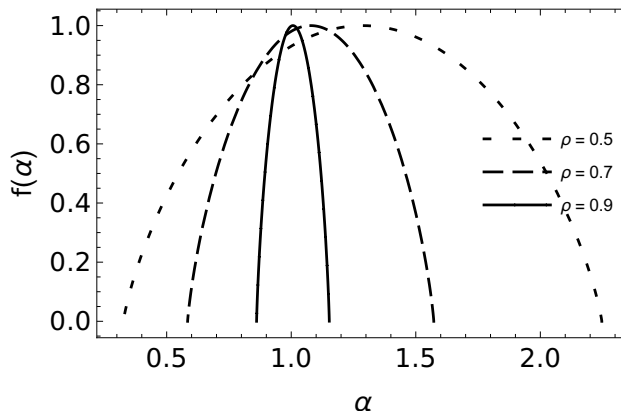


Figure 4.4. – The multifractal spectrum of the central state of the Fibonacci chain, for different value of the coupling ratio ρ .

and

$$f(\alpha_q) = \log(\omega(qx)) - qx \frac{\omega'(qx)}{\omega(qx)} \quad (4.35)$$

Remark that whenever the function ω is such that

$$\omega(x) = e^{Ax} \omega(-x), \quad (4.36)$$

the function $f(\alpha)$ is symmetric around its maximum. One can easily prove that the above condition (4.36) is equivalent to having a height distribution which is asymptotically symmetric around its maximum. One can moreover express the maximum h_M in terms of A : $h_M(t) = At/2$

4.2.2. The fractal dimensions of the $E = 0$ state of the Fibonacci chain

Figure (4.4) shows the multifractal spectrum of the central state of the Fibonacci chain, for different values of the ratio of the couplings, ρ . The spectrum is clearly multifractal (not reduced to a single point), meaning that the $E = 0$ state is critical, as we expected. Note that as $\rho \rightarrow 1$, the support of the spectrum becomes narrower, meaning that the state approaches the limiting Bloch wave form in the periodic limit. We also remark that the multifractal spectra are symmetric around their maximum, which is, as explained in the previous section, a consequence of the shape of the height distribution, which is symmetric around its maximum (here the maximum is reached at $h_M = 0$). The symmetry of the $f(\alpha)$ spectrum, explicitly, is

$$\alpha_q + \alpha_{-q} = 2\alpha_{q=0} \quad (4.37)$$

This relation is distinct from the symmetry relation obeyed by the multifractal spectrum of a disordered system at the Anderson transition [Rodriguez et al. \[2009\]](#): in the present case, the symmetry relates q to $-q$, whereas the symmetry at the Anderson transition connects q to $1 - q$. However, in both cases, the scaling of the *small wavefunction components* (given by $q \rightarrow \infty$) is related to the scaling of the *large wavefunction components* (given by $q \rightarrow -\infty$). As we remarked earlier, under the substitution S' (4.13) the heights on the “old” sites m change sign, and $\psi(m)$ is transformed to $\psi(m)^{-1}$. In other words large components are transformed to small components and vice-versa.

4.3. Transmission coefficient on the Fibonacci chain

We now present some results for the transmission coefficient, as an example of the special properties of these critical states. Consider an approximant of the Fibonacci chain consisting of

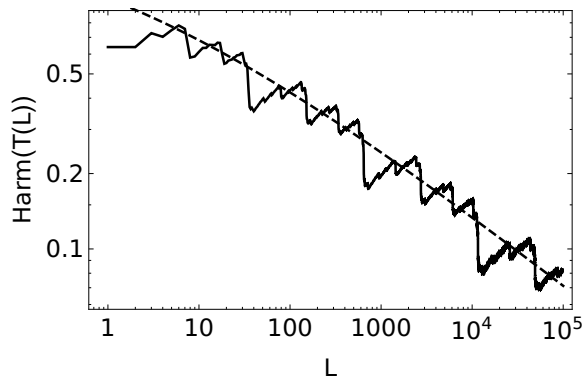


Figure 4.5. – Mean (harmonic) transmission of a finite-size piece of length L of the Fibonacci chain. Dashed line: analytical prediction (4.41), continuous line: numerical calculation (average was performed on subchains of a system of $F_{27} = 196418$ atoms).

$2n$ atoms, attached to translationally invariant left and right leads. The transmission coefficient is the fraction of the incident electronic probability that goes through the system. Creating a plane wave at energy $E = 0$ (i.e. of wavevector $k = \pm\pi/2$) on the periodic lead excites the $E = 0$ state of the chain. The transmission coefficient T_n is then [Beenakker \[1997\]](#):

$$T_n = \frac{4}{\left(x_n + \frac{1}{x_n}\right)^2} \quad (4.38)$$

with $x_n = |\psi(2n)/\psi(0)|$. Note that according to the Landauer formula, this transmission coefficient is proportional to the zero-temperature dc conductance of the system at Fermi energy $E = 0$ [Economou and Soukoulis \[1981\]](#).

Exploiting the SKK form of the $E = 0$ state, $|\psi(2n)| = e^{\kappa h(n)}$, the transmission can be recast as

$$T_n = \frac{1}{\cosh^2[\kappa(h(n) - h(0))]}, \quad (4.39)$$

so that the transmission between two sites depends only on the height difference of these two sites. The transmission is maximal when the height difference is zero, in other words, *one can have perfect transmission between two sites of the chain which are arbitrarily far apart.*

Another useful quantity which is easy to compute is the harmonic mean of T defined by

$$\langle T \rangle(L) = \left(\frac{1}{L} \sum_{m \leq L} \frac{1}{T_m} \right)^{-1} \quad (4.40)$$

To estimate the typical transmission, the harmonic mean is preferred over the arithmetic mean in cases when the distribution is very wide leading to domination of the latter by rare events. This was pointed out for random systems [Economou and Soukoulis \[1981\]](#), where it is the logarithm of T which is distributed normally. Here too, the distribution of $\log T$ is expected to be Gaussian, as can be inferred from Eq. (4.40). The scaling of $\langle T \rangle(L)$ with system size can be calculated using the properties of the distribution of heights. The mean transmission of this chain after t inflations is given by

$$\langle T \rangle(L) \sim 2 \left(1 + (L/L_0)^{\log \frac{\omega(2\kappa)}{\omega(0)} / \log \tau^6} \right)^{-1} \quad (4.41)$$

Since $\omega(\kappa) \geq \omega(0)$, the mean transmission goes to zero at large distance as a power law, in good accord with numerical data as seen in (4.5). Remark that the analytical calculation is performed

for chains of even length, i.e., every third approximant of the Fibonacci series, whose lengths are given by $L_t = F_{3t} \sim \tau^{3t}$. This explains why our analytical calculation only captures the overall power-law behavior of the transmission, but not the superimposed log-periodic oscillations observed in the numerical study, which was carried out for all lengths L (Fig. (4.5)). It may be interesting to study these oscillations with an analysis along the lines of [Dumont and Thomas \[1991\]](#). More generally, log-periodic modulations are frequently observed in systems presenting a discrete scale invariance property: see appendix A.5 for a more detailed discussion.

4.4. SKK states on other aperiodic chains

One may ask to what extent the results of the preceding section are generically true for other aperiodic chains, quasiperiodic or not.

4.4.1. SKK states on chains of the metallic mean series

To investigate this question, we consider models on a series of quasiperiodic chains: the so-called metallic mean substitutions (based on the golden mean τ and its generalizations to silver, bronze, ... irrationals) [Thiem and Schreiber \[2011\]](#). They are generalization of the Fibonacci substitution:

$$S_n : \begin{cases} A \rightarrow A^n B \\ B \rightarrow A, \end{cases} \quad (4.42)$$

where A^n is a shorthand notation for A repeated n times. $n = 1$ yields the Fibonacci chain, $n = 2$ the silver-mean chain, $n = 3$ the bronze-mean chain, ...

In this case, it is easy to show by direct inspection of the inflation rule for the arrows that the evolution of the height statistics still obeys the Fokker-Planck-like equation (4.17). Thus, the same conclusions hold as in the Fibonacci case: the partition function has the scaling behavior

$$Z_\mu^{(2t)}(\beta) \underset{t \rightarrow \infty}{\sim} \omega_n(\beta)^t f_\mu(\beta), \quad (4.43)$$

the height distribution converges to a normal distribution, and the central state is multifractal with the fractal dimensions

$$d_q(\kappa, n) = \frac{1}{q-1} \log \left(\frac{\omega_n(2\kappa)^q}{\omega_n(2\kappa q)} \right) / \log(\omega_n(0)) \quad (4.44)$$

For n even, $n = 2k$, we can compute the ω function explicitly:

$$\omega_{2k}(\beta) = \frac{2e^\beta + k^2(1 + e^\beta)^2 + k(1 + e^\beta)\sqrt{4e^\beta + k^2(1 + e^\beta)^2}}{2e^\beta}, \quad (4.45)$$

and thus find the explicit expression of the fractal dimensions of all the central states in the series $n = 2k$. For n odd, the substitution rule for the arrows is more involved and we were not able to compute explicitly the ω function.

Going back to the even case, one can readily check that, as n grows, the central state behaves more and more like an extended state: $d_q(\kappa, n \rightarrow \infty) = 1$. This is to be expected since the aperiodic chain locally looks more and more periodic as n grows. Figure (4.6) shows the multifractal spectrum for different values of k . We see that the support of the spectrum decreases as k is increased, which is yet another signature that the state becomes less critical as k is increased.

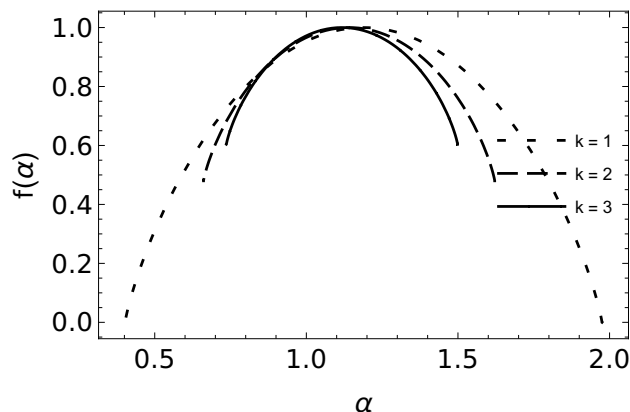


Figure 4.6. – The multifractal spectrum of the central state of three metallic mean chains ($k = 1, 2, 3$), for $\rho = 1/2$.

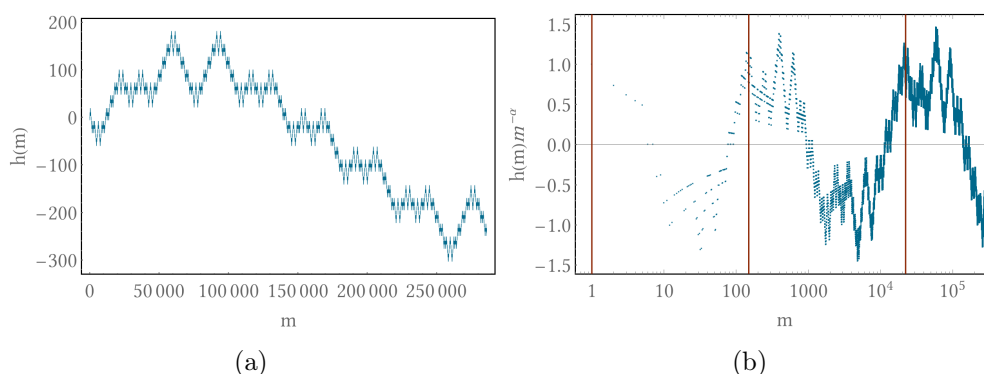


Figure 4.7. – (a): The field of heights for the aperiodic and non-quasiperiodic b3 substitution. The central state is localized, like in the case of a random chain, although this chain is deterministic. (b): The C part of the height function (see Eq. (4.48)), in log-linear scale. Periods of the function are marked by red vertical lines. As m becomes larger, the function C is sampled more and more precisely, and its continuous, nowhere differentiable character becomes apparent.

4.4.2. Absence of SKK state on the b3 non-Pisot substitution

To conclude this section, we consider an aperiodic substitution which is *not* quasiperiodic:

$$S : \begin{cases} A \rightarrow AB BB \\ B \rightarrow A, \end{cases} \quad (4.46)$$

This substitution, which we will call the *b3 substitution*, is aperiodic – but not quasiperiodic. Indeed, as the eigenvalues of the substitution matrix do not satisfy the Pisot condition³, hence the structure does not have Bragg peaks in its diffraction spectrum [Godrèche and Luck \[1992\]](#). The b3 substitution has been thoroughly studied from the geometrical point of view, see e.g. [Frank and Robinson \[2008\]](#).

One can show that under the b3 substitution, the heights are multiplied by 3, along with a sign change, giving:

$$\mathbf{N}^{(t+1)}(-3h) = \sum_{h'=-3}^3 M(h') \mathbf{N}^{(t)}(h-h') \quad (4.47)$$

3. To be Pisot, only one of the eigenvalues can be greater than 1 in absolute value.

This equation implies that the height on this tiling (Fig. (4.7a)) grows much faster than in the quasiperiodic case: in particular, the maximum of the height grows as a power law $h_{\max}(L) = \max_{i \leq L} h(i) \sim L^\alpha$, whereas in the quasiperiodic case it grows much slower – logarithmically. The power-law exponent can be computed explicitly: $\alpha = \log 3 / \log \omega_{b3}^3$, where $\omega_{b3} = (1 + \sqrt{13})/2$ is the largest eigenvalue of the b3 inflation matrix. Since $h_{\max}(L)$ behaves as a power-law, we can expect the typical height $h_{\text{typ}}(L)$ to also behave as a power-law. Indeed, using the result of Dumont [1990], one can compute that

$$h(m) = C \left(\frac{\log m}{\log \omega_{b3}^6} \right) m^\alpha + o(m^\alpha), \quad (4.48)$$

where C is a continuous, nowhere differentiable function of period one, responsible for log-periodic oscillations in $h(m)$, as can be seen on Fig. (4.7b). Eq. (4.48) implies that the $E = 0$ state on the b3 chain has a stretched exponential form – with bounded log-periodic modulations, and is therefore localized, as in the random case Soukoulis and Economou [1981].

4.5. Discussion and conclusions for 1D chains

Having described these properties of the central states in 1D quasiperiodic models, we now address the question of the ground state in these models. We now explain why it is not expected to have the SKK form, as mentioned earlier. The ground state is known to be multifractal like the other states, as has been discussed in Chap. 2.7. However, the following argument indicates that it should not be factorizable into a local part and an exponential height-dependent part. For, on the one hand, since the ground state is non-degenerate, the arrow field used in construction of the SKK ansatz must respect the symmetry of the chain (in contrast to the arrow field (4.8) which depends not only on the local environment but *also on the parity* of the site). On the other hand, in the case of the metallic mean chains, any such arrow field will yield a height function which either i) grows linearly with distance (corresponding to an evanescent wave) or ii) depends on the local environment only (corresponding to an extended state)⁴.

This argument is confirmed by an explicit calculation in Sec. 4.7, where we compute the form of the ground state in perturbation theory. Specifically, we compute the spatial dependence of the prefactor term and show that it is non-local, contrarily to the ansatz.

To conclude, we have seen that the central state of a tight-binding Hamiltonian on aperiodic chains can be described in terms of a height field, which is the integral of a field of arrows drawn on the chain. The structure of the central state (as read from its fractal dimensions) is directly related to the geometrical properties of the height field. In the metallic mean case, the height field grows slowly with the distance $h(L) \sim \sqrt{\log L}$, which results in the state being critical. We believe that this behavior is likely to generalize to canonical cut-and-project chains, of which the metallic mean chains are particular cases. Next we considered an aperiodic chain which is *not* quasiperiodic, the b3 chain, whose behavior is seen to be radically different. The typical height now grows much faster, $h(L) \sim L^\alpha$, and this results in the central state being localized. Note that, although this state has the same scaling characteristics as that on the random chain, this chain is purely deterministic.

4.6. SKK states on 2D tilings and their properties

This section deals with the extension of the preceding calculations to two dimensional models. We will focus on the two most studied tilings: the Penrose rhombus tiling and the Ammann-

4. This is related to the fact that puncturing a two-dimensional torus in one point does not affect its first cohomology group, see also Kalugin and Katz [2014].

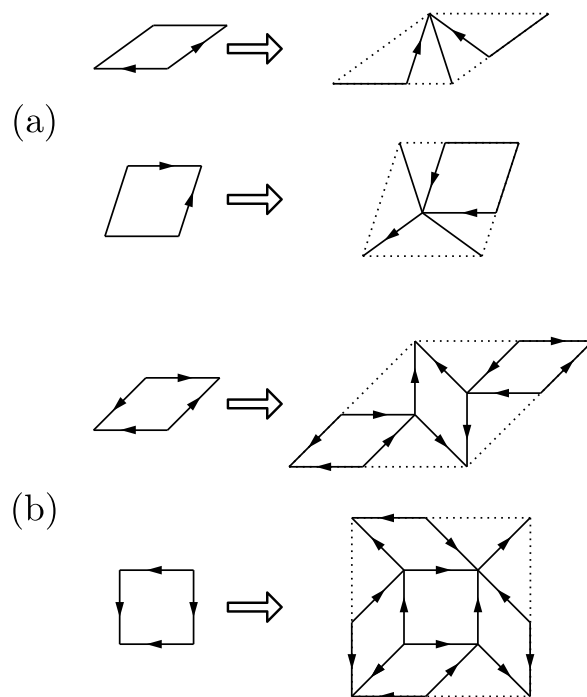


Figure 4.8. – Tile substitution rules and some of the arrow decorations corresponding to matching rules (see text) for (a) Penrose tiling and (b) Ammann-Beenker tiling

Beenker tiling.

Both tilings are built using two tiles: these are the fat and thin rhombuses in the case of the Penrose tiling, and the square and 45° rhombus for the Ammann-Beenker tiling. These tilings can be constructed by successive transformation of the two tiles using well-known substitution rules, as shown in Fig. (4.8). It is known, moreover, that substitution tilings possess matching rules [Goodman-Strauss \[1998\]](#) which allow to distinguish “allowed” from “forbidden” configurations of adjacent tiles [Baake and Grimm \[2013\]](#). In the case of Penrose and Ammann-Beenker tilings, the matching rules can be implemented by decorating the tiles and by requiring that the decorations on adjacent tiles match. These decorations consist in adding arrows to the tile edges (in the case of Ammann-Beenker tiling additional decorations of vertices is also needed to enforce the eight-fold rotational symmetry). It turns out, interestingly, that a subset of these decorations can be used in the construction of SKK states on these two tilings. Fig. (4.8) shows the arrows which will enter in the construction of the SKK ground state. They are illustrated for the two basic tiles and their inflations on the two tilings we consider here.

As can be checked by inspection, these arrows form an irrotational field. This implies that they can be written as a gradient of a scalar function, the height function $h(m)$, taken up in Sec. 4.1.3. As in the case of 1D chains, the height functions will enter in the construction of SKK states on 2D tilings.

4.6.1. Tight-binding models on 2D tilings

We can now ask the question whether tight-binding models for electrons hopping along edges of these 2D tilings admit eigenstates which can be defined in terms of the arrow field.

[Sutherland \[1986\]](#) was the first to answer positively to this question, furnishing a tight-binding Hamiltonian in which on-site potentials are tuned to have specific values, so that its ground state is given by $\psi(m) = \exp(\kappa h(m))$, where κ is a constant. Note that this expression is not yet the form Eq. (4.2)), as it lacks the pre-exponential factor. Similar eigenstates have been found by

other authors for more complicated Hamiltonians Tokihiro et al. [1988], Repetowicz et al. [1998]. In those works, a functional form is proposed, and used to reverse engineer the Hamiltonian for which it is an eigenstate. These Sutherland-type solutions correspond to artificially “fine-tuned” Hamiltonians and do not apply in the standard tight-binding case (4.1). The solution for the ground state of the pure hopping Hamiltonian proposed by Kalugin and Katz [2014] was thus an important advance.

Here we consider quasiperiodic tight-binding Hamiltonians in 2D with off-diagonal as well as diagonal (onsite) terms, given by

$$\hat{H}(t, V) = -t \sum_{\langle m, n \rangle} |n\rangle \langle m| + \text{H.c.} + V \sum_m z_m |m\rangle \langle m|, \quad (4.49)$$

where z_m is the coordination of site m , and where the hopping occurs between nearest neighbor sites. The parameter V allows to go continuously from the pure hopping model ($V = 0$) to the discrete Laplacian model ($V = t$) and eventually to the limit of decoupled atoms ($V/t \rightarrow \infty$). We will show that the ground state has the SKK form for any choice of V , namely:

$$\psi_{\text{GS}}(m) = C(m)e^{\kappa h(m)}, \quad (4.50)$$

where $h(m)$ is a height field defined on the vertices of the tiling, and κ is a constant. The pre-exponential factor $C(m)$ is, as we stated in the introduction, a quasiperiodic function which depends on the local environment of the site m . In Subsec. 4.6.5 we examine Hamiltonians with other types of on-site terms V_m , and show that the SKK form of the ground state persists in these cases.

This form of the wave function allows to compute exactly, as in 1D, the multifractal spectrum of the ground state of this family of models. To do this, it is necessary to know the properties of the height field, studied in the next section.

4.6.2. Properties of the 2D height field. Fractal dimensions of the ground state.

As for the one dimensional case, the height on a given site is the integral of an arrow field. The arrows correspond to decorations of edges of the basic tiles, as illustrated in Fig. (4.8) for the Penrose and Ammann-Beenker tilings. Fig. (4.8) also indicates how the distribution of heights evolves under inflation. By repeated inflations, one thus generates the set of height fields for larger and larger pieces of tiling.

To understand the spatial dependence of the height field, it is instructive to start by examining the variations of $h(m)$ along some specific directions in the tiling. Fig. (4.9a) shows the height field along the slice of the Ammann-Beenker tiling shown in blue in figure (4.9b). The similitude of behavior with the 1D height function of the Fibonacci chain (Fig. (4.3)) is evident. Let us now explain the reasons for this similarity.

Consider a line which runs parallel to one of the eight possible orientations of the edges (in our figures these occur at angles which are multiples of $\pi/4$). In Fig. (4.9b) the blue line is shown as an example. The distance between a pair of nodes along such a line is $nl' + mL'$, where l' and L' are respectively the length of an edge and of the diagonal of a square, and where n and m are integers. Upon substitution (4.8), the lengths are transformed according to $l' \rightarrow l' + L'$, $L' \rightarrow l' + L' + l'$. The lengths $A = l' + L'$ and $B = L'$ are transformed according to the silver mean substitution: $A \rightarrow A + A + B$ and $B \rightarrow A$. Reasoning along the same lines as in Sec. 4.1.4, the heights along any such line oriented at angles $n\pi/4$ also transform according to the silver mean substitution, meaning that the height plot along such a line (Fig. (4.9a)) should have the same structure as in the 1D case.

On the tiling, there are also paths along which the height is constant, as illustrated by the orange line shown on figure (4.9b), corresponding to directions lying in-between the axes of the

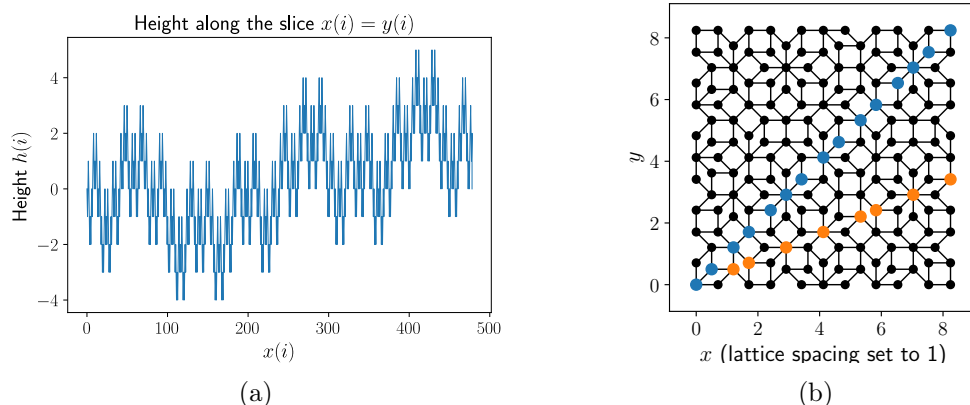


Figure 4.9. – (a): The height field along a slice of the Ammann-Beenker tiling. (b): In blue, the slice taken in (a), and in orange another slice, along which the height is constant.

edges (in our figures these occur at angles $(n + 1/2)\pi/4$). For the orange path, the distance between two nodes is of the form $nl + mL$, where l and L are respectively the length of the small and large diagonals of lozenges. Therefore, any two nodes along such a line are connected by a path going only through large and small diagonals of lozenges, a path along which, as can be seen from Fig. (4.8), the height is a constant. This implies that the exponential factor of the wavefunction remains constant along these paths and any variations are due only to the prefactor C . If one looks at the variation of the SKK eigenstate along such a path, the state will appear to be extended, with no evidence of fractality.

As in 1D, the scale invariance of the height field implies multifractality of the corresponding SKK state. We present now the results for the statistics of the heights.

Height distribution

Just like in the 1D case (see Sec. 4.1.4), we compute the distribution of heights $N^{(t)}(h)$ on an asymptotically large region \mathcal{R}_t : $\mathcal{R}_t = S^t \mathcal{R}_0$ with $t \rightarrow \infty$. For Penrose tiling, this distribution was first calculated by Sutherland in the saddle-point approximation in Sutherland [1986], while the exact results were later obtained in Repetowicz et al. [1998]. We present here the detailed computation for the case of Ammann-Beenker tiling.

The Ammann-Beenker tiling can be built using a substitution rule (see Fig. (4.10)) which acts on the two tiles (lozenge and square). Let $\mathbf{v} = (N_L, N_S)$ be a vector whose entries are respectively the number of lozenge and square tiles in a given region \mathcal{R}_0 . Then the number of tiles in the inflated region $\mathcal{R}_1 = S \mathcal{R}_0$ is given by $M\mathbf{v}$ where M is the *inflation matrix*

$$M = \begin{bmatrix} 3 & 4 \\ 2 & 3 \end{bmatrix}, \quad (4.51)$$

already introduced in Chap. 1.

As in 1D, we now make use of the substitution to compute the distribution of heights. Following Sutherland [1986], we associate to each tile the height on one of its four vertices, taken as reference. Here we choose the reference vertex to be the one which has arrows pointing in (see Fig. (4.10)). We now compute $N_\mu^{(t)}(h)$, the number of times height h is reached on the reference site of the tiles of type $\mu = L, S$. As in 1D, the substitution reverses the effective arrows on the supertiles (see Fig. (4.10)), meaning that height changes sign on the reference sites of the supertiles after

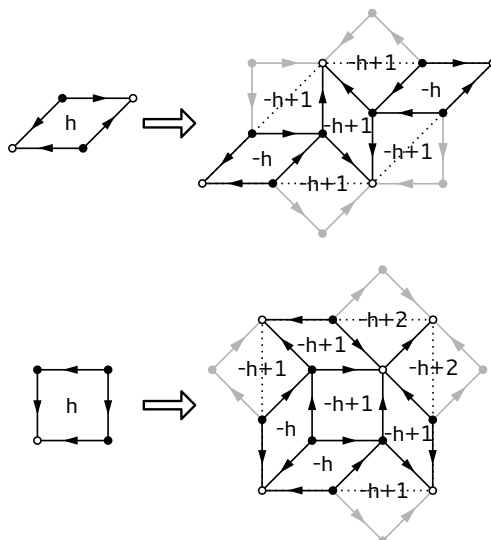


Figure 4.10. – The two tiles of the Ammann-Beenker tiling, and the supertiles obtained upon substitution. Reference vertices (see text for details) are marked by open circles. The height associated to each tile, i.e. the height on its reference site, is marked inside the tile.

a substitution. As will be checked a posteriori, the heights are distributed in an *environment-independent fashion*, meaning the arbitrariness in the choice of reference sites does not affect the result of the computation. Introducing the vector $\mathbf{N}^{(t)}(h) = (N_L^{(t)}(h), N_S^{(t)}(h))$, one has

$$\mathbf{N}^{(t+1)}(-h) = \sum_{h'=0}^2 M(h') \mathbf{N}^{(t)}(h - h'), \quad (4.52)$$

where the *generalized inflation matrices* are given by

$$M(0) = \begin{bmatrix} 2 & 2 \\ 0 & 0 \end{bmatrix}, \quad (4.53)$$

$$M(1) = \begin{bmatrix} 1 & 2 \\ 2 & 2 \end{bmatrix}, \quad (4.54)$$

$$M(2) = \begin{bmatrix} 0 & 0 \\ 0 & 1 \end{bmatrix}. \quad (4.55)$$

Note that the sum of the generalized inflation matrices, $M = \sum M(h')$, is just the inflation matrix M of eq. (4.51). As 1D, the equation (4.52) is a Fokker-Planck-like equation, and we expect the environment-specific height distributions to converge to Gaussian distributions in the large time limit. Introducing partition function $Z_\mu^{(t)}(\beta) = \sum_h N_\mu^{(t)}(h) \exp(\beta h)$, the evolution equation (4.52) is recast to

$$\mathbf{Z}^{(t+2)}(\beta) = \tilde{M}(-\beta) \tilde{M}(\beta) \mathbf{Z}^{(t)}(\beta) \quad (4.56)$$

where $\tilde{M}(\beta) = \sum_h M(h) \exp(-\beta h)$. From this recursion relation, and since all the coefficients of \tilde{M} are strictly positive, the Perron–Frobenius theorem applies, we deduce that the large time behavior of the partition function must be of the form

$$Z_\mu^{(2t)}(\beta) \underset{t \rightarrow \infty}{\sim} \omega^t(\beta) f_\mu(\beta) \quad (4.57)$$

where $\omega(\beta)$ is the largest eigenvalue of $\tilde{M}(-\beta)\tilde{M}(\beta)$, and $f_\mu(\beta)$ is the associated eigenvector. Explicit calculation gives

$$\omega(\beta) = \frac{a(\beta) + \sqrt{a(\beta)^2 - e^{2\beta}}}{e^\beta} \quad (4.58)$$

with $a(\beta) = 4 \exp(2\beta) + 9 \exp(\beta) + 4$. Thus, in the $t \rightarrow \infty$ limit, the distributions all converge to the Gaussian distribution:

$$P_\mu^{(t)}(h) \sim \frac{f_\mu}{\sqrt{4\pi Dt}} \exp\left(-\frac{h^2}{4Dt}\right) \quad (4.59)$$

where D is given by

$$D = \frac{1}{6\sqrt{2}}. \quad (4.60)$$

To obtain the fractal dimensions of the Penrose SKK eigenstate we need a formula for $\omega(\beta)$, which was not explicitly calculated in Sutherland [1986], Repetowicz et al. [1998]. We give this formula without derivation since the computation is along the same line as in the Ammann-Beenker case and most of it was already done by Repetowicz et al. [1998]:

$$\omega(\beta) = \frac{b(\beta) + \sqrt{b(\beta)^2 - 4e^{2\beta}}}{2} \quad (4.61)$$

with $b(\beta) = \exp(2\beta) + 5 \exp(\beta) + 1$.

To conclude, the 2D height fields examined here have exactly the same properties as the 1D ones (see 4.1.4). Namely : the height grows slowly – $h(L) \sim \sqrt{\log L}$, and the height distribution on a large tiling piece is Gaussian. Moreover, the ω function – which governs the large-scale behavior of the partition function – can be computed exactly.

Height field and multifractality of the SKK states

As in the 1D case (see 4.2), this ω function determines the multifractal spectrum an SKK state ψ through the equations:

$$\alpha_q = \log(\omega(2q\kappa)) - 2q\kappa \frac{\omega'(2q\kappa)}{\omega(2q\kappa)} \quad (4.62)$$

and

$$f(\alpha_q) = \log(\omega(2q\kappa)) - 2q\kappa \frac{\omega'(2q\kappa)}{\omega(2q\kappa)}. \quad (4.63)$$

These theoretical predictions will be compared with results from numerical computations, as described in the next subsections.

4.6.3. Results for the AB tiling

The tight-binding matrix was diagonalized numerically for a fixed value of the onsite potential V and for a range of system sizes. In numerical computations, it is rather common to consider “canonical approximants”: periodic tilings with arbitrarily large unit cells approximating the quasiperiodic tiling (see Subsec. 2.3.1 for a discussion on 1D approximants, and Duneau et al. [1989] for the case of the canonical approximants to the Ammann-Beenker tiling). However on these canonical approximants, the height field is not single-valued. We therefore use the modified approximants – with mirror boundary conditions instead of periodic boundary conditions – proposed by Kalugin and Katz [2014], which do not have this drawback. We shall label approximants of increasing size with an integer, l , which is equal to the number of inflations (4.8) performed to build it. Using these approximants, the values of the constant κ and the pre-exponential factors of the expression Eq. (4.2) can then be determined.

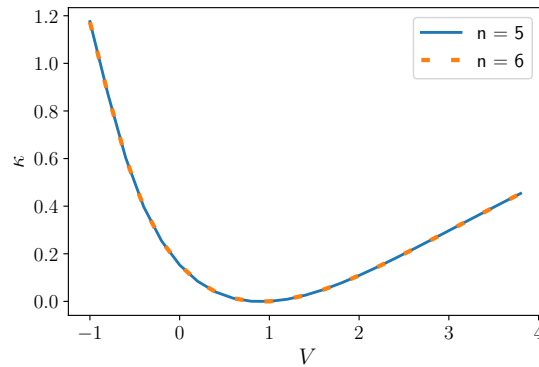


Figure 4.11. – Plot of κ versus V for the ground state of the Ammann-Beenker tiling computed by numerical diagonalization for approximants $l = 5$ and 6 (respectively 4180 and 23950 sites).

The constant κ

The first step of the analysis consists of determining the unknown constant κ in the expression for the ground state ψ_{GS} from the numerical solution of ψ . This is done by the method used by Kalugin and Katz [2014], which relies on the following observation: if two sites m_1, m_2 of the approximant have nearly identical local environments, then their wavefunction amplitudes will have almost identical prefactors. The ratio of eigenstate amplitudes on these two sites is then

$$\frac{\psi_{\text{GS}}(m_1)}{\psi_{\text{GS}}(m_2)} = \frac{C(m_1)}{C(m_2)} e^{\kappa(h(m_1)-h(m_2))} \simeq e^{\kappa(h(m_1)-h(m_2))} \quad (4.64)$$

This relation allows us to calculate a value of κ from the numerical solution, since the height field is known exactly for the approximant. One expects this value to become progressively more accurate as larger and larger approximants are considered, since the numerical solution approaches the exact one, and since one can find sites m_1 and m_2 whose environments are similar out to a greater distance. As can be seen in Tab. (4.1), the κ -value determined in this fashion indeed converges.

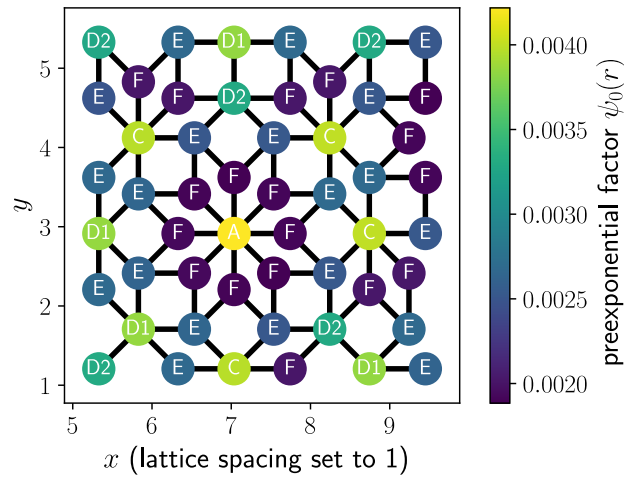
	Penrose tiling		
N	9045	23490	61191
κ	0.02125888	0.02163468	0.02148895
	Ammann-Beenker tiling		
N	4180	23950	138601
κ	0.61215	0.61252	0.61249

Table 4.1. – κ for different values of N (the number of sites) in Penrose and Ammann-Beenker approximants for $V = -0.5$

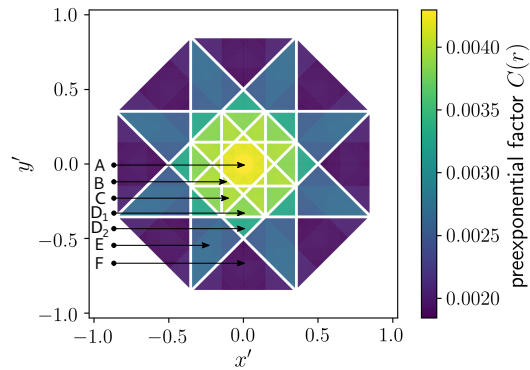
Figure (4.11) shows the evolution of κ when the strength of the on-site potential, V , is varied in the model. The shift of the two curves in going from the $l = 5$ to $l = 6$ approximant is too small to be visible on the graph, indicating that the results are converged.

The prefactors C

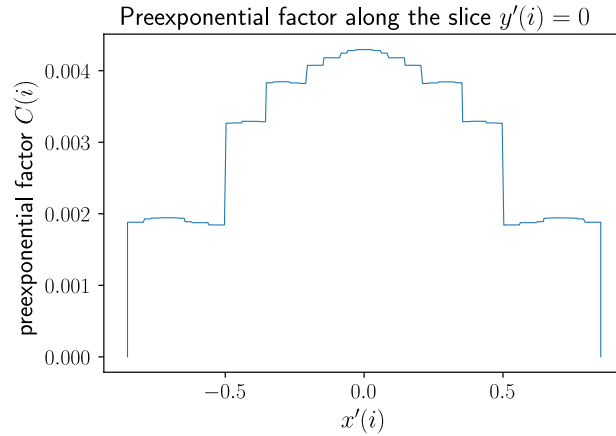
The second step of the analysis consists of determining the set of prefactors $C(m)$ by plugging in the value of κ already found. Once these have been determined, we need to check whether



(a)



(b)



(c)

Figure 4.12. – (a): The numerically computed prefactors on a small patch of the approximant $l = 7$ (138601 atoms). (b): The numerically computed prefactor in perpendicular space (x' and y' denote the perpendicular horizontal and vertical coordinates), for approximant $l = 7$. White lines outline the zones corresponding to different first neighbor environments. (c): “Wedding cake” plot showing the variation of the prefactor along a horizontal cut passing through the origin in perpendicular space.

$C(m)$ is local: that is, dependent only on the local arrangement of atoms. A first indication that this is indeed the case is provided by Fig. (4.12a), which shows the numerically computed prefactors in a small region of the Ammann-Beenker tiling. The colors reflect the wavefunction amplitudes computed for the pure hopping Hamiltonian ($V = 0$), and sites have been labeled by A, B, C, D₁, D₂, E and F, to indicate the seven different nearest neighbor configurations on this tiling. A represents sites with 8 neighbors, B represents sites with 7 neighbors, and so on. The subscripts allow to differentiate between sites of the same coordination number (5), but which transform differently under substitutions. Upon inspection of the figure, the colors and labels are seen to correlate, providing a visual check that the pre-exponential factor depends primarily on the local arrangement of the atoms.

A more quantitative demonstration of the local character of the $C(m)$ consists of plotting them in the perpendicular (or internal) space representation of the tiling. This representation allows to classify sites according to their environments on the tiling. As detailed explanations can be found in the literature, it suffices here to give the general idea. Recall that the Ammann-Beenker tiling, as many other quasiperiodic tilings, can be constructed from a periodic tiling in higher dimension : the so-called cut-and-project construction method (see Sec. 1.2.2 for a general introduction, and Duneau et al. [1989] for a description in the particular case of the Ammann-Beenker tiling). In the case of the Ammann-Beenker tiling, the higher-dimensional space is 4 dimensional, and decomposes into the 2D physical plane, and the 2D orthogonal plane called the *perpendicular (or internal) space*. The closer the projections of two vertices are in internal space the more similar their local environments in physical space⁵. Internal space representation is thus well-suited to check the local character of the pre-exponential factor, as was already pointed out by Kalugin and Katz [2014].

Fig. (4.12b) shows the $C(m)$ represented by a colorscale in perpendicular space. The seven families of nearest neighbor configurations A, B, ... correspond to seven nonoverlapping domains as shown by the labels in the Fig. (4.12b). The colors and the domain labels are seen to be in good correspondence, showing thereby that the prefactors are determined by the local environment.

Within each family of environments, one can distinguish subfamilies according to the next nearest neighbor configurations. These in turn can be subdivided and so on. The prefactors $C(m)$, in consequence, exhibit a fine structure due to these differences of environments at the level of n th near-neighbors. This can be seen in Fig. (4.12c), which shows the variation of the prefactor along a horizontal cut passing through the origin in internal space.

Multifractal spectra

Fig. (4.13) shows the multifractal spectrum, $f(\alpha)$, of the ground state calculated numerically for $\kappa(V = -0.5) \simeq 0.5$, on the Ammann-Beenker tiling. Dots indicate the numerical values obtained from system-size scaling (see e.g. Thiem and Schreiber [2011] for a description of the method) for approximants up to $l = 7$ (138601 atoms). One can see that the theoretical prediction and the numerical computations are in perfect agreement, showing that Eq. (4.62) correctly captures the multifractal properties of the ground state on the Ammann-Beenker tiling, for the family of models (4.49).

The multifractality of a wavefunction can be measured by the width (or support) of the bell-shaped curve (see Fig. (4.13)) formed by its multifractal spectrum:

$$\Delta_f = \lim_{q \rightarrow \infty} (\alpha_{-q} - \alpha_q) \quad (4.65)$$

5. More precisely, for any point p and for any distance r , there is a $\epsilon(p, r) > 0$ such that any point closer than $\epsilon(p, r)$ from p in internal space has a local environment that matches the one of p up to distance r in physical space.

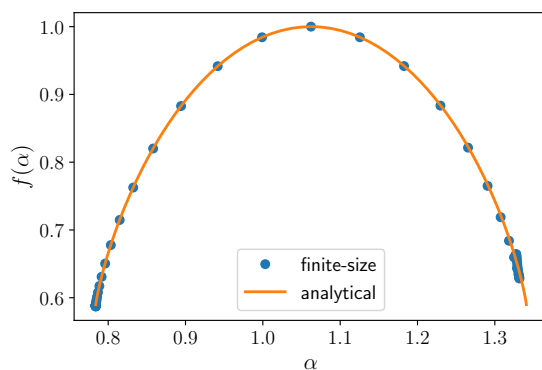


Figure 4.13. – Dots: The numerically computed $f(\alpha)$ of the GS on the Ammann-Beenker tiling ($V = -0.5$). Solid line: the analytical solution (4.62), using the numerically determined κ (see text).

For the SKK states on the Penrose and Ammann-Beenker tilings we find

$$\Delta_f(\kappa) = \frac{4|\kappa|}{\log \omega(0)}. \quad (4.66)$$

Interestingly, this expression is valid not only for the Penrose and Ammann-Beenker but also for the Fibonacci chain, and for every chain of the metallic mean series, with n even (see Sec. 2). For the metallic mean with $n = 3$ however, the expression is different. To our knowledge, there is no explanation for the surprising universality of the support of the multifractal spectrum of the SKK states. The value of κ , as shown on Fig. (4.11) is proportional to the support of the multifractal spectrum, and thus tells us to which extent the ground state is multifractal. To give a specific example, the figure shows that for $V = 1$, $\kappa = 0$, and the ground state is not multifractal at all – it is extended. This is of course to be expected since for $V = 1$ the model is just the discrete Laplacian, whose ground state is uniform over the tiling. As V is increased or decreased with respect to $V = 1$, κ increases, and the support of the ground state likewise. This state is thus becoming increasingly multifractal.

4.6.4. A variational calculation for the ground state

It is interesting to ask at this point whether an analytical calculation could reproduce, even approximately, the SKK solution just presented. In this subsection, we describe a variational calculation for the ground state on the Ammann-Beenker tiling. This method allows us to obtain an approximate theoretical solution for the ground state wave function and energy, and we will see that the results compare well with the numerical solutions.

Consider a variational ansatz which includes the exponential nonlocal term, and with a truncated set of local environments, namely the seven nearest neighbor environments present on this tiling. This approximation is expected to be reasonable, as can be seen from the numerical results shown in Fig. (4.12). The following form was thus chosen for the variational ansatz:

$$\psi_{\text{var}}(m; C_{\text{var}}, \kappa) = C_{\text{var}}(m) e^{\kappa h(m)} \quad (4.67)$$

where C_{var} is a function that takes seven values according to the seven possible first neighbor configurations of the Ammann-Beenker tiling (see Fig. (4.12a)). The seven values of the function C_{var} and the parameter κ , are determined using a variational approach: C_{var} and κ are chosen

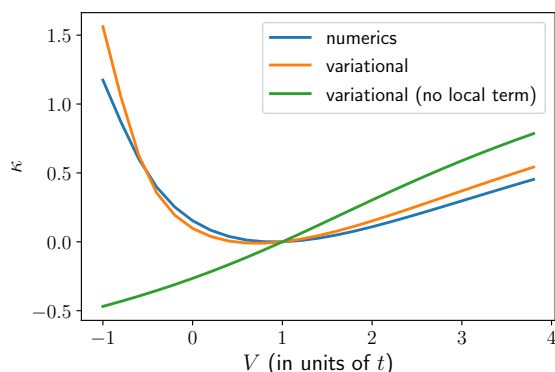


Figure 4.14. $-\kappa$ for the model (4.49). Blue: numerical result. Orange: prediction obtained using the variational method. Green: prediction of the variational method, for a variational state with no local term.

such that the functional

$$E(C_{\text{var}}, \kappa) = \frac{\langle \psi_{\text{var}} | H | \psi_{\text{var}} \rangle}{\langle \psi_{\text{var}} | \psi_{\text{var}} \rangle} \quad (4.68)$$

is minimized. Details of this calculation are given in Appx. E.

	ansatz 1	ansatz 2	ansatz 3	Numerics
$-\mathbf{E}_{\text{GS}}$	4.16143	4.21936	4.22091	4.221697
κ	-0.265337	\emptyset	0.097175	0.153035

Table 4.2. – Predictions for the ground state energy of the pure hopping model by the variational method.

Figure (4.14) shows the value of κ predicted by the variational method, together with its numerically determined value, as a function of the parameter V . To investigate the importance of the two factors entering the variational ansatz Eq. (4.67), we have given in Tab. (4.2) the results for variants as follows: ansatz 1 (all prefactors replaced by a constant), ansatz 2 (exponential terms replaced by a constant) and ansatz 3 (both factors allowed to vary). One sees that the agreement between the variational and the numerical values are quite good for ansatz 3. Increasing the number of environments considered in the variational ansatz would of course improve the quality of the agreement at the price of increasing the number of variables for minimization.

It is interesting to compare the result of the variational method for ansatz 1 in which all prefactors are taken to be equal (the green curve in Figure (4.14)) with the ansatz 3, where prefactors are allowed to vary (the orange curve in Figure (4.14)), and with the numerical results. One can see that, in the absence of the local prefactors, the κ value is not predicted accurately. To conclude, the variational method gives satisfactory values for κ already at first-neighbor level of the approximation. We see that although the local term has no influence on the multifractal spectrum of the state – whose shape is determined by κ alone – it must be included in the expression of the ground state in order to get a good value of κ .

4.6.5. Varying the on-site potential

For the moment, we have only studied the case (4.49) where the on-site potential is proportional to the coordination of the site. Although this choice is “natural” (see e.g. Passaro et al. [1992]), we can wonder whether the SKK nature of the ground state survives when other types of on-site

potentials are used. In this subsection, we study a more general form of Hamiltonian than we have considered so far (Eq. (4.49)).

$$\hat{H} = -t \sum_{\langle m,n \rangle} |n\rangle \langle m| + \text{H.c} + \sum_m V(m) |m\rangle \langle m| \quad (4.69)$$

with different choice of potentials $V(m)$.

SKK ground states for different potentials

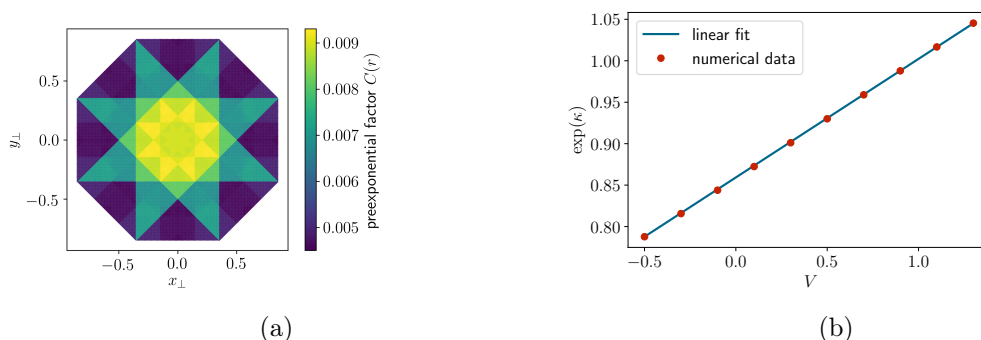


Figure 4.15. – (a): Pre-exponential part of the ground state, for the model described in the text, with $V = 1.3$, computed on the $l = 6$ approximant. (b): $\exp \kappa$ as a function of V for the same model, computed on the same approximant.

Several potentials $V(m)$ preserving the symmetries of the quasicrystals were tested. More specifically, we chose potentials which depend on the first neighbors configuration (see Fig. (4.12b)). In every case we tested, we could check that the ground state was of the SKK type, supporting the following conjecture: *as long as the Hamiltonian has the same symmetry group as the Ammann-Beenker tiling, the ground state is of the SKK type.*

As an example, we consider the case of a potential which is 0 except on sites with 3 neighbors, where it takes the constant value V . As before, we compute the ground state numerically and extract the pre-exponential part. Fig. (4.15a) shows this pre-exponential part. One observes that this figure is very similar to Fig. (4.12). In both cases the pre-exponential factor is approximately constant on nearest neighbors domains, with small variations across different next nearest neighbors domains, and so on. This factor is therefore quasiperiodic (or local), and the ground state is, as claimed, of the SKK type.

Fig. (4.15b) shows how $\exp \kappa$ varies as a function of the potential on the sites with 3 neighbors. One observes that this quantity is well approximated by a line of slope 0.143. Knowing whether $\exp \kappa$ is a linear function of V or not remains an open question. Another interesting feature of this model is the fact that the point $\kappa = 0$ occurs at a non-trivial value of the potential $V^* \simeq 1$. By non-trivial, we mean a value of V which makes the Hamiltonian different from the Laplacian model. Indeed, the ground state of the Laplacian model is uniform and for that model $\kappa = 0$, as we have seen before (see Fig. (4.11)). However, in the non-trivial case at hand, although the ground state has no non-local part (and is therefore extended), it remains non-uniform, and varies quasiperiodically in space. In the Laplacian case, the low energy modes have a large wavelength ($\lambda \propto 1/E$). Here it is not the case: numerical computations show that the ground state at V^* depends strongly on the coordination of the site, and hence has rapid spatial variations. Also in analogy with the Laplacian case, it would be interesting to study the low energy modes: are they also rapidly spatially varying, or do they have a large wavelength like in the Laplacian case? Is there a gap in energy between the ground state and the first excitation, or is there a continuum of

energy like in the Laplacian case? These questions remain open for further study. We shall find similar non-trivial states, for which the same questions can be asked, in the Penrose case (4.17c).

A non-SKK ground state

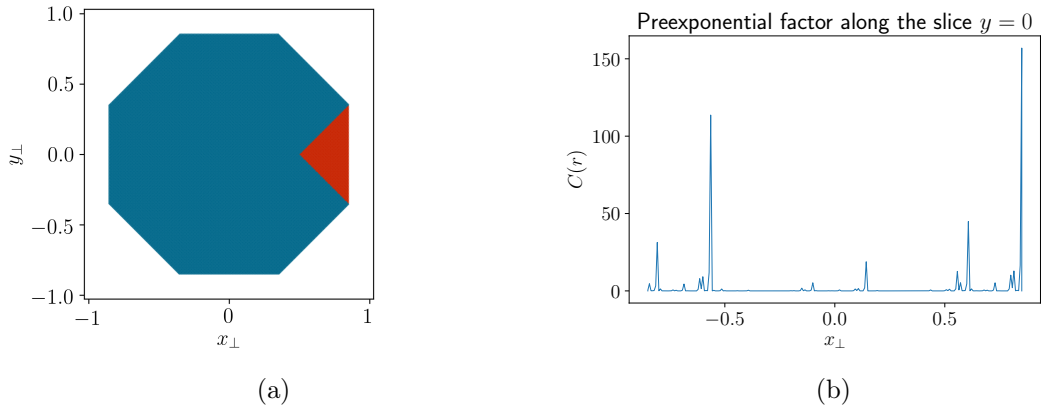


Figure 4.16. – (a): The asymmetric potential described in the text, in perpendicular space. In blue: points where the potential is 0, in red: points where it is non-zero. (b): The prefactor in perpendicular space, computed on a 47321 sites approximant.

As argued in Kalugin and Katz [2014], the Hamiltonian has to have the same symmetry group as the Ammann-Beenker tiling for the ground state to be of the SKK type. Therefore, if the potential $V(m)$ explicitly breaks the symmetry of the tiling, the ground state should not be an SKK state. We can easily verify this statement. Setting for example the potential to 0 except on sites with three neighbors in 1 of the 8 possible orientations explicitly breaks the eightfold rotational symmetry of the Hamiltonian, as shown on Fig. (4.16a). Applying the procedure detailed above, we decompose the ground state obtained numerically into a height part and a pre-exponential part. Note that since the Hamiltonian is not eightfold symmetric, neither is the ground state. As a result, we cannot work with the mirror-boundary approximants introduced earlier. Instead, we work with the standard approximants with periodic boundary conditions. Fig. (4.16b) shows the pre-exponential part of the ground state in perpendicular space. It does not exhibit the plateaus (seen on (4.12c)) we should observe if this function were quasiperiodic. We conclude that it is not, and that, as announced, the ground state is indeed not of the SKK type.

4.6.6. Results for the Penrose tiling

In the case of the Penrose tiling, we proceed in the same way as described above for the Ammann-Beenker tiling. For arbitrary V , we verify that its ground state is of the SKK type by computing the values of κ and the pre-exponential factors.

The evolution of κ with V is plotted in Fig. (4.17c), where one sees a significant difference between the two tilings. While the $\kappa(V)$ function for the Ammann-Beenker ground state reaches 0 only at the trivial $V = 1$ point – meaning that the ground state is critical and multifractal for all other values of V , the $\kappa(V)$ function for the Penrose ground state has two extra, non-trivial zeros at $V_1^* \simeq 0.5$, $V_2^* \simeq 3.0$ (see Fig. (4.17c)). At these two points, the ground state is extended yet non-trivial (the ground state depends only on the local environment, i.e. it is a quasiperiodic function). Just like in the case of the non-trivial Ammann-Beenker model of Sec. 4.6.5, we can wonder whether or not the properties of the Laplacian model (the low energy modes have a large

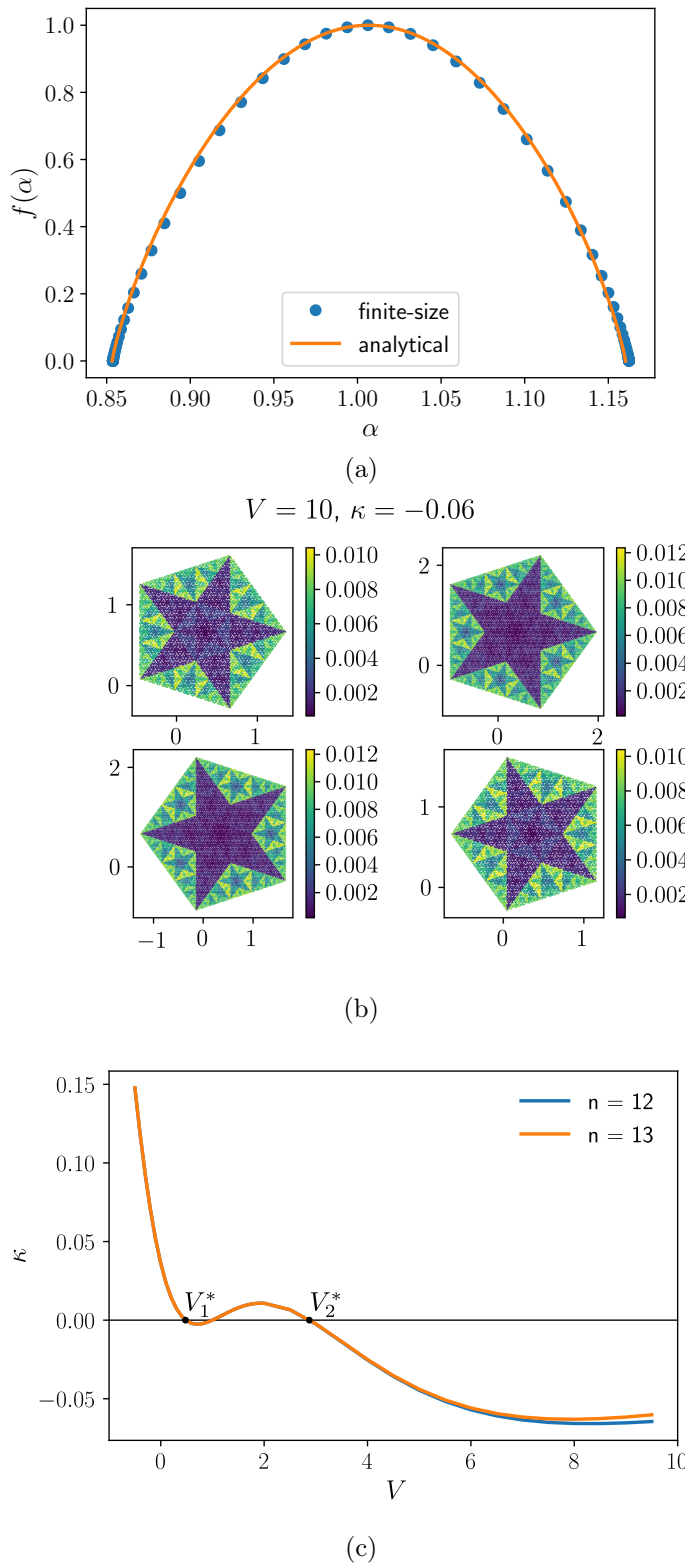


Figure 4.17. – (a): Dots: $f(\alpha)$ for the GS on the Penrose tiling ($V = -0.5$). Solid line: analytical curve (4.62) using numerically determined κ (see text). (b): The prefactors of the ground state of (4.49) on the Penrose tiling represented in the four parallel planes of internal space. Here the approximant used is $l = 12$ (61191 atoms). (c): κ versus V for the Penrose tiling calculated for two approximants (61191 and 159705 sites).

wavelength, and their energies form a continuum) also hold at the non-trivial points. These questions remain open for further study.

For arbitrary κ , the pre-exponential factors are shown to be environment dependent by plotting them in internal space (Fig. (4.17b)), as we did in the Ammann-Beenker case. For this tiling, the projections of vertices fall into four distinct pentagonal domains (corresponding to different planes of the 3D internal space), as are illustrated in Fig. (4.17b).

The fractal dimensions of the ground state computed numerically are shown in Fig. (4.17a). The curves corresponding to the two approximant sizes overlap, showing convergence of the results. The agreement with the analytical prediction Eq. (4.62) is likewise good.

4.6.7. Discussion and conclusions for 2D quasicrystals

In this section we have examined a family of tight-binding models on the 2D Ammann-Beenker and Penrose quasiperiodic tilings, and shown that they admit solutions of the SKK form: $\psi(m) = C(m) \exp(\kappa h(m))$. As in 1D, the prefactor C is quasiperiodic: it depends only on the local arrangement of the atoms, while the exponential factor contains the height field h , which is nonlocal. It is this latter term which results in multifractality of these states. We thus provide the theoretical demonstration of a property that had been numerically observed in the literature for eigenstates of quasiperiodic tilings.

We have studied various of tight-binding models with a tunable on-site potential. We observed that the form of the ground state is preserved, provided the Hamiltonian has the symmetry of the tiling. We computed analytically the properties of the height fields and fractal dimensions of the eigenstates, and compared the predictions to numerical results. We have discussed a variational calculation which allows to compute the 2D ground state wave functions to good approximation.

In 2D, ground states are observed to be of the SKK form as long as the Hamiltonian does not break any symmetry. It is therefore natural to wonder whether the ground states of 1D chains can also be SKK states. We address this question in the following section.

4.7. Are the ground states of 1D chains SKK states?

In this section, we consider again the simple tight-binding Hamiltonian (4.5) introduced in the first section of this chapter. We recall that the hopping amplitude t_m takes the value t_A or t_B if the letter m in the quasiperiodic chain we consider is an A or a B. In Sec. 4.1 we considered in details the case of the Fibonacci chain (4.5), and in Section 4.4 we considered more generally chains of the *metallic mean sequence*. Here, we place ourselves in an even more general setup, considering Sturmian chains (or canonical C&P chains), as introduced in 1.2.2. Calling α the irrational slope of the studied chain, the sequence of couplings is given by

$$t_m = \begin{cases} t_A & \text{if } S_\omega(m) = 1, \\ t_B & \text{if } S_\omega(m) = 0. \end{cases} \quad (4.70)$$

where $S_\omega(m)$ is the Sturm function (see the Appendix B) defined as $S_\omega(m) = \lfloor \omega(m+1) \rfloor - \lfloor \omega m \rfloor$. The k^{th} metallic-mean chain (studied in Section 4.4) is the Sturmian chain of slope $\alpha_k = (\sqrt{k^2 + 4} - k)/2$.

We showed in Section 4.4 that the $E = 0$ state on these chains is an SKK state. It is natural to wonder whether the *ground state* on these chains is also an SKK state. We show in this section that it is not the case: the ground state of no .

4.7.1. SKK states and logarithmic derivative

We introduce the *discrete logarithmic derivative*

$$d \log \psi(m) = \frac{\psi(m) - \psi(m-1)}{\psi(m)}, \quad (4.71)$$

where ψ is the ground state wavefunction. We can always write the ground state as $\psi(m) = C(m) \exp(\kappa h(m))$, with h an unknown height field, and C a preexponential factor. Assuming that we are close to the periodic chain (i.e. $t_a \simeq t_b$), we then have $\kappa \ll 1$ and we can write

$$d \log \psi(m) = \kappa A(m-1 \rightarrow m) + d \log C(m), \quad (4.72)$$

where $A(m-1 \rightarrow m) = h(m) - h(m-1)$. In the periodic limit $\rho \rightarrow 1$, the ground state becomes the Bloch state of period 1 (in units of the lattice spacing). If we guess that, just like in the case of the $E = 0$ state (see Section 4.1), the period of the Bloch wave sets the length of the group of letters forming effective arrows, then the function $A(m-1 \rightarrow m)$ is the *arrow function* for the ground state. The arrow function has to be *local* (i.e. the arrow only depends on the local arrangement of the atoms), and *if the ground state is of the SKK type*, the preexponential factor has to be local as well, by definition. Thus, if the ground state is of the SKK type constructed with arrows defined on single letters, its logarithmic derivative $d \log \psi$ must be local. Since in perpendicular space, points are arranged according to their local environment, *in perpendicular space, $d \log \psi$ must exhibit plateaus*, just like the preexponential factor of the ground state for 2D tilings, see eg. (4.12). $d \log \psi$ is thus a tool to determine whether the ground state is of the SKK type or not. In the next section, we compute this quantity in perturbation theory, close to the periodic chain, observe that it does not exhibit plateaus, thus proving that the ground state of Sturmian chains is not of the SKK type with arrows defined on single letters.

4.7.2. Computing the logarithmic derivative

We place ourselves close to the periodic chain, i.e. consider the case $t_A \simeq t_B$. Setting $t_A = 1$, we introduce

$$t_m = \begin{cases} 1 & \text{if B between } m \text{ and } m+1, \\ 1 - \delta & \text{otherwise.} \end{cases} \quad (4.73)$$

and we have $\delta \ll 1$. Writing the Schrödinger equation in terms of the logarithmic derivative, and introducing the *effective potential* $V(m) = t_{m-1} + t_m - 2$, we obtain to first order in δ :

$$E^{(1)} = -d \log \psi(m+1) + V(m) + d \log \psi(m), \quad (4.74)$$

where $E^{(1)}$ is the first order correction to the ground state energy: $E_{\text{GS}} = -2 + E^{(1)} + \mathcal{O}(\delta^2)$. Writing the Hamiltonian as $H = H_0 + H_1$, with H_0 the unperturbed, periodic, tight-binding Hamiltonian, we have that $E^{(1)} = \langle \psi_0 | H_1 | \psi_0 \rangle = \langle V \rangle$ where $|\psi_0\rangle = \sum_m |m\rangle$ is the ground state of H_0 . The first order correction to the ground state energy is thus simply the mean value of the effective potential.

Letting $v(m) = V(m) - \langle V \rangle$ we get an iterative equation on $d \log \psi$:

$$d \log \psi(m+1) = d \log \psi(m) + v(m). \quad (4.75)$$

Solving the recursion,

$$d \log \psi(m) = w(m) + \text{cst}, \quad (4.76)$$

where we have introduced the integrated potential $w(m) = \sum_{n=0}^m v(n)$. Let us now evaluate the integrated potential.

V_m varies according to the local environment, taking the values $V_{AB} = \delta$, $V_{BA} = \delta$ and $V_{AA} = 2\delta$ if the letters on the left and right of site m respectively form the groups AB, BA or AA. In order to compute more easily the integrated potential, let us consider the more general case where V_{AB} , V_{BA} and V_{AA} can take arbitrary values. We can express the integrated potential as

$$w(m) = \sum_{L=AB,BA,AA} V_L (|L|_\alpha(m) - (m+1)\langle L \rangle_\alpha) \quad (4.77)$$

where $|L|_\alpha(m)$ denotes the number of times the group of letters L appears around sites in the interval $[0, m]$, and where $\langle L \rangle_\alpha$ denotes the frequency of the group of letters L . The factors $|L|_\alpha(m)$ obviously depend on our choice of origin. Setting the origin at the site intercepting the slope E_\parallel (as shown e.g. on Fig. (1.6)), the number of groups BA appearing around sites in $[0, m]$ is simply equal to the number of B letters appearing in the same interval. This number is given by the formula (B.6) of the Appendix B on properties of sturmian sequences. Namely,

$$|BA|_\alpha(m) = \left\lceil \frac{\alpha m}{1 + \alpha} \right\rceil. \quad (4.78)$$

Because a B is always followed by an A,

$$|AB|_\alpha(m) = |BA|_\alpha(m+1). \quad (4.79)$$

The number of AA groups is now simply given by the ‘‘conservation law’’

$$|AA|_\alpha(m) = m + 1 - |AB|_\alpha(m) - |BA|_\alpha(m). \quad (4.80)$$

Remark that knowing the *tree of words* of the sturmian sequence α (see Section 1.3.1), one can devise similar formulas to count the occurrences of larger and larger groups of letters. Now that we have computed the occurrences of the different groups of 2 letters, it is easy to compute their frequencies:

$$\begin{aligned} \langle AB \rangle_\alpha &= \frac{\alpha}{1 + \alpha}, \\ \langle BA \rangle_\alpha &= \frac{\alpha}{1 + \alpha}, \\ \langle AA \rangle_\alpha &= \frac{1 - \alpha}{1 + \alpha}. \end{aligned}$$

Putting all these results together, and performing some algebraic manipulations exploiting the relations given in B.3, we end up with

$$w(m) = (V_{AB} + V_{BA} - 2V_{AA}) \left\{ \frac{m+1}{1+\alpha} \right\} + (V_{AA} - V_{BA}) Y \left(\left\{ \frac{m+1}{1+\alpha} \right\} - \frac{1}{1+\alpha} \right), \quad (4.81)$$

where Y is the Heaviside function. This Heaviside function just ‘‘reads’’ the letters: it is 0 if the letter at position $m+1$ is an A, and is 1 if it is a B. Noting that $\{m/(1+\alpha)\}$ is the normalized perpendicular space position of site m , we find a particularly simple expression for the integrated potential in perpendicular space:

$$w(\tilde{x}_\perp) = (V_{AB} + V_{BA} - 2V_{AA})\tilde{x}_\perp + (V_{AA} - V_{AB}) Y \left(\tilde{x}_\perp - \frac{1}{1+\alpha} \right), \quad (4.82)$$

As explained above, the integrated potential is the logarithmic derivative of the ground state up to a constant: $d \log \psi(m) = w(m) + \text{cst}$. We can determine the constant by using the fact that, because of the periodic boundary conditions on the approximant, $\sum_m d \log \psi(m) = 0$. In

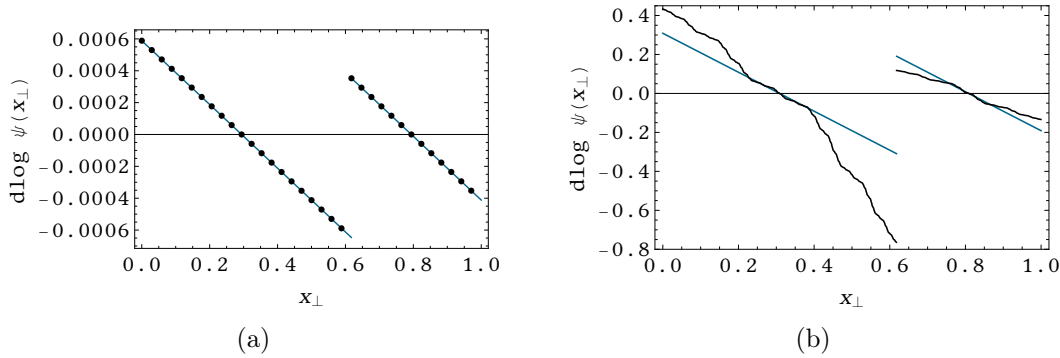


Figure 4.18. – (a): The logarithmic derivative of the ground state for $\rho = 0.999$. Dots: numerics, for a chain of 34 sites, line: analytical prediction (4.83). (b): The logarithmic derivative for $\rho = 0.5$. Black line: numerics for a chain of 1597 sites, blue line: analytical prediction.

the particular case of the pure hopping model, using the explicit expressions for the potentials, we get

$$d \log \psi(\tilde{x}_\perp) = (1 - \rho) \left((1 + \alpha)^{-1} - 2\tilde{x}_\perp + Y(\tilde{x}_\perp - (1 + \alpha)^{-1}) \right). \quad (4.83)$$

Fig. (4.18a) shows a plot of the logarithmic derivative in the case of the Fibonacci chain, $\alpha = \tau^{-1}$. We observe perfect agreement between the perturbative formula (4.83) and the numerically computed logarithmic derivative, for $\rho \simeq 1$. When ρ is lowered, the logarithmic derivative starts to wiggle, showing a devil's staircase structure, as seen on Fig. (4.18b).

As proved by formula (4.83), and as observed on Fig. (4.18a), instead of the plateaus expected if the ground state were of the SKK type with arrows defined on single letters, the logarithmic derivative is piecewise linear. We thus conclude that, on Sturmian chains, the ground state cannot be of the SKK type with arrows defined on single letters. Therefore, there are two possibilities:

1. The ground state is of the SKK type, but arrows are defined on groups of more than 1 letter. As discussed in Sec. 4.7.1, this seems unlikely, because the ground state has to vary according to its 1-letter local environment, at least in the periodic limit.
2. The ground state is not a SKK state.

To conclude this section, we remark that in principle the same analysis can be carried out for other states, to test whether or not there are of the SKK type.

4.8. Conclusion and perspectives

In this chapter we have examined a family of tight-binding models on 1D and 2D quasiperiodic tilings and shown that they admit solutions of the SKK form: $\psi(m) = C(m) \exp(\kappa h(m))$. The prefactor C is quasiperiodic: it depends only on the local arrangement of the atoms, while the exponential factor contains the height field h , which is nonlocal.

In 1D, by considering the Fibonacci chain, we show that the states in the middle of the spectrum can be written in terms of an exponential of a height function. We described the properties of the height field and shown how it is linked to the geometry of the underlying quasiperiodic tiling. Extending the arguments to the metallic-mean family of quasiperiodic 1D chains, we show that the $E = 0$ state is always multifractal. The multifractal spectrum for the $E = 0$ state on the quasiperiodic chains is seen to have a reflection symmetry around its maximum for any value of the ratio of hopping amplitudes. In contrast, we find that the $E = 0$ state is localized for the case of the aperiodic $b3$ chain, which is not quasiperiodic. We stress that the ground state of

these quasiperiodic 1D chains is *not* of the SKK form, not being expressible as a product of an exponential function of a non-local heights function and a local prefactor.

For the SKK 1D eigenstates we give the expression for the exact transmission coefficient of a finite piece of the Fibonacci 1D chain when connected to perfect leads. The scaling of the typical transmission for a given length is also given.

For the 2D Penrose and Ammann-Beenker tilings, we have studied a family of tight-binding models where the strength of the diagonal terms of H can be continuously varied. We showed that the form of the ground state is preserved, while the constant κ and the local prefactors vary. We computed analytically the properties of the height fields and fractal dimensions of the eigenstates, and compared the predictions to numerical results. We have discussed a variational calculation which allows to compute the 2D ground state wave functions to good approximation.

We conclude with some open questions. In the 1D case, we have constructed a height field by interpreting groups of two letters as arrows. One could do the same thing with groups of 3, 4, ... letters. Whether the corresponding height fields describe eigenstates remains an open question. Another point concerns extensions to other models and finding other 2D quasiperiodic tilings that host SKK eigenstates. An interesting model to study in this context would be the Socolar tiling [Socolar \[1989\]](#) with similarities to Penrose and Ammann-Beenker tiling and having 12-fold symmetry. The nature of $E = 0$ extended states in 2D tilings, if any, is another open question. The robustness of the SKK state under disorder and different types of symmetry breaking of the tight-binding Hamiltonian is also an interesting problem. These questions remain for future study.

Chapter 5.

Conclusions

We have studied the problem of simple non-interacting tight-binding Hamiltonians in quasiperiodic tilings. It has been known for a long time that such Hamiltonians have uncommon properties: they behave like systems at a phase transition, with a multifractal spectrum and critical eigenstates. Understanding how these properties stem from the quasiperiodic geometry is a task that was undertaken very early in the history of quasicrystals, and remains still very challenging.

During this thesis, we have examined first what is perhaps the most simple and well studied quasiperiodic system: the Fibonacci chain. Early studies have shown that the multifractality of the eigenstates is linked to the quasiperiodic nature of the Fibonacci chain. In particular, the perturbative renormalization group approach that we considered, valid in the strong modulation limit, explicitly relates the fractal nature of the system to its inflation symmetry. We have extended this well-known renormalization group method to describe the eigenstates at next-to-leading order, at which multifractal properties are seen to emerge.

The renormalization group has also been used to study spectral gaps. In particular, it yields recurrence relations between the values the IDOS can take inside spectral gaps of Fibonacci approximants. We exploited these to reformulate the well-known gap labeling theorem. These recurrence relations between IDOS values help us understand how the spectrum of periodic chains of increasingly large period converge to the spectrum of the quasiperiodic chain. In particular, we learn that depending on their label, gaps of approximants can be “transient” or “stable”, according to whether or not they disappear in the quasiperiodic limit. We presented numerical hints that these results can be transposed without difficulties to any other canonical C&P chain.

Interestingly, although the renormalization group we have used is approximate, with it we could non-perturbatively describe one eigenstate of the Fibonacci chain: the state at the middle of the spectrum. We have studied this state in detail, and shown that it can be written as a function of a geometrical height field. The distribution of the heights obeys a Fokker-Plank-like equation, where the number of inflations plays the role of time. Solving this equation and finding the asymptotic form of the distribution of heights gives access to properties of the central state. In particular, we have shown that the multifractal spectrum of the state, and the conductivity at the middle of the spectrum were directly related to the asymptotic form of the distribution of heights, which we could compute exactly. The results presented here are not limited to the Fibonacci chain: any quasiperiodic chain admits a central state of the same type, with the same properties. A contrario, we have shown that aperiodic chains which are not quasiperiodic have a central state of a totally different nature: localized instead of being critical.

In two dimensions, previous works have identified eigenstates described by similar height fields. Building on a recent ansatz for the ground state of two dimensional tilings, we showed that these are a solution for a family of Hamiltonians, and that they possess, just like their 1D counterparts, a multifractal spectrum that we can compute exactly.

Chapter 5. Conclusions

I have only scratched the surface of this fascinating topic. Finding robust states whose physical properties can be computed easily is exciting. However, these states are probably not typical in the vast set of eigenstates of a given model. For example, the ground state of the Fibonacci chain does not belong to their class, as we have shown... New ideas are still needed, and many things are still to be discovered! Further directions can be decomposed into two classes: i) the same tools and methods to other geometrical models (and they are plenty!), and ii) building on the knowledge we have of previously studied models to tackle different problems: single particle transport, magnetism, interactions.

Appendix A.

Fractals



Figure A.1. – A Romanesco broccoli. Image credits: Jon Sullivan (public domain).

In the course of the study of quasiperiodic Hamiltonians, we frequently encounter fractal objects. A fractal is a self-similar object: it exhibits patterns which repeats at all – or at least on many – length scales. We will also say that a fractal object exhibit *scaling symmetry*. Romanesco broccoli (Fig. (A.1)) are popular examples of fractal objects.

There are of course scale invariant objects which are not fractal. A trivial example is the unit segment $[0, 1]$. Zooming on any part of this segment, one gets a picture similar to the original one.

A.1. Scale invariance property

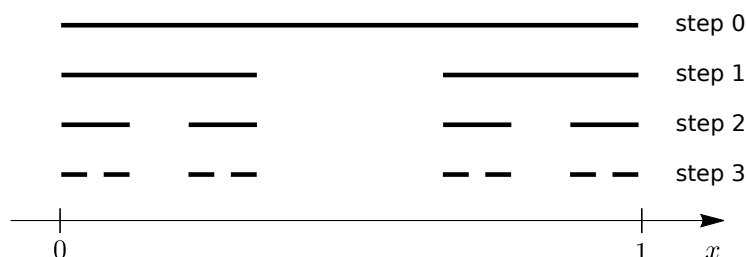


Figure A.2. – Recursive construction of the Cantor set: a initial interval of length 1 (step 0) is subdivided into 3 equal parts, and the middle part is removed (step 1). The process is then applied recursively to the remaining pieces (step 2 and next).

We consider another famous example of fractal: the Cantor set. This example is particularly relevant as the energy spectrum of certain quasiperiodic Hamiltonian has a Cantor set structure (see Chap. 2). The Cantor set can be built by recursively removing pieces from a segment, as

shown on Fig. (A.2). The Cantor set is self-similar: zooming in on any part of it one obtains the same picture.

The scaling properties of the Cantor set differ from the ones of the segment. How can we characterize this difference? Let us consider a generic fractal (or non fractal) object. We will characterize our object by a mass distribution μ . We shall note $\mu(\mathcal{R})$ the mass inside the region of space \mathcal{R} . The ‘‘mass’’ needs not be actual mass, but any physical quantity we would like to analyze. For example one could study stars in a galaxy, and the ‘‘mass’’ affected to each star could be its luminosity. In future examples concerning quasicrystals, the electronic density will often play the role of mass.

A.2. Measuring fractal set

A.2.1. The box-counting algorithm

$$\begin{array}{llll}
 B_0 & \boxed{\text{---} \text{---} \text{---} \text{---}} & l_0 = 1 & M_0(l_0) = 1 \\
 B_1 & \boxed{\text{---} \text{---}} \quad \boxed{\text{---} \text{---}} & l_1 = 1/3 & M_0(l_1) = 2 \\
 B_2 & \boxed{\text{---}} \quad \boxed{\text{---}} \quad \boxed{\text{---}} \quad \boxed{\text{---}} & l_2 = 1/3^2 & M_0(l_2) = 2^2 \\
 B_3 & \boxed{\text{---}} \quad \boxed{\text{---}} \quad \boxed{\text{---}} \quad \boxed{\text{---}} & l_3 = 1/3^3 & M_0(l_3) = 2^3
 \end{array}$$

Figure A.3. – Successive partitions of the Cantor set into boxes of common length. $M_0(\mathcal{B})$, the box-counting mass associated to the partition \mathcal{B} , is also given.

To determine whether the object we consider is fractal or not, we analyze how its mass distribution changes when length scales are changed. The *box-counting algorithm* is a way to do it. Consider a partition of the space into a set of boxes of a given length l . Let us call the set of boxes \mathcal{B}_l . Fig. (A.3) shows set of boxes at different length scales, in the case of the Cantor set. Let us now introduce the *box-counting mass at scale l*:

$$M_0(\mu; l) = \# \{ \text{boxes in } \mathcal{B}_l \text{ containing some mass} \} \quad (\text{A.1})$$

The index 0 will become useful later, when we will introduce other ways of approximating the mass at scale l .

Fig. (A.3) shows how the box-counting is computed for the Cantor set. Since $M_0(1/3^n) = 2^n$, by a change of variables one can compute the scaling of the box-counting mass:

$$M_0^{\text{Cantor}}(l) = l^{-\frac{\log 2}{\log 3}} \quad (\text{A.2})$$

Moreover, in the trivial case of a segment (or a 1D wire), the box-counting mass is simply equal to the number of boxes. Therefore, the box-counting mass scales as $1/l$. Similarly, in the case of a d -dimensional object of homogeneous mass,

$$M_0^{\text{hom}}(l) \propto l^{-d} \quad (\text{A.3})$$

Comparing equations (A.2) and (A.3), it is tempting to say that the dimension of the Cantor set is $\log 2 / \log 3$. It is also natural: on the one hand, the Cantor set seems to be less than a 1D object since it is constructed by removing most of the initial interval (in fact, the Cantor set has mass 0 if one constructs it from an initial interval of uniform linear mass), and on the other hand, it seems to be more than a 0D point since it has by construction no isolated points. So its

dimension should be in between 0 and 1: $0 < \log 2 / \log 3 \simeq 0.63 < 1$. Based on these observations, we introduce the *box-counting dimension*, defined by as

$$d_0(\mu) = \lim_{l \rightarrow 0} -\frac{\log M_0(\mu; l)}{\log l}. \quad (\text{A.4})$$

The box-counting dimension of the Cantor set is then

$$d_0^{\text{Cantor}} = \frac{\log 2}{\log 3}. \quad (\text{A.5})$$

A.2.2. The Hölder pointwise exponent

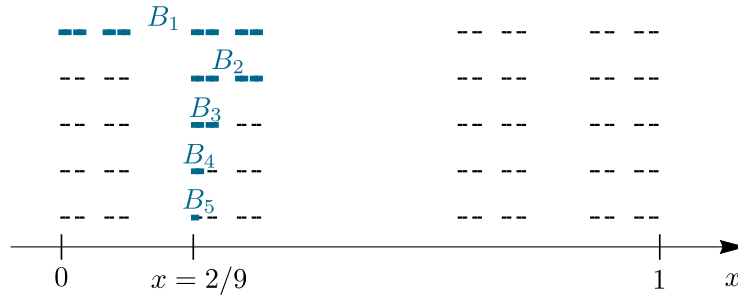


Figure A.4. – A series of boxes shrinking to the point $x = 2/9$ of the Cantor set. In blue: the part of the Cantor set that is inside a given box.

While the box-counting dimension quantifies how the object mass scales globally, the *pointwise Hölder exponent* quantifies how the object mass scales locally. Call $B(l, x)$ a box of length l containing point x . In the 1D case, boxes are simply intervals. The pointwise Hölder exponent at point x is

$$\alpha(x) = \lim_{l \rightarrow 0} \frac{\log \mu(B(l, x))}{\log l} \quad (\text{A.6})$$

For an object of homogeneous mass density, the Hölder exponent is also uniform and equal to the space dimension:

$$\alpha^{\text{hom}}(x) = d \quad (\text{A.7})$$

So, we expect the Hölder exponent to be yet another measure of the dimensionality of a fractal object. Consider again the Cantor set, and let us evaluate the Hölder exponent at point $x = 2/9$. We choose, as shown on Fig. (A.4), a series of boxes shrinking to x :

$$\begin{aligned} B_1 &= \left[0, \frac{1}{3}\right] \\ B_2 &= \left[\frac{2}{9}, \frac{1}{3}\right] \\ B_3 &= \left[\frac{2}{9}, \frac{2}{9} + \frac{1}{3^3}\right] \\ &\vdots \\ B_n &= \left[\frac{2}{9}, \frac{2}{9} + \frac{1}{3^n}\right] \end{aligned}$$

Appendix A. Fractals

This series of boxes is represented on figure (A.4). We compute the length of each box and the mass inside:

$$\begin{array}{ll}
 |B_1| = \frac{1}{3} & \mu(B_1) = \frac{1}{2} \\
 |B_2| = \frac{1}{9} & \mu(B_2) = \frac{1}{4} \\
 |B_3| = \frac{1}{3^2} & \mu(B_3) = \frac{1}{2^3} \\
 \vdots & \vdots \\
 |B_n| = \frac{1}{3^n} & \mu(B_n) = \frac{1}{2^n}
 \end{array}$$

Using the definition of the Hölder exponent, we can now compute it:

$$\alpha^{\text{Cantor}}(2/9) = \lim_{n \rightarrow \infty} \frac{\log \mu(B_n)}{\log |B_n|} \quad (\text{A.8})$$

$$\alpha^{\text{Cantor}}(2/9) = \frac{\log 2}{\log 3} \quad (\text{A.9})$$

So the Hölder exponent at point $2/9$ is equal to the box-counting dimension of the Cantor set. The Cantor set is uniformly self-similar: to get a structure similar to the whole Cantor set, we can rescale any part of it with the same scaling factor. One says that the Cantor set is a *monofractal*. Owing to the monofractal nature of the Cantor set, it is clear that the Hölder exponent is uniform:

$$\alpha^{\text{Cantor}}(x) = \frac{\log 2}{\log 3} \quad (\text{A.10})$$

So the Hölder exponent of the Cantor set is uniform and equal to its box-counting dimension. These properties are characteristic of a monofractal object. But what about fractal objects which are not uniformly self-similar: multifractals?

A.2.3. Multifractals and the generalized fractal dimensions

Two scales Cantor set and multifractals

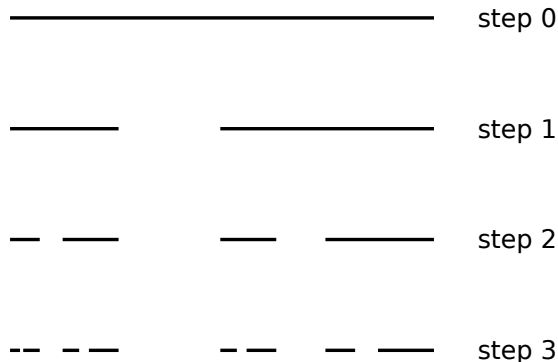


Figure A.5. – Iterative construction of a two scales Cantor set.

“Real life” fractals are most of the time *multifractals*, meaning that the mass scales differently when zooming on different parts of the structure, or, said differently, that the Hölder exponent is

not uniform. We introduce here a first, simple example of such a multifractal set: the *two scales Cantor set*. This set was introduced in a slightly more general setting in Halsey et al. [1986].

To construct the two scales Cantor set, let us choose two lengths, l_1 and l_2 . Instead of cutting the unit interval into 3 pieces of equal length like was done for constructing the usual Cantor set, we cut the unit interval into 3 pieces of length l_1 , $1 - l_1 - l_2$ and l_2 . Like for the usual Cantor set, the central piece is removed and the cutting procedure is then repeated on the two remaining pieces. Fig. (A.5) illustrate the construction process.

Let us now prove that on the two scales Cantor set the Hölder exponent is non-uniform. To fix the ideas, we set $l_1 = 1/4$ and $l_2 = 1/2$, like illustrated on Fig. (A.5). Let us evaluate the Hölder exponents of the two end points of the unit interval, $x = 0$ and $x = 1$. We consider series of intervals shrinking to these points:

$$\begin{aligned} B_1^{(1)} &= \left[0, \frac{1}{4}\right] & B_1^{(2)} &= \left[\frac{1}{2}, 1\right] \\ B_2^{(1)} &= \left[0, \frac{1}{4^2}\right] & B_2^{(2)} &= \left[1 - \frac{1}{4}, 1\right] \\ &\vdots & &\vdots \\ B_n^{(1)} &= \left[0, \frac{1}{4^n}\right] & B_n^{(2)} &= \left[1 - \frac{1}{2^n}, 1\right] \end{aligned}$$

Like previously, we compute the length of the intervals and the mass inside: for the first series, shrinking to $x = 0$, one has $|B_n^{(1)}| = 1/4^n$, $\mu(B_n^{(1)}) = 1/3^n$, and for the second series, shrinking to $x = 1$, one has $|B_n^{(2)}| = 1/2^n$, $\mu(B_n^{(2)}) = (2/3)^n$. Computing the Hölder exponents is now straightforward:

$$\alpha(0) = \frac{\log 3}{\log 4} \simeq 0.79 \qquad \alpha(1) = \frac{\log 3/2}{\log 2} \simeq 0.58 \qquad (\text{A.11})$$

The Hölder exponent $\alpha(x)$ is indeed non-uniform in the case of the two scales Cantor set.

The whole set of x dependent Hölder exponents can be cumbersome to compute in practice. Let us forget about the precise form of the function $\alpha(x)$. Consider the set of points x such that $\alpha(x) = \alpha$. In the simple case of a monofractal like the Cantor set, this set is just the whole fractal object, but in the case of a multifractal object like the two scales Cantor set, it is subset of the whole fractal object. This subset also constitute a generically fractal object. Let us call $f(\alpha)$ its box-counting dimension. Calling μ_α the mass distribution of the the set of points such that $\alpha(x) = \alpha$, $f(\alpha)$ is such that

$$M_0(\mu_\alpha; l) \underset{l \rightarrow 0}{\sim} l^{-f(\alpha)} \qquad (\text{A.12})$$

where M_0 is the box-counting mass introduced in Eq. (A.1). Since M_0 counts the number of occupied boxes, $l^{-f(\alpha)+1}$ is proportional to the probability that the Hölder exponent equals α . Thus, $f(\alpha)$ contains the information about the scaling of the Hölder exponents' distribution. For that reason, we shall call $f(\alpha)$ the *multifractal spectrum*. A multifractal spectrum reduced to a point is the signature of either a trivial (non-fractal) object, or of a monofractal, while a non-trivial multifractal spectrum is the signature of a multifractal object.

We now link the multifractal spectrum with the box-counting dimension. First, we need to generalize the box-counting mass introduced in Eq. (A.1). Consider as before \mathcal{B}_l , a partition of space into boxes of length l . Denote by $\mu(B)$ the mass contained in box B , and μ_{tot} the total mass of the object. Let us introduce the quantity

$$M_q(\mu; l) = \sum_{B \in \mathcal{B}_l} \left(\frac{\mu(B)}{\mu_{\text{tot}}} \right)^q, \qquad (\text{A.13})$$

Appendix A. Fractals

which we shall call the q -mass in this thesis. Remark that M_0 corresponds to the box-counting mass introduced in Eq. (A.1). When q is large, only the largest terms in the sum (A.13) contribute significantly to the q -mass. Therefore, a q -mass with q large probes the regions where the mass density is the largest. Similarly, when q large in absolute value and negative, regions where the mass density is the smallest are probed. So, varying q enables us to capture more information about the scaling of the object.

For an d -dimensional homogeneous mass distribution, the q -mass scales as

$$M_q^{\text{hom}}(\mu; l) \underset{l \rightarrow 0}{\sim} l^{(q-1)d} \quad (\text{A.14})$$

In the light of this result, we introduce the *generalized fractal dimensions*:

$$d_q(\mu) = \lim_{l \rightarrow 0} \frac{1}{q-1} \frac{\log M_q(\mu; l)}{\log l} \quad (\text{A.15})$$

In particular, d_0 is indeed the box-counting dimension introduced before. d_1 is sometime called the information dimension, and d_2 the correlation dimension.

We now make the connection between the q -mass and the multifractal spectrum. Calling $B(x, l)$ the box of length l shrinking to point x , we rewrite the q -mass (A.13) as

$$M_q(\mu; l) = \sum_x \left(\frac{\mu(B(x, l))}{\mu_{\text{tot}}} \right)^q \quad (\text{A.16})$$

Recalling the definition of the pointwise Hölder exponents (A.6) and of the multifractal spectrum (A.12), we have successively:

$$M_q(\mu; l) \underset{l \rightarrow 0}{\sim} \sum_x l^{q\alpha(x)} \quad (\text{A.17})$$

$$M_q(\mu; l) \underset{l \rightarrow 0}{\sim} \sum_{\alpha} M_0(\mu_{\alpha}; l) l^{q\alpha} \quad (\text{A.18})$$

$$M_q(\mu; l) \underset{l \rightarrow 0}{\sim} \sum_{\alpha} l^{q\alpha - f(\alpha)} \quad (\text{A.19})$$

When $l \rightarrow 0$, the sum is dominated by the term which minimizes $q\alpha - f(\alpha)$. Let us call this term α_q . We have

$$M_q(\mu; l) \underset{l \rightarrow 0}{\sim} l^{q\alpha_q - f(\alpha_q)} \quad (\text{A.20})$$

Comparing with the definition of the generalized fractal dimensions (A.15), we end up with a relation between the multifractal spectrum and the generalized dimensions:

$$(q-1)d_q = q\alpha_q - f(\alpha_q). \quad (\text{A.21})$$

Let us define

$$\tau_q = (q-1)d_q. \quad (\text{A.22})$$

Remark that $\alpha_q = \tau'_q$. Using this property, and the relation (A.21), the multifractal spectrum can be computed graphically from τ_q . More precisely, and as shown on Fig. (A.6), *the multifractal spectrum $f(\alpha)$ is the Legendre transform of τ_q .*

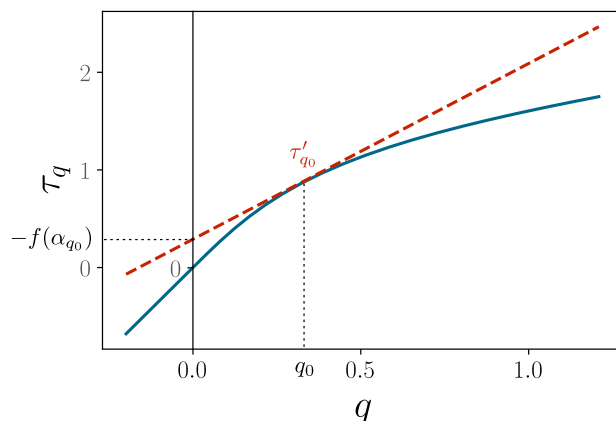


Figure A.6. – Graphical construction of the multifractal spectrum at point q_0 . In blue, the τ_q function. In red, the tangent to τ_q at point q_0 . The vertical intercept of the tangent is $-f(\alpha_{q_0})$.

A.3. Computing fractal dimensions and the multifractal spectrum

Fractal dimensions and the multifractal spectrum contain the same information since they are Legendre transform of one another. It is often interesting to compute both to gain more knowledge about the fractal set at hand.

A practical way of computing $f(\alpha)$ is to compute first the generalized fractal dimensions d_q using the so-called *partition function*. Then we can access the multifractal spectrum using the fact that $\alpha_q = \tau'_q$ (we recall that $\tau_q = (q - 1)d_q$), and $f(\alpha_q) = q\alpha_q - \tau_q$.

As before, consider a partition of the space in boxes. This time, we allow the boxes to have different lengths, and we call $l(x)$ the length of the box $B(x, l)$, shrinking to point x . Allowing boxes to have different sizes can be handy for numerical computations. The partition function Γ is defined by

$$\Gamma(q, \tau) = \sum_x \frac{\mu(B(x, l))^q}{l(x)^\tau} \quad (\text{A.23})$$

We have $\Gamma(q, \tau > \tau_q) \rightarrow +\infty$, and $\Gamma(q, \tau < \tau_q) \rightarrow 0$ in the limit $l(x) \rightarrow 0$. Only at $\tau = \tau_q$ does Γ have a finite nonzero limit when $l \rightarrow 0$. This gives us a practical way of computing τ_q .

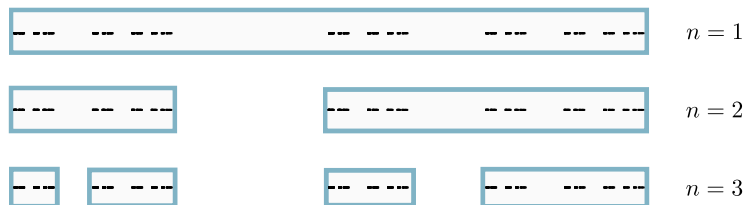


Figure A.7. – Successive partitions of the two scales Cantor set into boxes.

As an illustrative example, let us compute the fractal dimensions and multifractal spectrum of the two scales Cantor set introduced previously (Fig. (A.5) shows how this set is constructed). Study of quasiperiodic Hamiltonians will provide us with more physical examples of multifractal spectra.

We partition the two scales Cantor set into boxes, as shown by Fig. (A.7). We then compute $\Gamma^{(n)}(q, \tau)$, the partition function associated to the n^{th} partition of the Cantor set. For $n \geq 1$,

$$\Gamma^{(n+1)} = \left(\Gamma^{(n)}\right)^2 \quad (\text{A.24})$$

Appendix A. Fractals

Moreover,

$$\Gamma^{(1)}(q, \tau) = \frac{\left(\frac{1}{3}\right)^q}{\left(\frac{1}{4}\right)^\tau} + \frac{\left(\frac{2}{3}\right)^q}{\left(\frac{1}{2}\right)^\tau} \quad (\text{A.25})$$

The partition function has a finite nonzero limit when $n \rightarrow \infty$ (i.e. when the length of the boxes goes to 0) if and only if $\Gamma^{(1)} = 1$. Therefore, $\Gamma^{(1)}(q, \tau_q) = 1$ and $\tau_q = \log x / \log 2$ with

$$x = 2^{q-1} \left(\sqrt{1 + 4 \left(\frac{3}{4}\right)^q} - 1 \right) \quad (\text{A.26})$$

In particular, the box-counting dimension is $d_0 = \log \tau / \log 2$, where $\tau = (1 + \sqrt{5})/2$ is the golden ratio. Once τ_q is known, it is not difficult to compute the multifractal spectrum. Fig. (A.8) shows it.

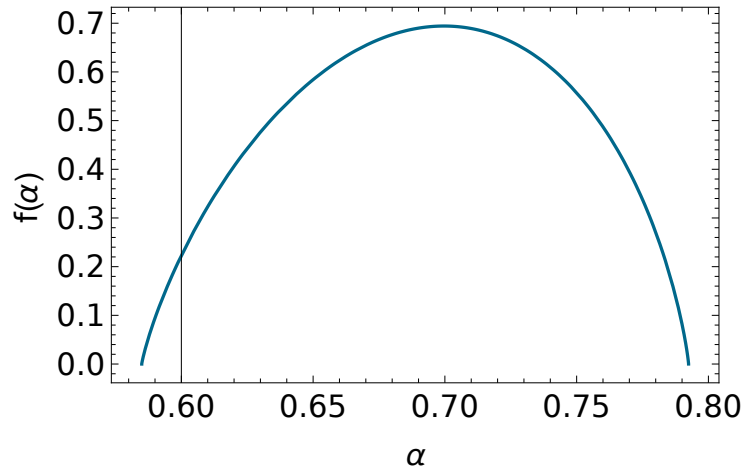


Figure A.8. – The multifractal spectrum of the two scales Cantor set.

Generic properties of the multifractal spectrum

- As a Legendre transform of a concave function (see Fig. (A.6)), the multifractal spectrum must be a concave function. So, the multifractal spectrum has at most one maximum, reached at point α_0 . The bell shape of the multifractal spectrum observed on Fig. (A.8) is thus generic.
- The slope of the multifractal spectrum verifies

$$q = f'(\alpha_q) \quad (\text{A.27})$$

- In particular, $f(\alpha_0) = d_0$.
- $\alpha_{\min} = d_{+\infty}$, $\alpha_{\max} = d_{-\infty}$.

A.4. Statistical physics and multifractal analysis

In this section, we discuss two completely independent connections between statistical physics and multifractal analysis.

A.4.1. Multifractal analysis in the language of statistical physics

There is a formal analogy between the concepts of statistical physics and those of multifractal analysis, as discussed in details in Kohmoto [1988]. Let us consider as before \mathcal{B}_l , a partition of

our space into a set of boxes. Indexing the boxes in this partition with an integer i , and calling μ_i the mass in the i^{th} box, we can rewrite the q -mass (A.13) as

$$M_q(\mu; l) = \sum_i \left(\frac{\mu_i}{\mu_{\text{tot}}} \right)^q. \quad (\text{A.28})$$

Recalling the definition of the pointwise Hölder exponent (A.6), this equation can then be recast as

$$M_q(\mu; l) = \sum_i e^{-\beta_q(l) \alpha_i}, \quad (\text{A.29})$$

where we have introduced the *inverse temperature* $\beta_q(l) = q |\log l|$. Now, the link with statistical physics is evident. Interpreting the space our mass distribution lives in as the phase space of some statistical physics system, and interpreting $\beta_q(l)$ as the inverse temperature of the system, we conclude that $\exp(-\beta_q(l) \alpha_i)$ is proportional to the probability of the system visiting the i^{th} box. The Hölder exponent α_i is the energy of the system in this configuration, and the q -mass is the partition function of the system. The free energy of the statistical physics system is proportional to the fractal dimension:

$$F(\beta_q(l)) \underset{l \rightarrow 0}{\sim} \frac{q}{q-1} d_q, \quad (\text{A.30})$$

while its average energy coincides with the Hölder exponent of equation (A.21):

$$\bar{E}(\beta_q(l)) \underset{l \rightarrow 0}{\sim} \alpha_q. \quad (\text{A.31})$$

Finally, the multifractal spectrum is proportional to the entropy:

$$S(\beta_q(l)) \underset{l \rightarrow 0}{\sim} |\log l| f(\alpha_q). \quad (\text{A.32})$$

A.4.2. Rényi entropies and quenches

The q -mass can be given a physical meaning in the context of a quenched statistical physics system Baez [2011], in the following way. Partition the phase space of a given system into boxes, and call $\mu(B(x))$ the probability that the system's state is in box $B(x)$ centered about x . Suppose that the system is at thermal equilibrium at temperature T . When the boxes length goes to zero, we have $\mu(B(x)) \sim \exp(-E(x)/T)/Z$ where $E(x)$ is the average energy of the state in box $B(x)$. Remark that the partition function, temperature and energy introduced here have no connection with the quantities defined in the previous subsection. They are the partition function, temperature and energy of a “real” statistical physics system, not quantities defined *by analogy* with statistical physics. We now introduce the Rényi entropy of order q :

$$S_q = \frac{1}{q-1} \log M_q \quad (\text{A.33})$$

Remark that $d_q = \lim_{l \rightarrow 0} S_q / \log l$ where l is the boxes width. Also remark that S_1 is equal to the entropy of the system. Furthermore, if the system is brought by a sudden quench to temperature $T' = T/q$, then the maximum amount of work that can be extracted from the system as it reaches thermal equilibrium at the new temperature T' , divided by the change in temperature, equals the system's Rényi entropy of order q in its original state at temperature T . In other words,

$$S_{T/T'} = - \frac{F(T') - F(T)}{T' - T} \quad (\text{A.34})$$

where F is the free energy of the system.

A.5. Discrete scale invariance and log-periodic oscillations

Fractals being scale invariant distributions of points, a physical quantity defined on a fractal can be modeled as a function with discrete scale invariance. That is a function verifying

$$bf(x) = f(ax). \quad (\text{A.35})$$

for some fixed a . Let us assume to begin with that the function has *continuous* scale invariance, meaning that the previous equation holds for any a . It is then an easy exercise to show that the only solutions to this functional equation are the power laws of the form $f(x) = Cx^{\log b / \log a}$.

Imposing only discrete scale invariance, we expect the set of solutions to be larger. In fact, one can prove [Lapidus and Van Frankenhuyzen \[2013\]](#), [Sedgewick and Flajolet \[2013\]](#), [Akkermans \[2013\]](#) that the solutions are

$$f(x) = C \left(\frac{\log x}{\log a} \right) x^{\frac{\log b}{\log a}}, \quad (\text{A.36})$$

where C is a periodic function of period 1. Thus, f is a power-law multiplied by a *log-periodic function*. Such functions are frequently observed in physical systems with some kind of discrete scale invariance, see e.g. [Akkermans \[2013\]](#), [Khamzin et al. \[2015\]](#). The case of quasiperiodic tiling is a bit more complicated. They are not discrete scale invariant objects (the distribution of tiling points is not fractal at all, but perfectly regular). However, they can often be constructed by the discrete *scale invariant process* of substitution (or inflation). Therefore, it comes as no surprise that many physical quantities on quasiperiodic tilings exhibit power-laws with log-periodic modulations, see e.g. [Lifshitz and Mandel \[2011\]](#), [Thiem \[2015\]](#). We shall see three examples of such quantities in this thesis: [3.4](#), [4.3](#) and [4.4.2](#).

Appendix B.

Properties of Sturmian sequences

B.1. Counting letters

Consider the Sturmian chain associated to α (irrational or not). Then, the number of A letters in the interval between site 0 and site i is

$$|A|_{\alpha}(m) = \left\lfloor \frac{m}{1 + \alpha} \right\rfloor \quad (\text{B.1})$$

Proof 1 (Counting letters) *Let α be the number used by canonical C&P to build the Sturmian word we consider. We chose a point of the \mathbb{Z}^2 lattice, and set the slope so that it passes through this point, which is chosen as the origin. If now θ denotes the angle the slope makes with the horizontal axis (i.e. $\alpha = \tan \theta$), the point $\mathbf{x} = (i, j) \in \mathbb{Z}^2$ has coordinates*

$$x_{\parallel} = i \cos \theta + j \sin \theta \quad (\text{B.2})$$

$$x_{\perp} = j \cos \theta - i \sin \theta \quad (\text{B.3})$$

in the basis whose first axis is along the slope, and whose second axis is such that the basis is direct and orthonormal. Then, the condition for \mathbf{x} to be in the tiling is $0 \leq x_{\perp} < \cos \theta + \sin \theta$, i.e.

$$0 \leq \frac{m}{1 + \alpha} - i < 1, \quad (\text{B.4})$$

where we have introduced the integer $m = i + j$ which counts tiling points from left to right starting from the origin. We recognize here the definition of the floor function, and we have

$$i = \left\lfloor \frac{m}{1 + \alpha} \right\rfloor. \quad (\text{B.5})$$

Since i counts the number of horizontal bounds we have encountered by going m sites to the right from the origin, and since the number of horizontal bounds corresponds in the C&P picture to the number of A letters in the Sturmian word picture, the proof is complete.

Similarly, the number of B letters is

$$|B|_{\alpha} m = m - |A|_{\alpha} m = \left\lceil \frac{\alpha m}{1 + \alpha} \right\rceil \quad (\text{B.6})$$

B.2. Sturm functions

Since $|A|_{\alpha}(m)$ counts the number of A letters between sites 0 and m , the *Sturm function*

$$S_{\alpha}(m) = |A|_{\alpha}(m + 1) - |A|_{\alpha}(m) \quad (\text{B.7})$$

takes the values 0 or 1 according to

$$S_\alpha(m) = \begin{cases} 0 & \text{if B between } m \text{ and } m+1, \\ 1 & \text{if A between } m \text{ and } m+1. \end{cases} \quad (\text{B.8})$$

It thus generates the Sturmian sequence associated to α .¹ Tab. (B.1) shows the first few terms of the Fibonacci Sturmian sequence.

m	0	1	2	3	4	5	6	7	8	9	10	11	12
$S_{\tau^{-1}}(n)$	0	1	0	1	1	0	1	0	1	1	0	1	1
sequence	B	A	B	A	A	B	A	B	A	A	B	A	A

Table B.1. – The first few terms of the Fibonacci sequence, associated with the inverse of the golden ratio, τ^{-1} . Below is shown the corresponding sequence of letters.

B.3. Mod 1 arithmetic and Sturmian sequences

B.3.1. Basic properties

In this section we recall some results about numbers modulo 1, or equivalently, about fractional part of numbers. Let us begin with equivalent definitions of the fractional part:

$$\{x\} = x \pmod{1}, \quad (\text{B.9})$$

$$\{x\} = x - \lfloor x \rfloor, \quad (\text{B.10})$$

$$\{x\} = x + 1 - \lceil x \rceil. \quad (\text{B.11})$$

Algebraic properties:

$$\{x + y\} = \{\{x\} + \{y\}\}, \quad (\text{B.12})$$

$$\{xy\} = \{\{x\}\{y\}\}. \quad (\text{B.13})$$

A useful one:

$$\{x\} + \{-x\} = 1. \quad (\text{B.14})$$

B.3.2. Mod 1 arithmetic and internal space coordinates

We will frequently use fractional parts of the form

$$\tilde{x}_\perp(\alpha, n) = \left\{ \frac{n}{1 + \alpha} \right\} \quad (\text{B.15})$$

where n is an integer and α an irrational (quasiperiodic chain) or a rational (periodic chain) number. It satisfies the following identities:

$$\tilde{x}_\perp(1/\alpha, -n) = \tilde{x}_\perp(\alpha, n), \quad (\text{B.16})$$

$$\tilde{x}_\perp(\alpha, -n) = 1 - \tilde{x}_\perp(\alpha, n). \quad (\text{B.17})$$

Below, we show that $\tilde{x}_\perp(\alpha, n)$ is the normalized perpendicular space position of n :

$$\tilde{x}_\perp(\alpha, n) = \frac{x_\perp(\alpha, n)}{H(\alpha)} \quad (\text{B.18})$$

where $H(\alpha) = (1 + \alpha)/\sqrt{1 + \alpha^2}$ is the width of the canonical window.

1. Mathematicians (see e.g. Fogg [2002]) usually define the Sturm function by the difference of B letters, which means the role of 0 and 1 is exchanged in equation (B.8).

Proof 2 (Normalized perpendicular position) From the proof (1) one knows that the perpendicular space projection of point $\mathbf{x} = (i, j)$ is

$$x_{\perp} = j \cos \theta - i \sin \theta. \quad (\text{B.19})$$

We have $\cos \theta = 1/\sqrt{1+\alpha^2}$ and $\sin \theta = \alpha/\sqrt{1+\alpha^2}$, so that the window width is $H(\alpha) = \cos \theta + \sin \theta = (1+\alpha)/\sqrt{1+\alpha^2}$. Using the expressions of the cos and sin, and then the expression of i and j derived in the proof (1), we get successively

$$\begin{aligned} \sqrt{1+\alpha^2}x_{\perp} &= j - \alpha i, \\ \sqrt{1+\alpha^2}x_{\perp} &= |B|_{\alpha}m - \alpha|A|_{\alpha}m. \end{aligned}$$

where $m = i + j$. Using the basic properties of the fractional part, we arrive at

$$\begin{aligned} \sqrt{1+\alpha^2}x_{\perp} &= 1 - \left\{ \frac{\alpha m}{1+\alpha} \right\} + \alpha \left\{ \frac{m}{1+\alpha} \right\}, \\ \sqrt{1+\alpha^2}x_{\perp} &= 1 - \left\{ -\frac{m}{1+\alpha} \right\} + \alpha \left\{ \frac{m}{1+\alpha} \right\}, \\ \sqrt{1+\alpha^2}x_{\perp} &= (1+\alpha) \left\{ \frac{m}{1+\alpha} \right\}. \end{aligned}$$

In perpendicular space, the tiles are arranged according to their local environment. In particular,

$$\begin{cases} 0 \leq \tilde{x}_{\perp}(\alpha, m) < \frac{\alpha}{1+\alpha} \implies \text{B between } m \text{ and } m+1, \\ \frac{\alpha}{1+\alpha} \leq \tilde{x}_{\perp}(\alpha, m) < 1 \implies \text{A between } m \text{ and } m+1. \end{cases} \quad (\text{B.20})$$

B.3.3. Approximants

In this section, we discuss how a given Sturmian word can be approximated by periodic words called *approximants*.

Best approximants of an irrational number

Consider α irrational. We want to construct a series of rational approximations of α , i.e. rational numbers α_l such that $\alpha_l \rightarrow \alpha$ when $l \rightarrow \infty$.

Consider the fraction p/q . Reducing the fraction if needed, we can consider p and q coprime. In this case, the canonical C&P word of slope p/q is periodic, with a unit cell of $L = p + q$ letters. We say that p/q is a *best approximant* of α if

$$|q\alpha - p| < |q'\alpha - p'| \quad (\text{B.21})$$

for all integers $q' \leq q$ and for all integers p' . Note that in particular

$$\left| \alpha - \frac{p}{q} \right| < \left| \alpha - \frac{p'}{q'} \right| \quad (\text{B.22})$$

so that among all fractions of denominator smaller or equal to q , best approximants best approximate α .

Convergents and best approximants

Let us now introduce a practical way of generating best approximants. Consider the continued fraction representation of α , which writes, for $\alpha < 1$ (which is the case we are interested in here) as:

$$\alpha = \frac{1}{a_1 + \frac{1}{a_2 + \dots}} \quad (\text{B.23})$$

also written as $\alpha = [a_1, a_2, \dots]$. The positive integers a_i are uniquely defined. The l^{th} *convergent* of α is the rational number obtained by cutting the continued fraction at position l : $\alpha_l = [a_1, a_2, \dots, a_l]$. It turns out that *convergents are best approximants* of α . We shall use them to produce periodic approximants of a given Sturmian word. Successive convergents verify

$$p_{l-1}q_l - p_lq_{l-1} = (-1)^l \quad (\text{B.24})$$

Conumbering and best approximants

In \mathbb{Z}^2 , the period of the l^{th} approximant is $\mathbf{b}_l = (q_l, p_l)$. Define now the *generator* $\mathbf{a}_l = (q'_l, p'_l)$ such that \mathbf{a}_l and \mathbf{b}_l form a unit cell of the approximant:

$$\mathbf{b}_l \times \mathbf{a}_l = 1 \quad (\text{B.25})$$

Given equation (B.24), the previous convergent is suited to build the generator: $\mathbf{a}_l = (-1)^l(q_{l-1}, p_{l-1})$. For example, in the case of the Fibonacci chain, the l^{th} convergent is $\alpha_l = F_l/F_{l+1}$ (where F_l is the l^{th} Fibonacci number, $F_1 = F_2 = 1$), so that one has $\mathbf{b}_l = (F_{l+1}, F_l)$ and $\mathbf{a}_l = (-1)^l(F_l, F_{l-1})$.

We can write a given lattice point $\mathbf{n} = (i, j) \in \mathbb{Z}^2$ in this new basis:

$$\mathbf{n} = c\mathbf{a}_l + k\mathbf{b}_l \quad (\text{B.26})$$

The c coefficient has a natural interpretation. Indeed, noting that $m = i + j$ is the labeling of the m^{th} point of the C&P tiling, then c can be written as

$$c = mq_l \pmod{p_l + q_l} \quad (\text{B.27})$$

We shall call say that c is the *conumbering* of m . The conumbering has a geometrical interpretation, as we shall see now.

B.3.4. Approximants and conumbering

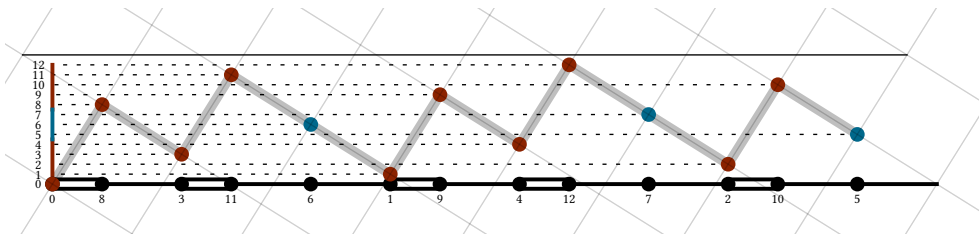


Figure B.1. – The cut and project construction of the approximant $\alpha = 5/8$ of the Fibonacci chain. The conumbering of each site is shown below it.

Fig (B.1) shows an approximant of the Fibonacci chain, together with the conumbering of each of its sites. As one can see, the conumbering of a site exactly corresponds to the ordering of the site in perpendicular space E_{\perp} . Let us prove it.

We consider an approximant of slope $\alpha_l = p_l/q_l$. In this case, the structure is periodic, with a unit cell of $L_l = p_l + q_l$ sites. We have successively

$$\tilde{x}_\perp(\alpha_l, m) = \left\{ \frac{q_l m}{L_l} \right\} \quad (\text{B.28})$$

$$\tilde{x}_\perp(\alpha_l, m) = \frac{1}{L_l} (q_l m \pmod{L_l}) \quad (\text{B.29})$$

So, the normalized perpendicular coordinate is proportional to the integer

$$c = q_l m \pmod{L_l} \quad (\text{B.30})$$

which is nothing but the conumber of site m (see Eq. (B.27)), as announced. For example, in the case of the Fibonacci chain, defining the 1th approximant as the 1th convergent of τ^{-1} : $\alpha_l = F_l/F_{l+1}$, we obtain a periodic chain of period F_{l+2} , and the conumbering is given by

$$c = F_{l+1} m \pmod{F_{l+2}}. \quad (\text{B.31})$$

This formula can moreover easily be inverted, yielding

$$m = (p'_l + q'_l)c \pmod{L_l}. \quad (\text{B.32})$$

In the case of the Fibonacci chain, we have

$$m = (-1)^l F_{l+1} c \pmod{F_{l+2}} \quad (\text{B.33})$$

Appendix C.

Brillouin-Wigner perturbation theory

Suppose we have a Hamiltonian

$$\hat{H} = \hat{H}_0 + \lambda \hat{H}_1 \quad (\text{C.1})$$

with \hat{H}_0 and \hat{H}_1 of the same order of magnitude, and $\lambda \ll 1$. The goal of perturbation theory is to express order by order in λ the energies and eigenstates of \hat{H} in terms of the energies and eigenstates of \hat{H}_0 . Brillouin-Wigner perturbation theory reaches this goal by writing an effective Hamiltonian which is easier to treat than the full Hamiltonian.

Let \hat{Q} denote the projector on the eigenspace of ε , energy of the unperturbed Hamiltonian \hat{H}_0 . Let us call \hat{P} the projector orthogonal to \hat{Q} . We are only interested in what happens in the subspace \hat{Q} . Our goal is to write an effective Hamiltonian \hat{H}_{eff} which coincides with \hat{H} on \hat{Q} , and which is easy to approximate.

To this end, let us choose $|\psi\rangle$, an eigenstate of \hat{H} associated to the energy E . We wish to express $|\psi\rangle$ in terms of its projection $\hat{Q}|\psi\rangle$ only. We have successively

$$(E - \hat{H}_0) |\psi\rangle = \lambda \hat{H}_1 |\psi\rangle \quad (\text{C.2})$$

$$(E - \hat{H}_0) \hat{P} |\psi\rangle = \lambda \hat{P} \hat{H}_1 |\psi\rangle \quad (\text{C.3})$$

$$\hat{P} |\psi\rangle = \lambda \hat{P} \frac{1}{E - \hat{H}_0} \hat{H}_1 |\psi\rangle \quad (\text{C.4})$$

and thus

$$|\psi\rangle = (\hat{P} + \hat{Q}) |\psi\rangle \quad (\text{C.5})$$

$$|\psi\rangle = \hat{Q} |\psi\rangle + \lambda \hat{P} \frac{1}{E - \hat{H}_0} \hat{H}_1 |\psi\rangle \quad (\text{C.6})$$

Iterating the previous relation, and we obtain

$$|\psi\rangle = \left(1 + \lambda \hat{P} \frac{1}{E - \hat{H}_0} \hat{H}_1 + \lambda^2 \hat{P} \frac{1}{E - \hat{H}_0} \hat{H}_1 \hat{P} \frac{1}{E - \hat{H}_0} \hat{H}_1 + \dots \right) \hat{Q} |\psi\rangle \quad (\text{C.7})$$

which we can write more compactly as

$$|\psi\rangle = \sum_{n=0}^{\infty} \left(\lambda \hat{P} \frac{1}{E - \hat{H}_0} \hat{H}_1 \right)^n \hat{Q} |\psi\rangle \quad (\text{C.8})$$

Applying $\hat{Q}\hat{H}$ on $|\psi\rangle$, we then obtain

$$E \hat{Q} |\psi\rangle = \left(\varepsilon + \hat{Q} \hat{H}_1 \sum_{n=0}^{\infty} \lambda^{n+1} \left(\hat{P} \frac{1}{E - \hat{H}_0} \hat{H}_1 \right)^n \right) \hat{Q} |\psi\rangle \quad (\text{C.9})$$

Therefore, on the subspace \hat{Q} the full Hamiltonian \hat{H} can be replaced by the effective Hamiltonian

$$\hat{H}_{\text{eff}} = \varepsilon + \hat{Q} \hat{H}_1 \sum_{n=0}^{\infty} \lambda^{n+1} \left(\hat{P} \frac{1}{E - \hat{H}_0} \hat{H}_1 \right)^n \quad (\text{C.10})$$

Appendix C. Brillouin-Wigner perturbation theory

which we can write in a more symmetric fashion:

$$\boxed{\hat{H}_{\text{eff}} = \hat{Q}\hat{H}_0\hat{Q} + \lambda\hat{Q}\hat{H}_1\hat{Q} + \lambda^2\hat{Q}\hat{H}_1\hat{P}\frac{1}{E - \hat{H}_0}\hat{P}\hat{H}_1\hat{Q} + \lambda^3\hat{Q}\hat{H}_1\hat{P}\frac{1}{E - \hat{H}_0}\hat{P}\hat{H}_1\hat{P}\frac{1}{E - \hat{H}_0}\hat{P}\hat{H}_1\hat{Q} + \dots} \quad (\text{C.11})$$

Remark that we have made no approximation: on subspace \hat{Q} , \hat{H}_{eff} coincides with the full Hamiltonian. The approximation then consists in cutting the formula at a given order in λ .

Remark that Brillouin-Wigner perturbation theory and standard (Rayleigh-Schrödinger) perturbation theory are equivalent at first order in λ . At higher orders, Brillouin-Wigner perturbation theory has the advantage of treating on equal footing degenerate and non-degenerate levels. Moreover, the order λ^n term writes in a compact formula, contrary to Rayleigh-Schrödinger perturbation theory. However, Brillouin-Wigner perturbation theory furnishes only an implicit equation on the perturbed energy E . This is not a problem if we are only interested in writing \hat{H}_{eff} at the lowest non-vanishing order in λ : we can then replace E by ε , the unperturbed energy.

Appendix D.

Renormalization group for the eigenstates of the Fibonacci chain

In this appendix, we derive the implicit equation the average fractal dimensions of the eigenstates obey. In the course of doing so, we find the analytical expression for the renormalization factors λ and $\bar{\lambda}$ (equation (2.47)).

the q -weight for an energy level E writes

$$\chi^{(l)}(E) = \sum_{m=1}^{F_l} |\psi_m(E)|^{2q} \quad (\text{D.1})$$

We are also going to define the partial sums on atomic (A) or on molecular (M) sites only:

$$\chi_{A/M}^{(l)}(E) = \sum_{m, \text{ at/mol}} |\psi_m(E)|^{2q} \quad (\text{D.2})$$

Atomic energy levels. Let us assume that E is an energy in the atomic cluster at step n . Using the tight-binding equations, we can relate at leading order in ρ the amplitudes on molecular sites to the amplitude on neighboring atomic sites. Using our Ansatz for the eigenstates, we relate the amplitude on atomic sites at step n to the amplitude on atomic and molecular sites at step $n-3$.

$$\chi^{(l)}(E) = \bar{\lambda}^q \left((1 + 2\rho^{2q} + \rho^{4q})\chi^{l-3}(E') + \rho^{4q}\chi_A^{l-3}(E') \right) \quad (\text{D.3})$$

Molecular energy levels. Using the tight-binding equations, we can relate the amplitudes on atomic sites to the amplitude on neighboring molecular sites. Specifically, we write the q -weight on an atomic site m surrounded by two molecular sites $m-1$ and $m+1$ as

$$|\psi_m|^{2q} = \gamma_q(\rho)\rho^{2q}(|\psi_{m-1}|^{2q} + |\psi_{m+1}|^{2q}) \quad (\text{D.4})$$

where we have introduced the function $\gamma_q(\rho)$ that takes into account the possible interferences between the site $m-1$ and $m+1$. We have the constraints $\gamma_0(\rho) = 1/2$, $\gamma_{q \neq 0}(0) = 1$, $\gamma_q(1) = 1/2$. We chose for this parameter the form $\gamma_q(\rho) = 1/(1 + \rho^{2q})$, which is supported by numerical evidences. Then, the total q -weight on a molecular level writes

$$\chi^{(l)}(E) = \lambda^q \left((2 + \gamma_q\rho^{2q})\chi^{l-2}(E') + \gamma_q\rho^{2q}\chi_A(E') \right) \quad (\text{D.5})$$

The special case $q = 1$. When $q = 1$, the q -norm is independant of l . Therefore, we have a closed system of equations for λ and $\bar{\lambda}$. It is straightforward to solve it, and we obtain the expressions given by equation (2.47).

The general case: q arbitrary. Now the q -norm depends on n . To obtain a closed system of equations, we take the limit $l \rightarrow \infty$, knowing that the limit behavior of the q -norm is $\log \chi_q^{(l)} \sim (q-1)\bar{D}^\psi_q \log(1/F_l)$. After averaging over the energies, we obtain as an implicit equation

$$2\omega^2(2\omega^2 I_{MM} + \omega^3 I_{AM}) + \omega^3(2\omega^2 I_{MA} + \omega^3 I_{AA}) = 1 \quad (\text{D.6})$$

with

$$\begin{aligned}
 I_{MM} &= (2 + 2\rho^{2q}\gamma_q(1 - M(\tau, q))) M(\tau, q) \\
 I_{AM} &= (2 + \rho^{2q}\gamma_q(1 + A(\tau, q))) M(\tau, q) \\
 I_{MA} &= (1 + 2\rho^{2q} + 2\rho^{4q}(1 - M(\tau, q))) A(\tau, q) \\
 I_{AA} &= (1 + 2\rho^{2q} + \rho^{4q}(1 + A(\tau, q))) A(\tau, q)
 \end{aligned}$$

and the ‘‘molecular’’ and ‘‘atomic’’ coefficients given by

$$\begin{aligned}
 M(\tau, q) &= \omega^{-2\tau} \lambda^q \\
 A(\tau, q) &= \omega^{-3\tau} \bar{\lambda}^q
 \end{aligned}$$

Then, for a given q , $\tau = \tau_q^\psi$ is the solution of the implicit equation (D.6). The averaged fractal dimensions of the eigenstates are given by $\overline{D}^\psi_q = \tau_q^\psi / (q - 1)$.

Perturbative expression in the strong modulation limit:

Neglecting terms of order ρ^{4q} in the above expression, we obtain

$$\begin{aligned}
 I_{MM} &\sim I_{AM} \sim \lambda(\rho)^q / \lambda(\rho^q) \omega^{-2\tau} \\
 I_{MA} &\sim I_{AA} \sim \bar{\lambda}(\rho)^q / \bar{\lambda}(\rho^q) \omega^{-3\tau}.
 \end{aligned}$$

Then, from (D.6) we get the perturbative formula (2.57).

The derivation of the implicit relation for the averaged local spectral dimensions (equation (2.62)) is in the same lines. The final relation is much simpler because we have dropped the terms of order ρ^{4q} . This is in order to be consistent with the results for the spectrum, that are only valid at leading order in ρ .

Appendix E.

Variational method

In this appendix we derive the variational equations used in Sec. 4.6.4 for approximation of the 2D groundstate on the Ammann-Beenker tiling.

We recall that the Hamiltonian writes

$$\hat{H}(t, V) = -t\hat{H}_0 + V\hat{H}_1, \quad (\text{E.1})$$

with

$$\hat{H}_0 = \sum_{\langle m, n \rangle} |m\rangle \langle n| + \text{H.c.}, \quad (\text{E.2})$$

and

$$\hat{H}_1 = \sum_m z_m |m\rangle \langle m|. \quad (\text{E.3})$$

We work with the following variational wavefunction:

$$\psi(m) = C_{\mu(m)} e^{\kappa h(m)} \quad (\text{E.4})$$

where $\mu(m)$ is the nearest neighbors configuration of the site m : $\mu = \text{A, B, C, D}_1, \text{D}_2, \text{E, F}$ (see Sec. 4.6.3 for details).

E.0.1. The variational energy

We recall that variational method consists in minimizing the energy $E(\{C\}, \kappa) = \langle \psi | \hat{H} | \psi \rangle / \langle \psi | \psi \rangle$ with respect to variational parameters of $|\psi\rangle$, namely here the constant κ and the 7 preexponential factors C_μ , $\mu = \text{A, B, C, D}_1, \text{D}_2, \text{E, F}$. We thus have 8 variational equations, the solution of which gives an approximation to the exact groundstate wavefunction of our Hamiltonian.

Evaluation of the norm $\langle \psi | \psi \rangle$.

In the following, we work on a finite-size sample \mathcal{R}_t , and we then let the size of the sample go to infinity ($\mathcal{R}_t \rightarrow \mathcal{R}_\infty$). In the same lines as in Sec. 4.1.4 and in appendix 4.6.2, we first compute $N_\mu^{(t)}(h)$, the number of times we have height h on sites of type μ inside region \mathcal{R}_t . For that, we introduce the generalized inflation matrix

$$M(\beta) = \begin{bmatrix} 1 & 1 & 1 & 1 & 0 & 0 & 0 \\ 0 & 0 & 0 & 0 & 1 & 0 & 0 \\ 0 & 0 & 0 & 0 & 0 & 1 & 0 \\ 0 & 0 & 0 & 0 & 0 & 0 & 1 \\ 0 & 0 & 0 & 0 & 0 & 0 & e^\beta \\ 0 & 0 & 0 & 0 & 2e^\beta & 3e^\beta & 2e^\beta \\ 8e^\beta & 8e^\beta & 8e^\beta & 8e^\beta & 5e^\beta & 2e^\beta & 0 \end{bmatrix}. \quad (\text{E.5})$$

This matrix has the same physical interpretation as the generalized inflation matrices introduced in Sec. 4.1.4 and in appendix. 4.6.2. In particular, $M(0)$ is the geometrical inflation matrix

Appendix E. Variational method

relating the number of sites of type $\mu = A, B, \dots$ after t inflations to the number of sites after $t + 1$ inflations. Let $f(\beta)$ is the eigenvector associated to the largest eigenvalue of $M(-\beta)M(\beta)$. We have

$$\langle \psi | \psi \rangle = \sum_{\mu} C_{\mu}^2 \sum_h e^{2\kappa h} N_{\mu}^{(t)}(h) \quad (\text{E.6})$$

$$= \sum_{\mu} C_{\mu}^2 Z_{\mu}^{(t)}(2\kappa) \quad (\text{E.7})$$

$$= \omega^t(2\kappa) \sum_{\mu} C_{\mu}^2 f_{\mu}(2\kappa) \quad (\text{E.8})$$

Evaluation of the average $\langle \psi | \hat{H}_0 | \psi \rangle$.

$$\langle \psi | \hat{H}_0 | \psi \rangle = \sum_{\mu, \nu} C_{\mu} C_{\nu} \sum_h e^{\kappa(2h + \epsilon(\mu \rightarrow \nu))} N_{\nu}(\mu, h) \quad (\text{E.9})$$

$N_{\nu}(\mu, h)$ is the number of bonds (μ, ν) with μ having height h . $\epsilon(\mu \rightarrow \nu) = \pm 1$ respectively if the arrow goes from μ to ν or the reverse. We can write $N_{\nu}(\mu, h) = z(\nu|\mu, h)N_{\mu}(h)$ with $z(\nu|\mu, h)$ the average number of type ν sites around type μ sites that have height h . If the number of ν sites around μ is always the same, then $z(\nu|\mu, h) = z(\nu|\mu)$. This is the case for $\mu < \nu$ (here we use lexicographic order: $1 = A, 2 = B, 3 = C, 4 = D_1, 5 = D_2, 6 = E, 7 = F$). Assuming $\mu < \nu$, we have

$$\sum_h e^{2\kappa h} N_{\nu}(\mu, h) = z(\nu|\mu) \sum_h e^{2\kappa h} N_{\mu}(h) \quad (\text{E.10})$$

$$= z(\nu|\mu) Z_{\mu}(2\kappa) \quad (\text{E.11})$$

Because the Hamiltonian is real symmetric, $e^{\kappa\epsilon(\mu \rightarrow \nu)} N_{\nu}(\mu, m)$ is symmetric under the exchange of μ and ν . So, finally

$$\langle \psi | \hat{H}_0 | \psi \rangle = \omega^t(2\kappa) \sum_{\mu, \nu} C_{\mu} h_{\mu, \nu}(2\kappa) C_{\nu} \quad (\text{E.12})$$

where h is the symmetric 7×7 matrix

$$h_{\mu, \nu}(2\kappa) = e^{\kappa\epsilon(\mu \rightarrow \nu)} z(\nu|\mu) f_{\mu}(2\kappa) \text{ if } \mu < \nu \quad (\text{E.13})$$

$$= e^{\kappa\epsilon(\nu \rightarrow \mu)} z(\mu|\nu) f_{\nu}(2\kappa) \text{ if } \mu > \nu. \quad (\text{E.14})$$

Evaluation of $\langle \psi | \hat{H} | \psi \rangle$

This straightforwardly amounts to replacing $h_{\mu, \nu}$ by

$$- t h_{\mu, \nu}(2\kappa) + V z_{\mu} f_{\mu}(2\kappa) \delta_{\mu, \nu} \quad (\text{E.15})$$

with z_{μ} the coordination of type μ sites.

E.0.2. The variational equations

If the energy has an extrema with respect to p , it obeys the equation

$$\partial_p \langle \psi | \hat{H} | \psi \rangle = E(p) \partial_p \langle \psi | \psi \rangle. \quad (\text{E.16})$$

Here we have two kinds of parameters: the preexponential factors C and κ . Let us consider each in turn.

Extremization with respect to C

Let us first extremize for \hat{H}_0 . Since h is symmetric, we have

$$\sum_{\nu} h_{\mu,\nu} C_{\nu} = E f_{\mu} C_{\mu} \quad (\text{E.17})$$

So, $\mathbf{C}(\kappa)$ is an eigenvector of the matrix $M_{\mu,\nu} = h_{\mu,\nu}(\kappa)/f_{\mu}(\kappa^2)$, with eigenvalue E . There are thus 7 independent solutions for $\mathbf{C}(\kappa)$, for each value of κ . The extension to H is simple: $M_{\mu,\nu}$ becomes

$$M_{\mu,\nu} = -t h_{\mu,\nu}(2\kappa)/f_{\mu}(2\kappa) + V z_{\mu} \delta_{\mu,\nu} \quad (\text{E.18})$$

Finding the extrema with respect to the C parameters amounts to diagonalizing the matrix M . Although it is possible to diagonalize M exactly, we do not reproduce the solution here as it is too long.

Extremization with respect to κ

Since h is symmetric, we can write

$$\langle \psi | \hat{H}_0 | \psi \rangle = 2 \sum_{\mu < \nu} C_{\nu} z(\nu|\mu) f_{\mu}(2\kappa) e^{\kappa\epsilon(\mu \rightarrow \nu)} C_{\mu} \quad (\text{E.19})$$

Then, extremization yields

$$\sum_{\mu < \nu} C_{\nu} z(\nu|\mu) \partial_{\kappa} \left(f_{\mu}(2\kappa) e^{\kappa\epsilon(\mu \rightarrow \nu)} \right) C_{\mu} = E \sum_{\mu} C_{\mu}^2 f'_{\mu}(2\kappa) \quad (\text{E.20})$$

The extension to \hat{H} is, again, straightforward. We were not able to solve this last equation analytically. We instead solved it numerically.

Bibliography

- E. Akkermans. Statistical mechanics and quantum fields on fractals. *Fractal Geometry and Dynamical Systems in Pure and Applied Mathematics II: Fractals in Applied Mathematics*, 2013.
- R. Ammann, B. Grünbaum, and G. C. Shephard. Aperiodic tiles. *Discrete & Computational Geometry*, 8(1):1–25, 1992.
- M. Baake and U. Grimm. *Aperiodic Order*. Cambridge University Press, 2013. ISBN 9780521869911.
- J. C. Baez. Rényi entropy and free energy. *arXiv preprint arXiv:1102.2098*, 2011.
- D. Barache and J. Luck. Electronic spectra of strongly modulated aperiodic structures. *Physical Review B*, 49(21):15004, 1994.
- N. Bédaride and T. Fernique. *The Ammann–Beenker Tilings Revisited*, pages 59–65. Springer Netherlands, Dordrecht, 2013. ISBN 978-94-007-6431-6. doi: 10.1007/978-94-007-6431-6_8. URL http://dx.doi.org/10.1007/978-94-007-6431-6_8.
- C. W. J. Beenakker. Random-matrix theory of quantum transport. *Rev. Mod. Phys.*, 69:731–808, Jul 1997. doi: 10.1103/RevModPhys.69.731. URL <http://link.aps.org/doi/10.1103/RevModPhys.69.731>.
- J. Bellissard. Gap labelling theorems for schrödinger operators. In *From number theory to physics*, pages 538–630. Springer, 1992.
- J. Bellissard, B. Iochum, E. Scoppola, and D. Testard. Spectral properties of one-dimensional quasi-crystals. *Comm. Math. Phys.*, 125(3):527–543, 1989. URL <http://projecteuclid.org/euclid.cmp/1104179532>.
- J. Bellissard, D. Herrmann, and M. Zarrouati. Hull of aperiodic solids and gap labelling theorems. *Directions in mathematical quasicrystals*, 13:207–258, 2000.
- J. Bellissard, J. Kellendonk, and A. Legrand. Gap-labelling for three-dimensional aperiodic solids. *Comptes Rendus de l’Académie des Sciences-Series I-Mathematics*, 332(6):521–525, 2001.
- L. Bendersky. Quasicrystal with one-dimensional translational symmetry and a tenfold rotation axis. *Physical Review Letters*, 55(14):1461, 1985.
- R. Berger. *The undecidability of the domino problem*. American Mathematical Soc., 1966.
- D. Damanik. Almost everything about the fibonacci operator. *New Trends in Mathematical Physics*, pages 149–159, 2009.
- D. Damanik and A. Gorodetski. Spectral and quantum dynamical properties of the weakly coupled fibonacci hamiltonian. *Communications in Mathematical Physics*, 305(1):221–277, 2011. ISSN 0010-3616. doi: 10.1007/s00220-011-1220-2. URL <http://dx.doi.org/10.1007/s00220-011-1220-2>.

Bibliography

- E. de Prunelé. Penrose structures: Gap labeling and geometry. *Phys. Rev. B*, 66:094202, Sep 2002. doi: 10.1103/PhysRevB.66.094202. URL <http://link.aps.org/doi/10.1103/PhysRevB.66.094202>.
- J.-M. Dumont. Summation formulae for substitutions on a finite alphabet. In *Number Theory and Physics*, pages 185–194. Springer, 1990.
- J.-M. Dumont and A. Thomas. Digital sum problems and substitutions on a finite alphabet. *Journal of Number Theory*, 39(3):351–366, 1991.
- M. Duneau and A. Katz. Quasiperiodic patterns. *Phys. Rev. Lett.*, 54:2688–2691, Jun 1985. doi: 10.1103/PhysRevLett.54.2688. URL <https://link.aps.org/doi/10.1103/PhysRevLett.54.2688>.
- M. Duneau, R. Mosseri, and C. Oguey. Approximants of quasiperiodic structures generated by the inflation mapping. *Journal of Physics A: Mathematical and General*, 22(21):4549, 1989. URL <http://stacks.iop.org/0305-4470/22/i=21/a=017>.
- E. N. Economou and C. M. Soukoulis. Static conductance and scaling theory of localization in one dimension. *Phys. Rev. Lett.*, 46:618–621, Mar 1981. doi: 10.1103/PhysRevLett.46.618. URL <http://link.aps.org/doi/10.1103/PhysRevLett.46.618>.
- V. Elser. The diffraction pattern of projected structures. *Acta Crystallographica Section A*, 42(1):36–43, Jan 1986. doi: 10.1107/S0108767386099932. URL <https://doi.org/10.1107/S0108767386099932>.
- Y. Feng, G. Lu, H. Ye, K. Kuo, R. Withers, and G. Van Tendeloo. Experimental evidence for and a projection model of a cubic quasi-crystal. *Journal of Physics: Condensed Matter*, 2(49):9749, 1990.
- N. P. Fogg. *Substitutions in Dynamics, Arithmetics and Combinatorics*. Springer, 2002.
- N. P. Frank and E. A. Robinson. Generalized β -expansions, substitution tilings, and local finiteness. *Trans. Amer. Math. Soc.*, 360:1163–1177, 2008. doi: 10.1090/S0002-9947-07-04527-8.
- T. Fujiwara, M. Kohmoto, and T. Tokihiro. Multifractal wave functions on a fibonacci lattice. *Phys. Rev. B*, 40:7413–7416, Oct 1989. doi: 10.1103/PhysRevB.40.7413. URL <http://link.aps.org/doi/10.1103/PhysRevB.40.7413>.
- W. Gellermann, M. Kohmoto, B. Sutherland, and P. C. Taylor. Localization of light waves in fibonacci dielectric multilayers. *Phys. Rev. Lett.*, 72:633–636, Jan 1994. doi: 10.1103/PhysRevLett.72.633. URL <http://link.aps.org/doi/10.1103/PhysRevLett.72.633>.
- C. Godrèche and J. M. Luck. Indexing the diffraction spectrum of a non-pisot self-similar structure. *Phys. Rev. B*, 45:176–185, Jan 1992. doi: 10.1103/PhysRevB.45.176. URL <https://link.aps.org/doi/10.1103/PhysRevB.45.176>.
- C. Goodman-Strauss. Matching rules and substitution tilings. *Annals of Mathematics*, 147(1):181–223, 1998. ISSN 0003486X. URL <http://www.jstor.org/stable/120988>.
- T. C. Halsey, M. H. Jensen, L. P. Kadanoff, I. Procaccia, and B. I. Shraiman. Fractal measures and their singularities: The characterization of strange sets. *Phys. Rev. A*, 33:1141–1151, Feb 1986. doi: 10.1103/PhysRevA.33.1141. URL <http://link.aps.org/doi/10.1103/PhysRevA.33.1141>.

- C. R. Iacovella, A. S. Keys, and S. C. Glotzer. Self-assembly of soft-matter quasicrystals and their approximants. *Proceedings of the National Academy of Sciences*, 108(52):20935–20940, 2011.
- T. Ishimasa, H.-U. Nissen, and Y. Fukano. New ordered state between crystalline and amorphous in ni-cr particles. *Physical Review Letters*, 55(5):511, 1985.
- A. Julien, J. Kellendonk, and J. Savinien. *Mathematics of Aperiodic Order*, chapter On the Noncommutative Geometry of Tilings, pages 259–306. Springer Basel, 2015.
- P. Kalugin and A. Katz. Electrons in deterministic quasicrystalline potentials and hidden conserved quantities. *Journal of Physics A: Mathematical and Theoretical*, 47(31):315206, 2014. URL <http://stacks.iop.org/1751-8121/47/i=31/a=315206>.
- P. Kalugin, A. Kitaev, and L. Levitov. Electron spectrum of a one-dimensional quasicrystal. *Sov. Phys. JETP*, 64(2), 1986. URL <http://www.jetp.ac.ru/cgi-bin/e/index/e/64/2/p410?a=list>.
- P. A. Kalugin, A. Y. Kitaev, and L. S. Levitov. $Al_{0.86}Mn_{0.14}$ - A 6-Dimensional Crystal. *JETP Letters*, 41(3):145–149, 1985. ISSN 0021-3640.
- J. Kellendonk and J. Savinien. Spectral triples and characterization of aperiodic order. *Proceedings of the London Mathematical Society*, 2012.
- R. Ketzmerick, K. Kruse, S. Kraut, and T. Geisel. What Determines the Spreading of a Wave Packet? *Physical Review Letters*, 79(September), 1997. ISSN 0031-9007. doi: 10.1103/PhysRevLett.77.1413. URL <http://link.aps.org/doi/10.1103/PhysRevLett.81.5039>.
- A. Khamzin, R. Nigmatullin, and D. Groshev. Analytical investigation of the specific heat for the cantor energy spectrum. *Physics Letters A*, 379(12):928–932, 2015.
- R. Killip, A. Kiselev, and Y. Last. Dynamical upper bounds on wavepacket spreading. *American journal of mathematics*, pages 1165–1198, 2003.
- M. Kohmoto. Entropy function for multifractals. *Physical review A*, 37(4):1345, 1988.
- M. Kohmoto and B. Sutherland. Electronic states on a penrose lattice. *Phys. Rev. Lett.*, 56: 2740–2743, Jun 1986. doi: 10.1103/PhysRevLett.56.2740. URL <http://link.aps.org/doi/10.1103/PhysRevLett.56.2740>.
- M. Kohmoto, L. P. Kadanoff, and C. Tang. Localization problem in one dimension: Mapping and escape. *Phys. Rev. Lett.*, 50:1870–1872, Jun 1983. doi: 10.1103/PhysRevLett.50.1870. URL <https://link.aps.org/doi/10.1103/PhysRevLett.50.1870>.
- M. Kohmoto, B. Sutherland, and C. Tang. Critical wave functions and a Cantor-set spectrum of a one-dimensional quasicrystal model. *Physical Review B*, 35(3), 1987. URL <http://journals.aps.org/prb/abstract/10.1103/PhysRevB.35.1020>.
- M. Lapidus and M. Van Frankenhuysen. *Fractal Geometry and Number Theory: Complex dimensions of fractal strings and zeros of zeta functions*. Springer Science & Business Media, 2013.
- D. Levine and P. J. Steinhardt. Quasicrystals. i. definition and structure. *Physical Review B*, 34(2):596, 1986.
- E. Levy, A. Barak, A. Fisher, and E. Akkermans. Topological properties of Fibonacci quasicrystals : A scattering analysis of Chern numbers. *arXiv*, pages 1–9, 2015.

Bibliography

- R. Lifshitz and S. E.-D. Mandel. Observation of log-periodic oscillations in the quantum dynamics of electrons on the one-dimensional fibonacci quasicrystal. *Philosophical Magazine*, 91(19-21): 2792–2800, 2011.
- J. M. Luck. Cantor spectra and scaling of gap widths in deterministic aperiodic systems. *Phys. Rev. B*, 39:5834–5849, Mar 1989. doi: 10.1103/PhysRevB.39.5834. URL <http://link.aps.org/doi/10.1103/PhysRevB.39.5834>.
- N. Macé, A. Jagannathan, and F. Piéchon. Fractal dimensions of wave functions and local spectral measures on the fibonacci chain. *Phys. Rev. B*, 93:205153, May 2016. doi: 10.1103/PhysRevB.93.205153. URL <http://link.aps.org/doi/10.1103/PhysRevB.93.205153>.
- N. Macé, A. Jagannathan, P. Kalugin, R. Mosseri, and F. Piéchon. Critical eigenstates and their properties in one- and two-dimensional quasicrystals. *Phys. Rev. B*, 96:045138, Jul 2017. doi: 10.1103/PhysRevB.96.045138. URL <https://link.aps.org/doi/10.1103/PhysRevB.96.045138>.
- N. Macé, A. Jagannathan, and F. Piéchon. Gap structure of 1d cut and project hamiltonians. In *Journal of Physics: Conference Series*, volume 809, page 012023. IOP Publishing, 2017.
- A. D. Mirlin, Y. V. Fyodorov, A. Mildenerger, and F. Evers. Exact relations between multifractal exponents at the anderson transition. *Physical Review Letters*, 97(July):1–4, 2006. ISSN 00319007. doi: 10.1103/PhysRevLett.97.046803.
- R. Mosseri. Universalities in condensed matter. *Les Houches proceedings*, 42, 1988.
- Q. Niu and F. Nori. Renormalization-group study of one-dimensional quasiperiodic systems. *Phys. Rev. Lett.*, 57:2057–2060, Oct 1986. doi: 10.1103/PhysRevLett.57.2057. URL <http://link.aps.org/doi/10.1103/PhysRevLett.57.2057>.
- Q. Niu and F. Nori. Spectral splitting and wave-function scaling in quasicrystalline and hierarchical structures. *Physical Review B*, 42(16), 1990. URL <http://journals.aps.org/prb/abstract/10.1103/PhysRevB.42.10329>.
- B. Passaro, C. Sire, and V. Benza. Anomalous diffusion and conductivity in octagonal tiling models. *Physical review. B, Condensed matter*, 46(21):13751–13755, dec 1992. ISSN 0163-1829. URL <http://www.ncbi.nlm.nih.gov/pubmed/10003433>.
- F. Piéchon. Anomalous diffusion properties of wave packets on quasiperiodic chains. *Phys. Rev. Lett.*, 76:4372–4375, Jun 1996. doi: 10.1103/PhysRevLett.76.4372. URL <http://link.aps.org/doi/10.1103/PhysRevLett.76.4372>.
- F. Piéchon, M. Benakli, and A. Jagannathan. Analytical results for scaling properties of the spectrum of the fibonacci chain. *Phys. Rev. Lett.*, 74:5248–5251, Jun 1995. doi: 10.1103/PhysRevLett.74.5248. URL <http://link.aps.org/doi/10.1103/PhysRevLett.74.5248>.
- P. Repetowicz, U. Grimm, and M. Schreiber. Exact eigenstates of tight-binding hamiltonians on the penrose tiling. *Phys. Rev. B*, 58:13482–13490, Nov 1998. doi: 10.1103/PhysRevB.58.13482. URL <http://link.aps.org/doi/10.1103/PhysRevB.58.13482>.
- T. Rieth and M. Schreiber. Numerical investigation of electronic wave functions in quasiperiodic lattices. *Journal of Physics: Condensed Matter*, 10(4):783, 1998. URL <http://stacks.iop.org/0953-8984/10/i=4/a=008>.

- A. Rodriguez, L. J. Vasquez, and R. A. Römer. Multifractal analysis with the probability density function at the three-dimensional anderson transition. *Phys. Rev. Lett.*, 102:106406, Mar 2009. doi: 10.1103/PhysRevLett.102.106406. URL <http://link.aps.org/doi/10.1103/PhysRevLett.102.106406>.
- A. Rüdinger and C. Sire. Analytical results for multifractal properties of spectra of quasiperiodic hamiltonians near the periodic chain. *Journal of Physics A: Mathematical and General*, 29(13): 3537, 1996. URL <http://stacks.iop.org/0305-4470/29/i=13/a=022>.
- L. Sadun. *Mathematics of Aperiodic Order*, chapter Cohomology of Hierarchical Tilings, pages 73–104. Springer, 2015. URL <http://arxiv.org/abs/1406.0882>.
- R. Sedgewick and P. Flajolet. *An introduction to the analysis of algorithms*. Addison-Wesley, 2013.
- D. Shechtman, I. Blech, D. Gratias, and J. W. Cahn. Metallic phase with long-range orientational order and no translational symmetry. *Physical review letters*, 53(20):1951, 1984.
- C. Sire and R. Mosseri. Spectrum of 1d quasicrystals near the periodic chain. *J. Phys. France*, 50(24):3447–3461, 1989. doi: 10.1051/jphys:0198900500240344700. URL <http://dx.doi.org/10.1051/jphys:0198900500240344700>.
- C. Sire and R. Mosseri. Excitation spectrum, extended states, gap closing : some exact results for codimension one quasicrystals. *J. Phys. France*, 51(15):1569–1583, 1990. doi: 10.1051/jphys:0199000510150156900. URL <http://dx.doi.org/10.1051/jphys:0199000510150156900>.
- J. E. S. Socolar. Simple octagonal and dodecagonal quasicrystals. *Phys. Rev. B*, 39:10519–10551, May 1989. doi: 10.1103/PhysRevB.39.10519. URL <https://link.aps.org/doi/10.1103/PhysRevB.39.10519>.
- C. M. Soukoulis and E. N. Economou. Off-diagonal disorder in one-dimensional systems. *Phys. Rev. B*, 24:5698–5702, Nov 1981. doi: 10.1103/PhysRevB.24.5698. URL <http://link.aps.org/doi/10.1103/PhysRevB.24.5698>.
- B. Sutherland. Self-similar ground-state wave function for electrons on a two-dimensional penrose lattice. *Phys. Rev. B*, 34:3904–3909, Sep 1986. doi: 10.1103/PhysRevB.34.3904. URL <http://link.aps.org/doi/10.1103/PhysRevB.34.3904>.
- B. Sutherland. Critical electronic wave functions on quasiperiodic lattices: Exact calculation of fractal measures. *Phys. Rev. B*, 35:9529–9534, Jun 1987. doi: 10.1103/PhysRevB.35.9529. URL <http://link.aps.org/doi/10.1103/PhysRevB.35.9529>.
- A. Sütő. Singular continuous spectrum on a cantor set of zero lebesgue measure for the fibonacci hamiltonian. *Journal of Statistical Physics*, 56(3):525–531, 1989. ISSN 1572-9613. doi: 10.1007/BF01044450. URL <http://dx.doi.org/10.1007/BF01044450>.
- D. Tanese, E. Gurevich, F. Baboux, T. Jacqmin, A. Lemaître, E. Galopin, I. Sagnes, A. Amo, J. Bloch, and E. Akkermans. Fractal energy spectrum of a polariton gas in a fibonacci quasiperiodic potential. *Phys. Rev. Lett.*, 112:146404, Apr 2014. doi: 10.1103/PhysRevLett.112.146404. URL <http://link.aps.org/doi/10.1103/PhysRevLett.112.146404>.
- C. Tang and M. Kohmoto. Global scaling properties of the spectrum for a quasiperiodic schrödinger equation. *Physical Review B*, 34(3):2041, 1986.

Bibliography

- S. Thiem. Origin of the log-periodic oscillations in the quantum dynamics of electrons in quasiperiodic systems. *Philosophical Magazine*, 95(11):1233–1243, 2015.
- S. Thiem and M. Schreiber. Generalized inverse participation numbers in metallic-mean quasiperiodic systems. *The European Physical Journal B*, 83(4):415–421, 2011. ISSN 1434-6036. doi: 10.1140/epjb/e2011-20323-7. URL <http://dx.doi.org/10.1140/epjb/e2011-20323-7>.
- S. Thiem and M. Schreiber. Wavefunctions, quantum diffusion, and scaling exponents in golden-mean quasiperiodic tilings. *Journal of Physics: Condensed Matter*, 25(7):075503, 2013. URL <http://stacks.iop.org/0953-8984/25/i=7/a=075503>.
- T. Tokihiro, T. Fujiwara, and M. Arai. Exact eigenstates on a two-dimensional penrose lattice and their fractal dimensions. *Phys. Rev. B*, 38:5981–5987, Sep 1988. doi: 10.1103/PhysRevB.38.5981. URL <http://link.aps.org/doi/10.1103/PhysRevB.38.5981>.
- M. Verbin, O. Zilberberg, Y. Lahini, Y. E. Kraus, and Y. Silberberg. Topological pumping over a photonic fibonacci quasicrystal. *Phys. Rev. B*, 91:064201, Feb 2015. doi: 10.1103/PhysRevB.91.064201. URL <http://link.aps.org/doi/10.1103/PhysRevB.91.064201>.
- N. Wang, H. Chen, and K. Kuo. Two-dimensional quasicrystal with eightfold rotational symmetry. *Physical review letters*, 59(9):1010, 1987.
- S.-I. Yasutomi. On sturmian sequences which are invariant under some substitutions. *Kluwer Acad. Publ.*, 1999.
- H. Yuan, U. Grimm, P. Repetowicz, and M. Schreiber. Energy spectra, wave functions, and quantum diffusion for quasiperiodic systems. *Physical Review B*, 62(23):15569, 2000.
- W. M. Zheng. Global scaling properties of the spectrum for the fibonacci chains. *Phys. Rev. A*, 35:1467–1469, Feb 1987. doi: 10.1103/PhysRevA.35.1467. URL <https://link.aps.org/doi/10.1103/PhysRevA.35.1467>.
- E. Zijlstra. Electronic structure of the octagonal tiling. *Journal of Non-Crystalline Solids*, 334–335: 126 – 129, 2004. ISSN 0022-3093. doi: <http://dx.doi.org/10.1016/j.jnoncrysol.2003.11.026>. URL <http://www.sciencedirect.com/science/article/pii/S0022309303008585>. 8th International Conference on Quasicrystals.